Electrical Properties of Chemically Derived Graphene

A dissertation submitted to the
ÉCOLE POLYTECHNIQUE FÉDÉRALE DE LAUSANNE

for the degree of
Doctor ès Sciences

by
Ravi Shankar Sundaram

Examining Board
Prof. O. Schneider, president
Prof. Klaus Kern, thesis director
Prof. Cristoph Stampfer, referee
Prof. Marcel Mayor, referee
Prof. Andras Kis, referee

March 2011

Abstract

Graphene, an atomically thin sheet of carbon, is the most recent endeavor for the application of carbon nanostructures in conventional electronics. The envisioned creation of devices completely carved out of graphene could lead to the revolution of electronic circuitry. However, the most established technique to obtain high quality graphene sheets, i.e, by micromechanical cleavage cannot be easily upscaled., serving as an impediment towards technological applications. The present thesis is dedicated to the study of graphene prepared via an alternative scalable, high yield and cost effective method which involves the chemical reduction of graphene oxide.

The first part of this thesis describes in detail the atomic structure of graphene obtained by this method. Raman spectroscopy was used for this purpose followed by Transmission Electron Microscopy (TEM) and Near Edge X-Ray and Fine Structure (NEXAFS) measurements locally probe these sheets with atomic resolution. This revealed a highly disordered structure of this material, where regions with perfect crystallinity are separated by defect clusters. These defective patches were found to contain remnant oxygenated functional groups.

Electrical characterization of chemically derived graphene sheets yielded ambipolar transfer characteristics similar to that of micromechanically cleaved graphene, albeit with moderate performance. The presence of a significant amount of disorder precludes ballistic transport and the charge carriers traverse through the sheet predominantly by thermally assisted variable range hopping in combination with a field driven tunneling mechanism. This is clearly evidenced in the low temperature two-probe conduction measurements performed on devices fabricated from these sheets.

Metal contacts in graphene devices play a crucial role in limiting the applicability of these materials. Although the performance of graphene based devices as prepared today is sufficient for a variety of applications, a clear understanding and engineering of contacts is important for utilization of these materials towards high end applications. In the latter part of this thesis a detailed study of contacts is presented; firstly on graphene grown via CVD on copper to understand the physics in play at a simpler carbon-metal interface, followed by a photocurrent microscopy study to understand the more complex interface between metal and reduced graphene oxide and its implications on device characteristics. A strong difference between the two kinds of graphene is found with metal contacts to high quality graphene creating a potential barrier at the interface owing to a charge transfer between them, whereas in the case of the chemically synthesized version contacts are of a non invasive nature stable upto 300 °C. In addition, Raman spectroscopy and Scanning Photocurrent Microscopy investigation of graphene obtained by CVD under the gold, away from the contact edge provided interesting insights towards the phenomena occuring at the gold graphene interface, thus highlighting the importance of understanding and engineering adequate contacts before the successful transition of graphene based devices into the industry.

Finally, a novel chemical vapor treatment of graphene oxide was employed to enhance its electrical characteristics. Exposure of reduced graphene oxide to ethylene vapor at 800 °C results in an improvement of conductivities by 2 orders of magnitude lagging behind that of pristine graphene. Electrical and structural characterization revealed that this increase in conductivity occurred inspite of the presence of a considerable amount of defects.

Keywords: Carbon nanoelectronics, Graphene, Graphene oxide, Atomic structure, TEM, Raman Spectroscopy, NEXAFS, Scanning photocurrent microscopy, Field effect transistor, contacts, CVD.

Zusammenfassung

Die Entdeckung von Graphen, einem atomar dicken Kohlenstoffblatt, hat wesentlich dazu beitragen, dass der Einsatz von Kohlenstoff-Nanostrukturen in elektronischen Bauelementen in greifbare Nähe gerckt ist. Die Realisierung von vollständig Graphen-basierten, integrierten Schaltungen stellt in der Tat eine technologische Revolution in Aussicht. Eine wesentliche Hürde fr die Erreichung diese Ziels besteht allerdings in der notwendigen Entwicklung von Syntheseverfahren, welche gröere Mengen an hochwertigem Graphen liefern können. Das bislang hauptsächlich eingesetzte Verfahren der mechanischen Exfolierung liefert zwar Graphen mit geringer Defektdichte, jedoch nur in geringer Flchendichte (wenige Flocken pro cm^2 Substratoberfläche). In der vorliegenden Doktorarbeit wird ein alternatives Verfahren untersucht, welches einen kostengünstigen Zugang zu größeren Mengen an ausgedehnten Graphenschichten gestattet. Hierin dient Graphenoxid als Zwischenstufe, welche auf chemischem Wege (Reduktion) möglichst weitgehend von den enthaltenen Sauerstoffatomen befreit wird.

Der erste Teil der Arbeit beschäftigt sich mit der atomaren Struktur des chemisch synthetisierten Graphens. Hierzu wurde das Graphen mittels Raman-Spektroskopie, Transmissionselektronenmikroskopie, sowie Röntgen absorptions Spektroskopie im Detail untersucht. Dabei trat zutage, dass in den Schichten wenige Nanometer ausgedehnte Bereiche hoher kristalliner Ordnung (perfektes hexagonales Kohlenstoffgitter), umgeben von Defektclustern, vorliegen. Die Cluster wurden als Orte identifiziert, an welchen eine gewisse Restmenge an sauerstoffhaltigen Gruppen vorliegt.

Im Anschluss werden die elektrischen Eigenschaften des chemisch hergestellten Graphens beschrieben. Elektrische Messungen als Funktion von angelegter Biasspannung, Gatespannung und der Temperatur ergaben, dass in diesem Material im Wesentlichen eine Hüpfleitung vorliegt, welche bei tiefen Temperaturen in temperaturabhängiges Tunneln übergeht. Ein weiteres wichtiges Ziel bestand darin zu klären, auf welche Weise die in dem chemisch gewonnenen Graphen vorhandenen Defekte die Eigenschaften der Metallkontakte beeinflussen. Dabei stellte sich heraus, dass zur Gewinnung intimer Goldkontakte ein Heizen der Proben auf mehrere hundert Grad Celsius notwendig ist. Parallel dazu wurde untersucht, in welchem Ausmaß die hufig eingesetzten Topkontakte aus Gold die elektronischen und vibronischen Eigenschaften des Graphens verändern. In diesen Experimenten wurden Graphenschichten verwendet, welche durch chemische Gasphasenabscheidung gewonnen wurden. Die Kombination von lokalen Photostrom- und Raman-Messungen ergab, dass die zuvor genannten Eigenschaften des Graphens nach Goldbedampfung nahezu unverändert sind.

Der letzte Teil der Arbeit widmet sich einer neuen Methode zur Verringerung der Defektdichte in dem chemisch hergestellten Graphen. Diese beinhaltet die Gasphasenabscheidung von Kohlenstoff aus einer gasförmigen Vorstufe auf das chemisch reduzierte Graphenoxid. Auf diese Weise konnte die elektrische Leitfhigkeit des Materials um zwei Gröenordnungen erhht werden. Mittels Raman-Spektroskopie wurde gefunden, dass die Leitfähigkeitserhöhung mit einer Zunahme der Defektdichte in den Proben einhergeht.

Schlüsselwörter: Kohlenstoff-basierte Nanoelektronik, Graphen, Graphenoxid, Transmissionselektronenmikroskopie, Ramanspektroskopie, Rntgenabsorption, Lokale Photostrommessungen, Feldeffekttransistoren, Metallkontakte, chemische Gasphasenabscheidung

Contents

Chapter 1

Introduction

Electronics, a seemingly modern field of research and application, has been used by mankind from as long as 2750 BC. Ancient Egyptian texts report the existence of "electric fish" which were observed again a millennia later in the literature of ancient Greek, Roman and Arabic naturalists and physicians. Although it remained just an intellectual curiosity for centuries, mankind has always found applications for it. Several ancient writers, such as Pliny the Elder and Scribonius Largus, attested to the numbing effect of electric shocks delivered by catfish and torpedo rays, and knew that such shocks could travel along conducting objects. Patients suffering from ailments such as gout or headache were directed to touch electric fish in the hope that the powerful jolt might cure them [1]. However, the surge of electronic applications as we know it today started with the discovery of conduction through a vacuum tube in 1883 which brought about the avalanche of modern day electronic devices. As technology advanced over the years the scope of applications widened and the quest for faster, smaller and more efficient technologies grew continuously.

For the past forty years, computers have grown more powerful as their basic sub-unit, the transistor has been continuously shrinking in size. This has been the driving factor in the boom of the information technology industry. However, further reduction in size of semiconductor transistors is likely to be inhibited due to the fundamental problems governed by the laws of quantum mechanics, plus the limitations of materials and fabrication techniques. Researchers have projected that as the overall size of the semiconductor transistor is aggressively miniaturized to approximately 0.1 micron (i.e., 100 nanometers) and beyond, the devices may no longer function as well. Thus, in order to continue the miniaturization of integrated circuits well into the next future, present day, micron-scale or microelectronic device designs would have to replaced with new designs for devices that take

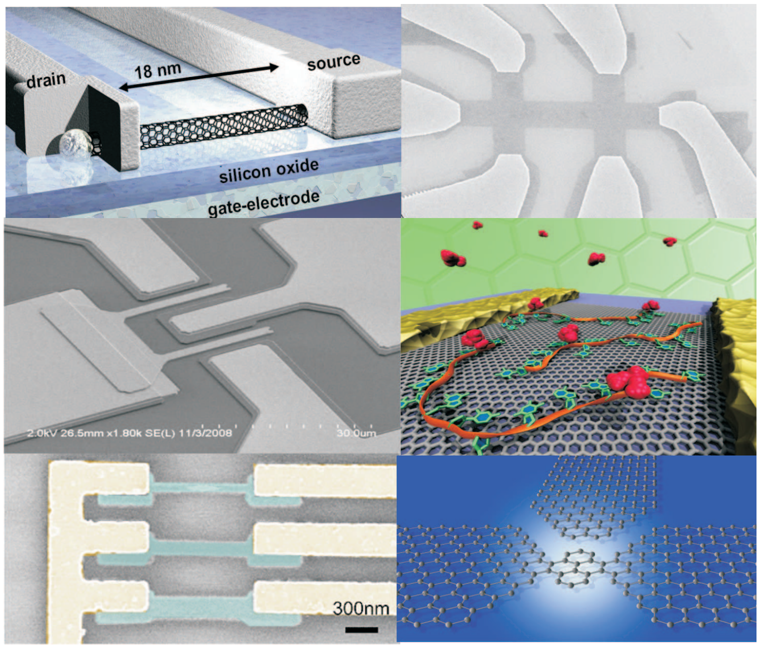

Figure 1.1: Carbon based electronic devices [2–5]

advantage of the quantum mechanical effects that dominate on the much smaller, nanometer scale. This led to rigorous research by scientists over varying disciplines coming together to understand the fundamental science at the nanoscale and thereafter applying this knowledge towards building functional nano-electronic devices. This technology promises of numerous applications beyond faster, smaller and more efficient computers. Cheaper and more powerful solar and fuel cells, to advance the usage of renewable sources of energy and point-of-care medical sensors, to enable cheaper and easier detection of dangerous diseases are also some of the potential venues of application.

1.1 Carbon based Nanoelectronics

Carbon has been heralded as one of the most promising materials to function as the successor for Silicon in the electronics industry. Nanostructures of this element have generated interest ever since Buckyballs (C60) [6] were experimentally observed. They offer the advantage of retaining the FET architecture but replacing the conducting channel, with carbon nanomaterials such as one-dimensional (1D) CNTs [7] or more recently by two-dimensional

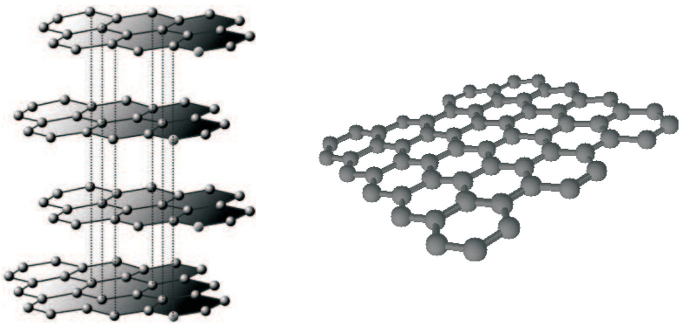

Figure 1.2: Graphene can be obtained by breaking the Van der walls bonds between the layers of graphite

(2D) graphene layers, which have outstanding electrical properties [2].

The superior properties of these nanoallotropes of carbon make them attractive for various electronic applications. Although carbon nanotubes are probably one of the most investigated materials in the past decade, the demonstration of an electrical field effect in single layer graphite or graphene [2] has opened a new and exciting field of research and development of carbon based electronic devices (Fig.1.1)

1.1.1 Graphene

Pure carbon naturally forms two different crystalline materials: diamond, in which all bonds between carbon atoms are the same, and graphite, with two different types of bonds between the atoms. In the case of the latter, a strong covalent bond exists between the hexagonally arranged sheets of sp^2 hybridized carbon atoms within each layer and weaker van der Waals interaction between these hexagonal carbon sheets. Graphene is the pure 2D form of carbon that exists as a single sheet of carbon atoms i.e, an isolated layer from the stack of carbon sheets in graphite (Fig. 1.2).

The experimental isolation of single-layer graphene, during the initial years has provided access to a large amount of fascinating physics [8,9]. Initial studies included the observation of an ambipolar field effect in graphene, [2] the quantum Hall effect at room temperature [10–12], measurements of extremely high carrier mobility [13–15], and even extremely sensitive detection of single molecule adsorption events [16]. The discernment of these properties generated huge interest in the possible implementation of graphene in novel applications. These include future generations of high-speed and radio frequency devices, thermally and electrically conductive composites, sensors, and transparent electrodes for displays and solar cells.

The unique properties of graphene stems from its purely two-dimensional

(2D) lattice structure which has interested researches for many decades. Its electronic structure can be derived by a simple nearest-neighbor, tight-binding approximation [17]. Graphene crystallizes in a triangular lattice with two atoms per unit cell, A and B, with $\vec{a}_1 = (\frac{\sqrt{3}}{2}a, \frac{1}{2}a)$ and $\vec{a}_2 = (\frac{\sqrt{3}}{2}a, -\frac{1}{2}a)$, where a is the lattice parameter ~ 2.46Å. Within the tight-binding method the two-dimensional energy dispersion relations of graphene can be calculated by solving the eigen-value problem for a Hamiltonian $H_{\mathrm{g-2D}}$ associated with the two carbon atoms in the graphene unit cell(Fig. 1.3) [18]. The solution yields the following:

$$E^{\pm}_{\mathrm{g-2D}}(\mathbf{k}) \;=\; \pm\, t\sqrt{1 \;+\; 4cos\left(\frac{\sqrt{3}k_x a}{2}\right)\cos\left(\frac{k_y a}{2}\right) \;+\; \cos^2\left(\frac{k_y a}{2}\right)} \quad (1.1)$$

where the $E^{+}_{\mathrm{g-2D}}$ and $E^{-}_{\mathrm{g-2D}}$ correspond to the π^* and the π energy bands, respectively. Figure 1.3(b) shows the electronic energy dispersion relations for graphene as a function of the two-dimensional wave-vector $\mathbf{k}$ in the hexagonal Brillouin zone, where band crossing occurs at the K and K′ points. Near these crossing points, the electron energy is linearly dependent on the wave vector (Fig. 1.3).

An important feature of the graphene energy dispersion which also makes it attractive for research is its resemblance to the Dirac spectrum for massless fermions[†] [19]. Thus, the charge carriers in graphene are described by a Dirac-like spectrum, rather than the usual Schrödinger equation for non-relativistic quantum particles. This arises as a consequence of graphene's crystal structure. Quantum-mechanical hopping between the sublattices A and B leads to the formation of two energy bands, and their intersection near the edges of the Brillouin zone yields the conical energy dispersion. As a result, quasi-particles in graphene exhibit a linear dispersion relation $E = hk\nu_F$, as if they were massless, relativistic particles analogous to photons. However, the particles in graphene travel at the Fermi velocity $\nu_F \sim c/300$ instead of the speed of light. Because of the linear spectrum, one can expect that quasiparticles in

---

[†] The Dirac equation describes relativistic quantum particles with spin 1/2, such as electrons.The essential feature of the Dirac spectrum, following from the basic principles of quantum mechanics and relativity theory, is the existence of antiparticles. More specifically, states at positive and negative energies (electrons and positrons) are intimately linked (conjugated), being described by different components of the same spinor wave function. This fundamental property of the Dirac equation is often referred to as the charge-conjugation symmetry.

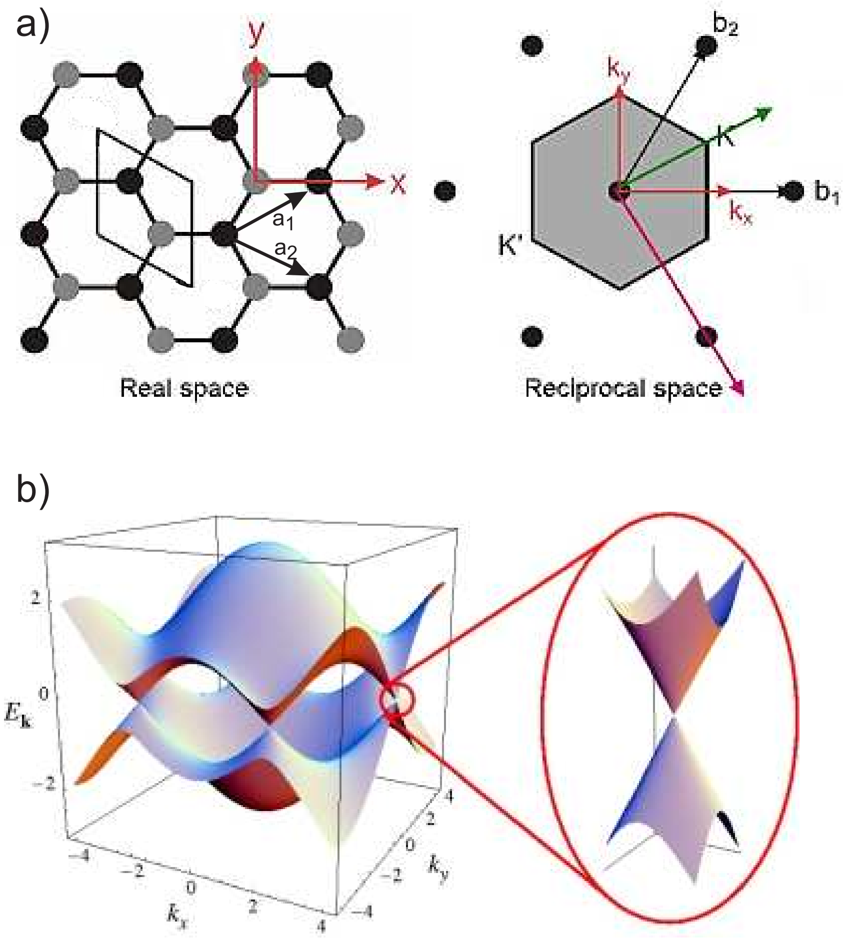

Figure 1.3: (a) The lattice structure and Brillouin zone of graphene with its unit cell consisting of the two inequivalent carbon atoms depicted inside the rhombus (black and grey circles). a_1, a_2 and b_1, b_2 are the unit vectors (in real and reciprocal space respectively).(b) Electron band structure in graphene. Near K and $K^{'}$ the dispersion relation is linear.

graphene behave differently from those in conventional metals and semiconductors, where the energy spectrum can be approximated by a free electron picture. This linear dispersion relationship also means that quasi-particles in graphene display properties quite different to those observed in conventional three-dimensional materials. For example, graphene displays an anomalous half-integer quantization of the Hall conductivity [20], [21]. The quantum Hall effect in graphene can be observed even at room temperature [22].

Graphene's linear energy dispersion is not the spectrum's only essential

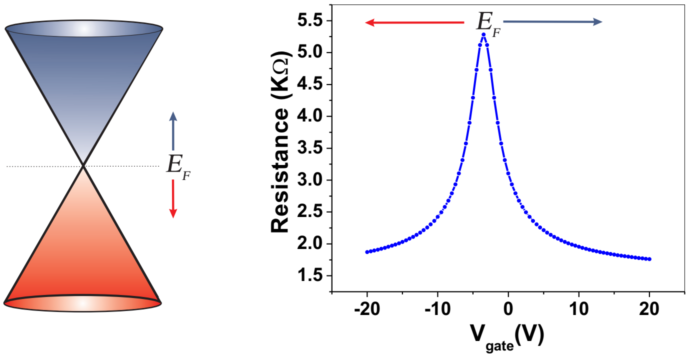

Figure 1.4: Electric field effect of a graphene device. The Fermi level of graphene (hence its doping level) is modulated using a gate field. A peak in resistance is observed when the Fermi level coincides with the Dirac point(zero density of states)

.

feature. The π^* and the π bands of graphene are degenerate at the K points of its reciprocal lattice (Dirac Point), where the Fermi level is located. Therefore, graphene behaves as a semi-metal. This term stems from the fact that the valence band is completely filled and conduction band empty at absolute zero temperature. Controlling the position of the Fermi level (with respect to the Dirac point) by applying an electric field results in the modulation of the sheet resistance as shown in Fig. 1.4. A conductivity minimum is observed when the Fermi level is aligned with the Dirac point. Charge carrier mobility in graphene show unprecedented values on the order of 10,000 $cm^2V^{-1}s^{-1}$ [2,20,21]. (Highest values of mobility ∼200,000 $cm^2V^{-1}s^{-1}$ have been reported for suspended graphene samples [23] which exhibit a ballistic transport regime in the length range of ∼ 0.3μm). These properties of graphene make it very attractive for application in electronics.

1.1.2 Synthesis of Graphene

For a long time, graphene, was considered thermodynamically unstable. Its isolation on a SiO_2 substrate and identification using optical interference contrast [2] triggered the search for techniques of producing graphene by different means. The state of the art in production techniques are detailed below.

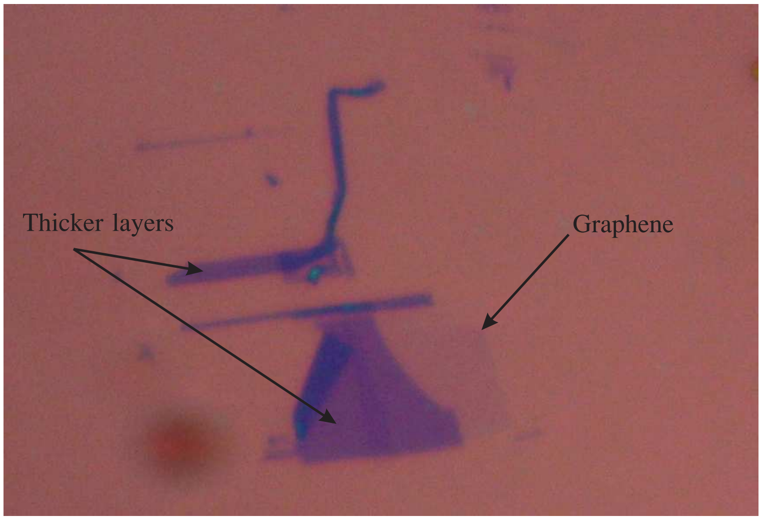

Figure 1.5: Single- and Multilayered graphene imaged by an optical microscope.

1.1.2.1 Micromechanical Cleavage

This technique involves the repeated pealing of layers of graphite. An adhesive tape is used to peel off layers from the surface of HOPG and subsequent peeling eventually leads to a single layer of graphite on the surface of a substrate like silicon oxide. Single layers of sizes up to 10 μm in size and thicker multilayer films (two or more layers) of around 100μm have been reported [2]. These sheets are visible under an optical microscope (figure 1.5) due to an optical interference contrast. This method although very crude has proven to be very reliable and has been used for various investigations [2, 10, 11]. However, the yield of single layers obtained by this technique is very low (a few graphene monolayers per mm^2 of substrate area).

Research on improving the yield of exfoliated single layers have led to many variants of the exfoliation technique [24, 25]. An example shown in figure 1.6 illustrates the transfer printing of graphene from a graphite crystal using a poly-dimethyl siloxane (PDMS) stamp. This technique, follows the same principle as tape exfoliation, but provides the advantage of controlled placement of the sheets. However, the size and yield of single layer graphene still remains a bottleneck in this process.

1.1.2.2 Epitaxial Graphene from Silicon Carbide

Growth of graphitic thin films on silicon carbide is well known [26, 27]. Specifically they grow on the 0001 (silicon-terminated) and $000\overline{1}$ (carbon-terminated) faces of $4H$- and $6H$-SiC crystals upon heating to about 1300

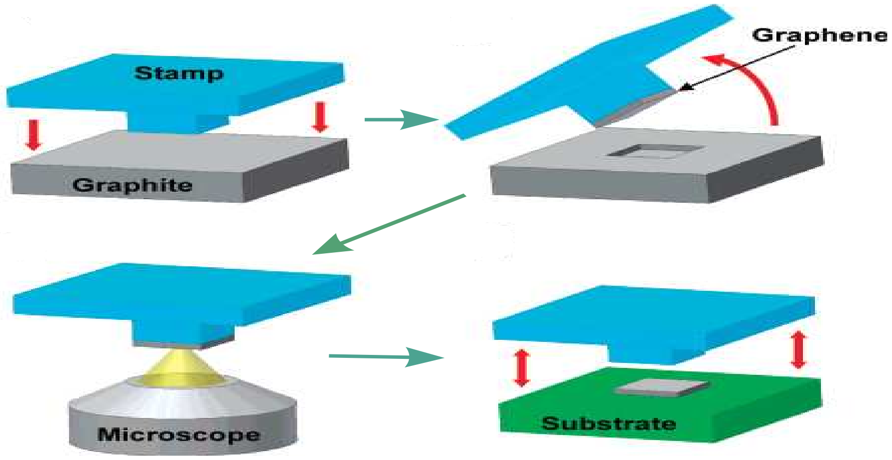

Figure 1.6: Transfer printing of graphene layers using a PDMS stamp. Process flow: The PDMS stamp is pressed on the graphite substrate. The stamp cuts and attaches a piece of graphene using its protrusion edge, and then the separation of the stamp from the graphite exfoliates the cut graphene sheet. Inspect the quality of the graphene sheet that is attached on the stamp protrusion and if the graphene is good, transfer the graphene sheet onto the device active-area of the required substrate.

$^{\circ}C$ in ultra-high vacuum (UHV). It is also possible to grow these films under less demanding vacuum conditions using ovens with controlled background gas. However, it was not until experiments by Walt de Heer et al. [28] that this technique was used to synthesize graphene. On both the silicon and carbon terminated face the graphene formation occurs via the solid state decomposition of SiC (0001) (figure 1.7 (a)) whereupon silicon sublimes to produce carbon rich regions on the surface that subsequently combine to form graphene. However, this technique does not produce atomically thin single graphene layers, rather it produces epitaxially ordered stacks of graphene. Although the graphene obtained in the way is not structurally perfect, it shows electrical properties comparable to that of mechanically exfoliated graphene. In magnetotransport measurements it exhibited mobilities in the range of 20000 $cm^2V^{-1}s^{-1}$ [29]. Furthermore, the charge carriers in epitaxial graphene are also found to be chiral and a band structure similar to that of graphene [29].

However, on the C-face of the SiC substrate it seems much more difficult to control the number of layers during growth, and only layers of low homogeneity are accessible. This drawback was overcome to a certain extent when de Heer et al. used a furnace growth technique combined with an inert gas flow at higher temperatures which yielded graphene from monolayers to

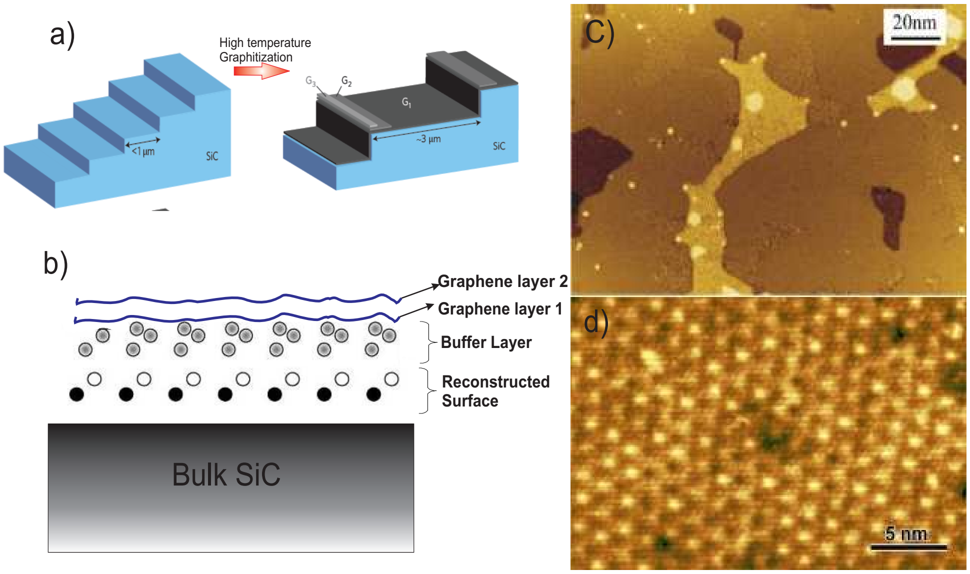

Figure 1.7: (a) Schematic representation of the evolution of the $SiC(0001)$ face starting with a staircase of atomically high steps and flat terraces upon which islands of graphene and its multilayers are formed when subjected to high temperatures under UHV or inert atmosphere. (b) A schematic model of the graphene/SiC interface. On the bulk SiC crystal a surface reconstruction exists on the last layer. An interface layer (layer-0 or buffer layer) between the bulk and the graphene film separates the grown graphene film from the SiC substrate. (c) Scanning Tunneling Microscopy image of nominally 1 monolayer epitaxial graphene on $SiC(0001)$ showing large flat regions of reconstruction and regions where the reconstruction has not fully formed. Islands of grown graphene layer are also seen. (d) A region of surface reconstruction, imaged through the overlying graphene layer [28].

thick slabs [28]. In order to grow homogeneous mono- and few-layer graphene on $SiC(0001)$, a suitable approach is to anneal the SiC samples at temperatures above 1600 $°C$ in an Ar atmosphere in a quartz glass reactor [30]. Furthermore, it has recently been demonstrated that it is also possible to grow graphene on both SiC faces with an additional carbon supply similar to molecular beam epitaxy using relatively low temperatures of around 950 $°C$ [31].

The structure of epitaxial graphene has been as subject of intense debate ever since its invention. Figure 1.7(b) illustrates a structural model summarizing the results of many experiments. For graphene grown on the silicon face of silicon carbide, the interface terminates in a carbon rich layer called the buffer layer [32, 33]. While the exact atomic structure of this layer is not known its atomic density is close to that of a graphene monolayer [34, 35]. Its bonding with the silicon carbide substrate is strong enough to create a bandgap so that this layer does not contribute to the transport [32]. The buffer layer isolates the grown graphene sheet from bonds to the silicon carbide substrate [36]. The graphene layer on top of the buffer layer is the first to display the characteristic graphene structure [37]. Upon continuing growth, a second layer is formed on top of the first layer which exhibits parabolic electronic dispersion consistent with that of bi-layer graphene. The electronic structure finally converges to that of bulk graphite if the number of layers are increased. The final graphite structure exhibits Bernal stacking [38–40].

1.1.2.3 Graphene grown on transition metal surfaces using Chemical Vapour Deposition (CVD)

The growth of graphene on transition metal surfaces has attracted strong interest in the recent past. Chemical vapour deposition (CVD) processes to grow carbon nanotubes have been immensely successful over the years in producing tubes with high quality and high yield [41, 42]. The basic technique (as depicted in Figure 1.8) to fabricate a single graphene layer using CVD is similar to that for CNTs. The process begins with an atomically flat surface of a transition metal substrate and an appropriate carbon precursor (like in methane or ethylene). The metal substrate plays the role of catalyst. This substrate is placed in a heated furnace and is attached to a gas delivery system. The precursor molecules will be brought into contact with the substrate surface from the gas phase (low pressure) or from liquid phase at elevated temperature. Upon contact with the surface, the precursor molecules are cracked to form carbon atoms and form gas-phase species, leaving the carbon atoms (which are free of functionalities) attached to the substrate surface. Graphene is formed when carbon atoms after diffusion on the metal surface, encounter other carbon atoms and form bonds. In order to obtain the lowest energy single layer i.e., graphene, the conditions have to be carefully controlled. Thus, there have been a variety of reports on the different combinations of metal substrate, precursor gas and growth conditions, few of which shall be elucidated in the following.

Initial observations of CVD growth of graphene were made on Ir(111) [43] or Ru(111) [44] using an ethylene source under ultra high vacuum (UHV) conditions. At high temperatures islands of graphene of the order of 200 μm have been observed to nucleate by surface segregation of carbon upon cooling from a metastable carbon-metal solid solution (see figure 1.9 (a) and (b)). Although this process enables the growth of graphene monolayers, a fundamental issue lies in the interaction of the deposited graphene with the metal substrate. The first graphene layer formed, couples strongly to the Ru substrate, the second layer is essentially decoupled and largely recovers

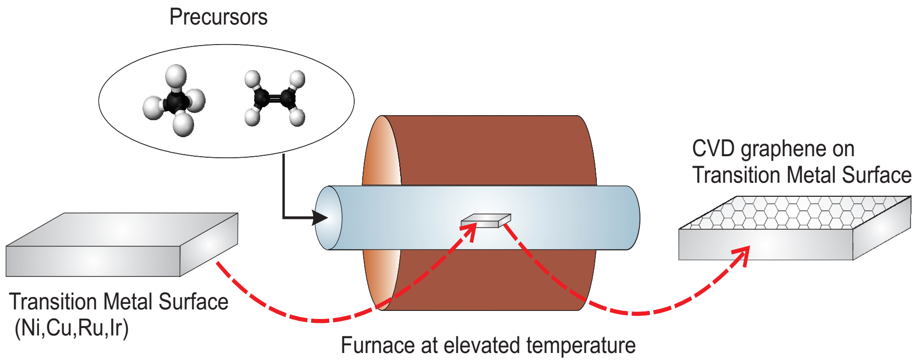

Figure 1.8: Schematic illustration of the growth process for the synthesis of graphene using Chemical Vapour Deposition (CVD).

the electronic structure of free-standing graphene quite similar to graphene grown epitaxially on SiC substrates [44]. Furthermore, carbon solubility in the metal and the growth conditions determine the deposition mechanism which ultimately also defines the morphology and thickness of the graphene films.

Optimization of the aforementioned process over the years has triggered interest in growth of graphene on relatively inexpensive polycrystalline Ni [45–47] and Cu [48] substrates. The CVD approach to graphene (figure 1.9 (c)) on Ni relies on dissolving carbon into the substrate, and then forcing it to precipitate out by cooling. The thickness and crystalline ordering of the precipitated carbon is controlled by the cooling rate and by the concentration of carbon dissolved in the nickel. Graphene deposited on polycrystalline Ni have been successfully transferred onto insulating substrates like SiO_2 via a transfer process using a PDMS stamp as previously described. Measurement of electrical characteristics of the transfered sheets yield mobility values of up to 3650 $cm^2V^{-1}s^{-1}$ and half-integer quantum Hall effect [45]. However, the fundamental limitation of utilizing Ni as the catalyst is that regions of single and few layered graphene spanning over few to tens of microns are obtained but they are quite inhomogeneous over the entire substrate [46]. The lack of control over the number of layers is partially attributed to the fact that the segregation of carbon from the metal carbide upon cooling occurs rapidly within the Ni grains and heterogeneously at the grain boundaries.

Growth of graphene on Cu substrates has by far shown the best results in terms of uniform deposition of high quality single layered graphene over large areas [48]. Studies have demonstrated the growth of single layered graphene over areas as large as 30 inches [49–51]. Detailed imaging and spectroscopic analyses have revealed that independent of growth time or heating and cooling rates, over 95% of the copper surface is covered by single layered graphene

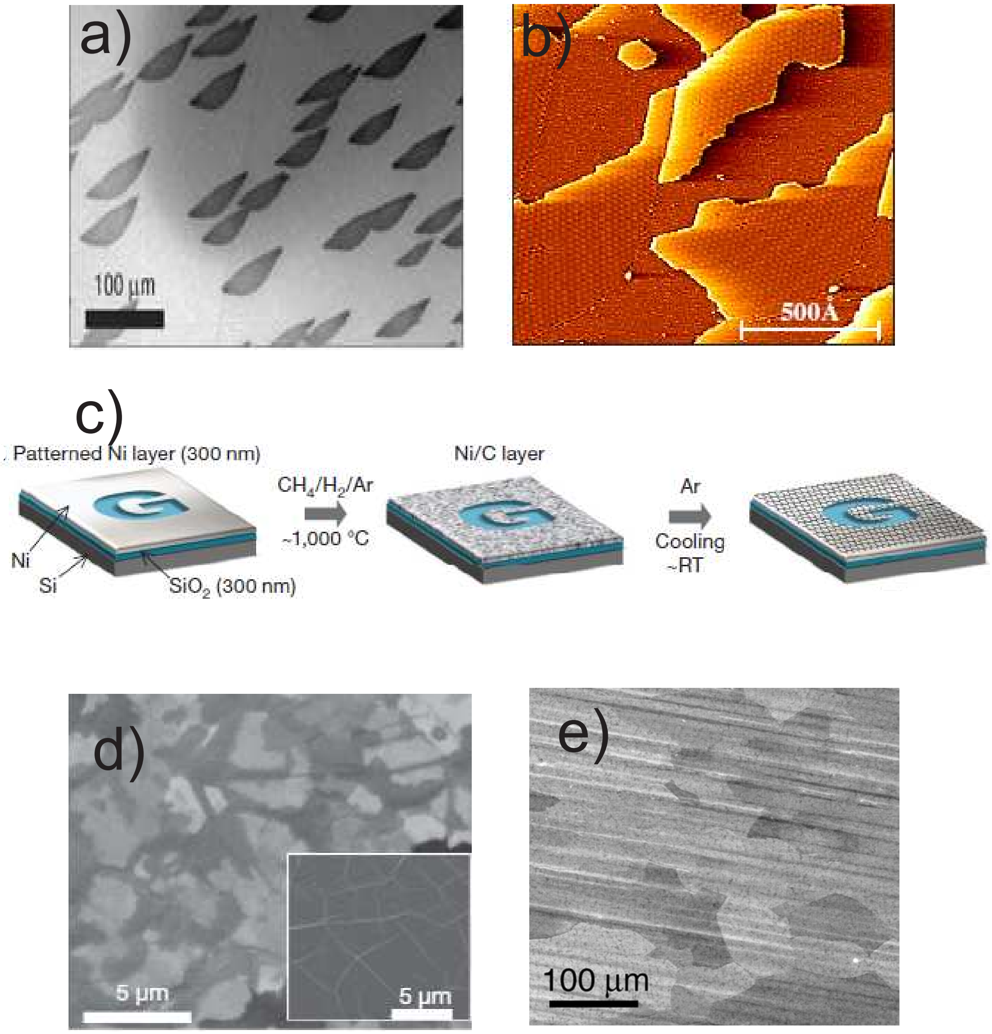

Figure 1.9: (a) Scanning Electron Microscopy image of graphene islands grown on Ru(111) [44]. (b) STM topography image of graphene on Ir (111) [43]. (c) Process flow illustration for segregation of graphene on Ni surface [45]. (d)SEM image of graphene grown on Ni [45]. (e) SEM image of graphene grown on Cu [48].

while the remaining graphene is 2-3 layers thick [48]. CVD of graphene on copper is a relatively simple process, involving the decomposition of methane gas over a copper substrate typically held at 1000 $°C$.

Monolayer graphene synthesis on copper foil has recently been reported using liquid precursors like hexane at 950 $°C$ [52] and also using solid sources like poly(methyl methacrylate) (PMMA) at 800 $°C$ (sources like fluorene and sucrose have also been studied) [53]. Although the described CVD methods provide access to large area graphene, the challenge remains to obtain fine control over film thickness and crystallinity. Ideally this method should allow the growth of a single crystal of graphene all over the susbtrate without the formation of a boundary or seeding a secondary layer. In practice, however, graphene grown using CVD on metal substrate is always polycrystalline consisting of many grain boundaries (figure 1.9(d) and (e)).

1.1.2.4 Solution based exfoliation and synthesis of graphene

A common issue in the described CVD techniques is the use of metal substrates which often necessitates a transfer of the graphene onto insulating substrates. Moreover, the mechanical exfoliation technique does not provide a high enough yield of monolayers. A possible solution to circumvent the above problems is the use of solution based techniques to separate the layers of graphite thus yielding a suspension of graphene. There have been numerous approaches explored in this regard, all of which follow the same underlying principle of liquid phase exfoliation by weakening the van der Waals interaction between the layers of graphite by either intercalation or functionalization of the individual layers. This approach is both scalable, affording the possibility of high-volume production, and provides versatility in terms of being well-suited to chemical functionalization. It is hence promising for a wide range of applications.

Graphite intercalation compounds or expandable graphites are interesting starting materials to obtain colloidal dispersions of single layer graphene sheets. Ideally this approach should allow the production of high quality single layer sheets of graphene. Colloidal suspensions of graphene sheets in organic solvents such as N-methylpyrrolidone (NMP) were obtained by sonication of graphite powder, however, only with lateral sizes of a few hundreds of nanometers and quite low yield [55]. Electrical sheet resistivity measurements on very thin films made from these sheets yielded, for example, an electrical conductivity of 6,500 Sm^{-1} at 42% of optical transparency. In addition, even after the films had been dried at 400 °C, residual NMP had not been completely removed and was estimated to be 7% by weight. A milder dissolution route has also been reported wherein starting from neutral graphite and avoiding any kind of sonication one could obtain large size graphene flakes. This was achieved by stirring the ternary potassium salt ($K(THF)_xC_{24}$) (a graphite intercalation compound) in NMP [56]. Polymer coated graphene sheets were synthesized from thermally treated, commercial expandable graphite at high temperature by sonication in a dichloroethane solution of (poly(m-phenylenevinylene-co-2,5-dioctoxy-p-phenylenevinylene) (PmPV) [57]. Another approach (illustrated in Figure 1.10) was intercalation with oleum and expansion with (tetrabutylammonium hydroxide)(TBA).

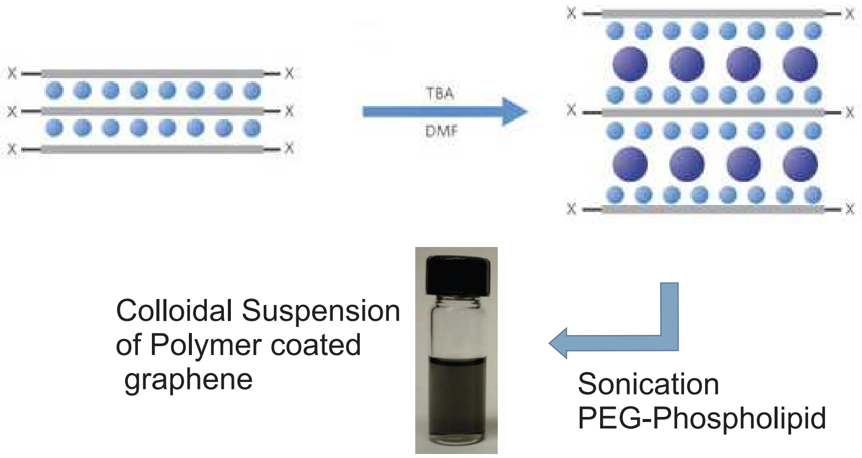

Figure 1.10: Schematic depiction of the exfoliation of graphite intercalated with sulphuric acid (oleum) (light blue) between the layers followed by the insertion of TBA (dark blue) intercalate. Upon sonication in the phospholipid polymer, the intercalated material yields a dark colloidal suspension of separated graphene sheets. [54]

The final suspension of graphene sheets, coated by (1,2-distearoyl-sn-glycero-3-phosphoethanolamine-N-[methoxy(polyethyleneglycol)-5000] (DSPE-mPEG), was produced by sonication in DMF, with $\sim$ 90% of the sheets reported as individual modified graphene sheets [54].

There have been numerous other efforts on producing stable colloidal suspensions of graphene by exfoliation in liquids [58–60]. However, one of the most promising, low-cost, up-scalable and widely studied synthetic approaches so far has been the reduction of oxidized layers of graphite which can be deposited with controllable density onto a wide range of substrates. The underlying principle of this method is illustrated in fig. 1.11.

The synthesis of graphite oxide itself was first reported in the nineteenth century [61–63]. Since then, graphite oxide has been mainly produced by the Brodie [61], Staudenmaier [63] and Hummers [62] methods. These methods involve oxidation of graphite in the presence of strong acids and oxidants. The degree of oxidation can be controlled by varying the reaction method, synthesis conditions and the precursor graphite used. Although extensive research has been done to determine the chemical structure of graphite oxide, several models are still being debated in the literature. An early interpretation of the structure proposed that the oxygen is bound to the carbon atoms of the hexagonal layered planes by epoxide (C_2O) linkages (Hofmann) [64].

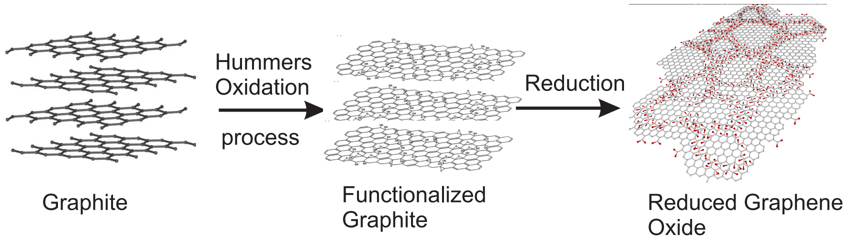

Figure 1.11: Graphical illustration of the principle of conversion of graphite to graphene oxide.

The planarity of the graphite layers was thought to be largely conserved in this case, which was challenged in a later model where a distorted carbon sheet composed of linked cyclohexane chairs is assumed and saturation of the carbon valencies is achieved by bonding to axial $-(OH)$ groups and ether oxygens in 1,3 positions (Ruess) [65]. This model was the first to account for the presence of hydrogen in Graphene Oxide(GO) which was later modified with C=C double bonds, ketonic and enolic groups [66]. In addition, observation of acidity in this material unraveled the presence of in plane enolic $-(OH)$ species and carboxylic groups. This model was then revised in accordance with stereochemical considerations by Scholz and Boehm [67]. Another school of thought proposed a structure analogous to poly fluoro-carbons [68].

The most recent models have focused on a nonstoichiometric, amorphous alternative instead of the lattice-based model. For instance, the model proposed by Lerf et al [69], based on NMR studies, describes GO as randomly distributed regions of unoxidised benzene rings and distorted hexagonal rings bearing $(C = C)$, 1,2-ethers and $-(OH)$ groups. A recent study of the evolution of the surface functional groups upon oxidation led to the model of Scholz et al., involving a few stereochemical modifications [70]. Initial studies done by Lerf and coworkers [69] used solid state nuclear magnetic resonance (NMR) spectroscopy to characterize the material. Recently ^{13}C-labeled graphite oxide based NMR studies indicated that the sp^2-bonded carbon network of graphite is strongly disrupted and a significant fraction of this carbon network is bonded to hydroxyl groups or participates in epoxide groups. Minor components of carboxylic or carbonyl groups are thought to populate the edges of the layers in graphite oxide [71]. Thus, it is quite unclear as to which is the most accurate structural model of graphite oxide.

The oxidation of commercially available graphite aids its exfoliation by rendering a hydrophilic nature to its layers. Although graphite oxide (GO) itself is an insulator, the graphitic network can be substantially restored

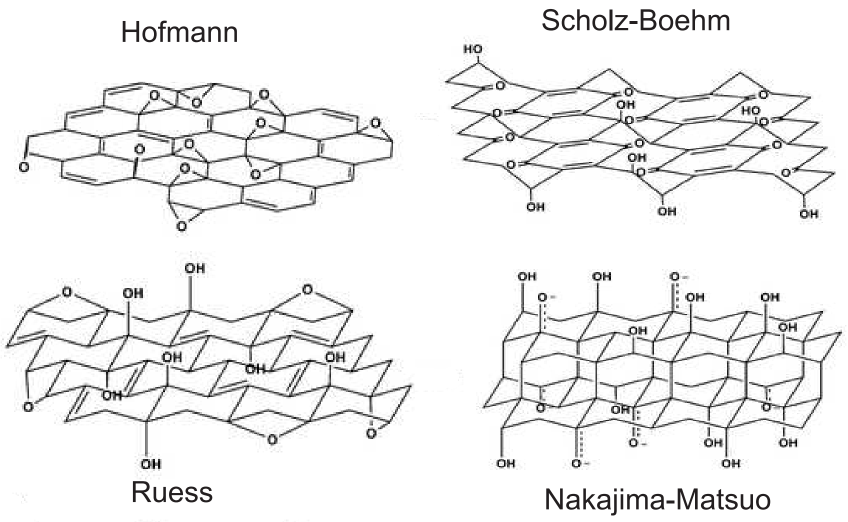

Figure 1.12: Older structural models of graphene oxide

by thermal annealing or treatment with chemical reducing agents. Thus, subsequent reduction produces graphene layers of considerable size and useful electrical conductivity [72, 73], albeit further improvements are required in order to completely eliminate the oxygen containing defects in the carbon lattice. Microscopic and electrical characterizations suggest a structure in which nanometer sized graphene islands are separated by defect rich regions. These regions are small enough that the electrical characteristics of graphene are largely preserved, rendering these sheets useful for electronic applications. The most exciting advantages of this method are its low-cost and potential scalability. The starting material is simple graphite, and the technique can easily be scaled-up to produce gram quantities (or larger) of chemically derived graphene dispersed in liquids. Owing to its superior mechanical properties GO is also an interesting material in its own right for applications in composites. [74, 75].

The following chapters mainly deal with the study of graphene obtained via the oxidation/reduction approach described above. An accurate understanding of the physiochemical structure is essential for the development of graphene synthesized via this technique. To this end, graphene oxide is synthesized from commercial graphite and is extensively investigated using Transmission Electron Microscopy(TEM), Raman spectroscopy and Near Edge X-Ray and Fine Structure (NEXAFS) measurements to clarify its physiochemical structure. Further studies in this work are targeted towards electronic devices fabricated using reduced graphene oxide as the active material. Electronic transport analysis was performed in order to understand charge carrier transport across both contact and channel regions of the device. A detailed study of the influence of gold contacts in graphene based devices shall be presented firstly on a carbon-gold system using high quality CVD graphene followed by experiments on the more complex reduced graphene oxide-gold interface. In order improve the electrical properties of such devices, a novel strategy was developed on the basis of chemical vapour deposition. An in-depth evaluation of the structure and electrical performance of the resulting devices provided valuable insights for future applications of this material.

Chapter 2

Experimental Methods

In this chapter, the experimental techniques involved in this thesis are introduced. This work involves the synthesis of graphene by chemical route. A detailed description of the steps involved shall be presented here. Structural analysis of chemically derived graphene was performed using Transmission Electron Micrcoscopy (TEM), Raman Spectroscopy and Near Edge X-Ray and Fine Structure measurements. Electrical transport measurements were made on devices fabricated using e-beam lithography. In order to study the nature of contacts in these devices, Scanning Photocurrent Microscopy was used.

2.1 Preparation of chemically derived graphene sheets from graphite

2.1.1 Oxidation of graphite

Graphite oxide preparation has been known since 1859 [61] by the treatment of natural graphite with potassium chlorate and fuming nitric acid. This method, however, is time consuming and hazardous. Thus in this work the graphite oxide was prepared using the well established Hummers method [62] which uses a combination of potassium permanganate and sulfuric acid. Though permanganate is a commonly used oxidant, the active species in the oxidation process is in fact diamanganese heptoxide (Mn_2O_7). The bimetallic heptoxide is known to vigorously react with organic compounds [76,77]. The most common source of graphite used for chemical reactions, including its oxidation, is flake graphite which is the starting material used for this work. As such, it contains numerous, localized defects that may serve as seed points for the oxidation process. The experimental steps towards the preparation

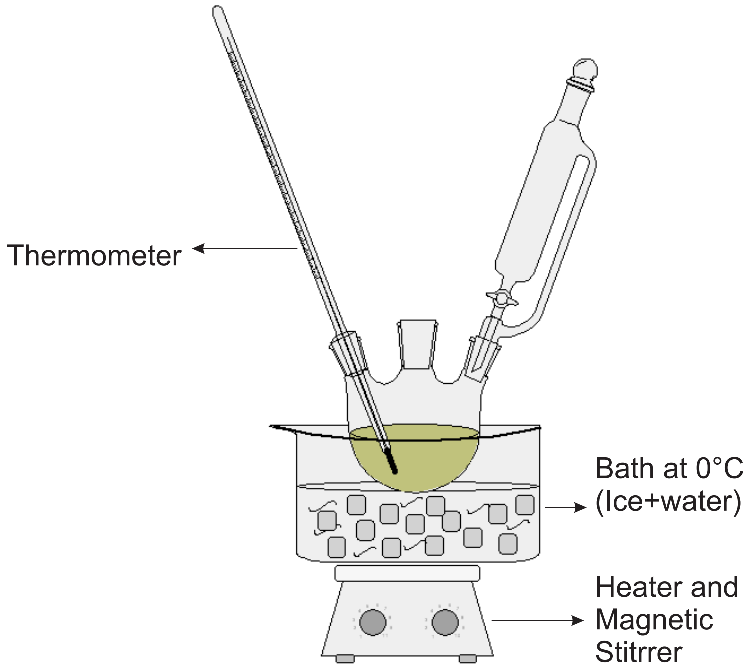

Figure 2.1: An illustration of the setup used for preparation of graphite oxide.

of graphite oxide starting from graphite have been outlined below:

- 23 ml of 98% H_2SO_4 was taken in the round bottomed flask as shown in figure 2.1, and 1 g of graphite powder (200 μm sized flakes) was added under constant stirring.
- To this mixture, 0.5 g of $NaNO_3$ was added and the speed of stirring was increased.
- 3 g of $KMnO_4$ was added carefully so that the temperature did not rise above $\sim$ 20°C.
- Upon removing the iced water bath, the temperature rose to $\sim$ 35°C in 30 minutes, leaving a brownish grey paste.
- 46 ml of deionized water was then added and the temperature rose to $\sim$ 98°C where it was maintained for 15 minutes.
- 70 ml of warm water was then added.
- 3% H_2O_2 was added slowly until the solution turned bright yellow.

- The suspension was vacuum filtered resulting in a yellow brown filtrate which was washed several times with of dilute HCl and warm water.

2.1.2 Exfoliation of graphite oxide

Upon oxidation, graphite is functionalized with oxygen containing groups as described earlier. This results in the weakening of the van der Waals forces between the layers, and thus facilitates exfoliation in aqueous solutions. This step has been previously demonstrated by rapid thermal heating (> 2000 °C /min) to 1000 °C, whereupon the GO is split into individual sheets through the fast evolution of CO_2 [78]. Here, by contrast the exfoliation was performed either by a mild ultrasonication or shaking technique. The obtained graphite oxide suspensions in water were placed in an ultrasonic bath for ∼10 minutes and then centrifuged at 3000 rpm for 3-4 minutes. Only mild ultrasonication was necessary to exfoliate the sheets. Higher powers of ultrasonication completely destroyed the sheets leaving only small flakes of graphite. The time of ultrasonication also seemed to have an important effect on the size of the obtained flakes. Smaller times yielded more intact and larger flakes. The resultant supernatant had a brownish yellow tinge. The average size of the flakes improved further by using a milder approach which involved shaking the aqueous solutions of GO over several hours.

2.1.3 Deposition of graphene oxide sheets on substrates

The deposition of GO sheets was done by simply drop casting the above suspension onto different substrates, as illustrated in figure 2.2(a). Degenerately doped silicon substrates with a 300 nm thick, thermally grown SiO_2 were employed. After thorough cleaning in acetone, 1-methyl-2-pyrrolidinone (NMP) and iso-propanol, the substrates were functionalized by 3-(aminopropyl)triethoxysilane (APTES) prior to deposition. This step is necessary in order to render the hydrophobic SiO_2 surface conducive for deposition of GO. The drops were left on the substrate for <2 minutes after which it was dried under N_2 flow. A commercially available Atomic Force Microscope (AFM) (Digital Instruments Inc., Multimode SPM Nanoscope III) was used for topographical characterization of these samples. AFM height images depicted in figure 2.2(b) revealed GO sheets with lateral dimensions of 5-30 μm and heights in the range of 1 ± 0.5 nm. The slightly larger value of the sheet height compared to the theoretical value of 0.8 nm [78] has been observed also by other AFM studies [78, 79] and assigned to individual graphitic sheets bearing oxygen-containing groups on both faces.

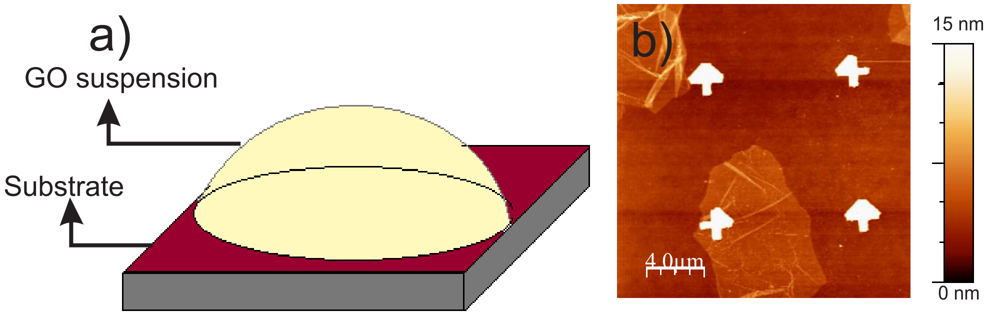

Figure 2.2: (a) Schematic representation of a GO suspension resting on the substrate. (b) AFM image of GO sheets deposited on a Si/SiO_2 substrate.

2.1.4 Reduction of graphene oxide

While graphene oxide itself is insulating, its carbon framework can be substantially restored by thermal annealing or treatment with chemical reducing agents. Earlier efforts mainly involved the use of hydrazine vapor for this purpose [80]. The use of hydrazine, however, requires great care because it is both highly toxic and potentially explosive. Therefore, there have been a number of alternative techniques explored.

Sodium borohydride ($NaBH_4$) was recently demonstrated to function more effectively than hydrazine as a reductant of graphene oxide [81]. Though $NaBH_4$ is slowly hydrolyzed by water, this process is kinetically slow enough that freshly prepared solutions, still function effectively as reductants of graphene oxide. Several other reductants have also been used for the reduction of graphene oxide including hydroquinone [82], gaseous hydrogen [83], vitamin C(ascorbic acid) [84] and strongly alkaline solutions [85]. For most of the experiments of the current thesis however, a simpler yet equally effective route for reduction of GO has been employed. Specifically, the sheets were exposed to hydrogen plasma for ~ 5 seconds at a pressure of 0.8 mbar at a power of 30 W, which achieved results comparable to other chemical reduction methods.

Further improvements in the reduction of GO were obtained by thermal annealing the sheets in vacuum or an inert atmosphere (eg, argon). A recent study of the effects of this method revealed a strong effect of temperature [86]. In the current work a thermal annealing step was carried out on the plasma reduced sheets at a temperature of 400 °C in an argon atmosphere.

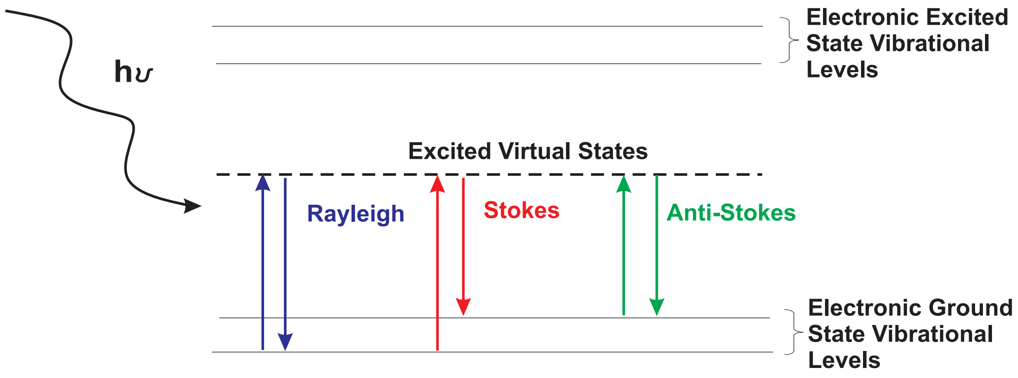

Figure 2.3: Graphical representation of the various light scattering processes. Energy is conserved in Rayleigh scattering, while for Stokes and Anti-Stokes scattering there is an energy decrease and increase, respectively.

2.2 Structural Characterization

2.2.1 Raman Spectroscopy

Raman spectroscopy has long been recognized as a valuable technique since the phenomenon was first observed by Sir C. V. Raman in his Nobel prize winning work in 1928. However it is only fairly recently that Raman has emerged as an important analytical tool across a number of industries and applications. The technique is based on inelastic light scattering or the "Raman Effect", initially observed in molecular liquids [87, 88]. When such a sample is irradiated with an intense monochromatic light source (usually a laser), most of the radiation is scattered by the sample at the same wavelength as that of the incoming laser radiation in a process known as Rayleigh scattering (Figure 2.3). (However, a small proportion of the incoming light (1 in every 10^6 photons) is scattered at a wavelength that is shifted from the original laser wavelength. This is referred to as inelastic light scattering.) This shift from the original laser wavelength (or energy) stems from the interaction with excited states of the molecules, which leads to inelastic scattering. The energy difference between the incident and scattered photons correspond to internal energy levels which can be electronic states in atoms and molecules, excitonic states in semiconductors, vibrational and rotational states in molecules, phonon states in crystals, etc.

This inelastic process caused by the quantum phenomena of absorption of one photon and creation of a phonon, thus releasing a photon of lower energy, is called Stokes scattering (figure 2.3). Another form of scattering occurs when a phonon is annihilated and the outgoing photon has more energy than that of the incident photon. This is called the anti-stokes Raman scattering, as depicted in figure 2.3. Both processes can be described using a classical description. However, to obtain an accurate picture of these processes a quantum mechanical treatment is required. An incident electromagnetic wave induces a dipole moment during the light-material interaction. The strength of the induced dipole moment, $\vec{\mu}$, is given by :

$$\vec{\mu} = \alpha \vec{E} \tag{2.1}$$

where α is the polarizability and $\vec{E}$ is the strength of electric field of the incident wave. The polarizability is a material property that depends on the molecular structure and nature of the bonds. The electric field can be expressed as $\vec{E} = \vec{E_0}\cos(2\pi\nu_0 t)$ and the induced dipole moment as $\vec{\mu} = \alpha\vec{E_0}\cos(2\pi\nu_0 t)$. Because the ability to perturb the local electron cloud of a molecular structure depends on the relative location of the individual atoms, it follows that the polarizability is a function of the instantaneous position of constituent atoms. The physical displacement dQ of the atoms about their equilibrium position due to the particular vibrational mode may be expressed as $d\vec{Q} = \vec{Q_0}\cos(2\pi\nu_{vib}t)$, where ν_{vib} is the frequency of the vibrational mode and Q_0 is the maximum displacement about the equilibrium position. A Taylor expansion over the displacement coordinate Q leads to the expression (2.2) that reflects the effect of modulation in polarizability.

$$\vec{\mu} = \alpha_0\vec{E_0}\cos(2\pi\nu_0 t) + \left(\frac{d\alpha}{dQ}\frac{\vec{Q_0}\vec{E_0}}{2}\right)\cos[2\pi(\nu_0 - \nu_{vib})t] + \cos[2\pi(\nu_0 + \nu_{vib})t] \tag{2.2}$$

The above equation reveals that induced dipole moments are created at three distinct frequencies, namely ν_0, $(\nu_0 - \nu_{vib})$, and $(\nu_0 + \nu_{vib})$, and the scattered radiation also comprises of these same three frequencies corressponding to the Rayleigh, Stokes and Anti-Stokes cases respectively.

In recent years, Raman spectroscopy has become an important tool in the study of carbon based nanostructures [89], as it is nondestructive, fast, with high resolution and gives great structural and electronic information. It has thus become the standard also in the fast growing field of graphene. The Raman spectrum of graphene mainly consists of 3 prominent features which are assigned as D (only prominent in the presence of defects), G and 2D bands (figure 2.4).

The G-band 1580 cm^{-1} is the primary mode in graphene and graphite. It represents the planar configuration sp^2 bonded carbon that constitutes

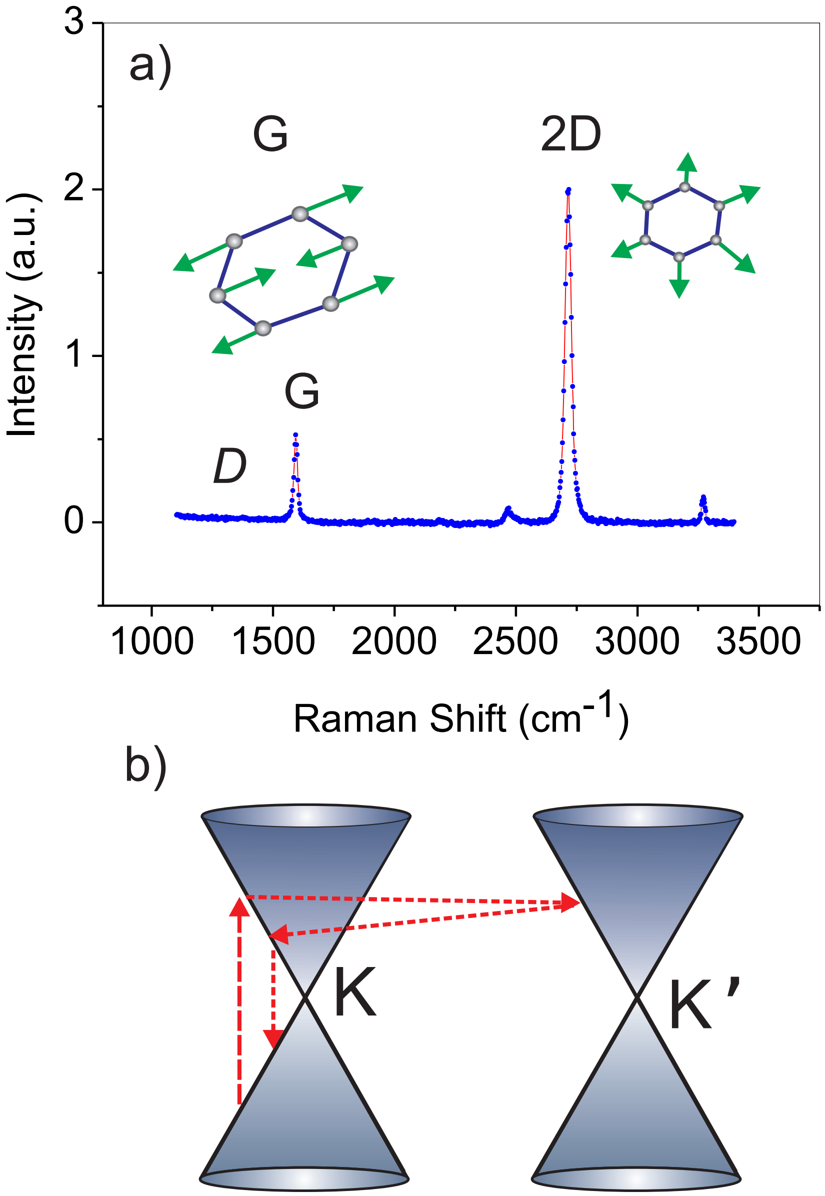

Figure 2.4: (a) Raman spectrum of a graphene sample and a graphical illustration of the molecular vibration modes resulting in the main Raman features, i.e., G and 2D peaks. The D peak is absent in this sample due to the absence of defects (b) A schematic representation of the scattering process required to satisfy the double resonance condition for the 2D (and D) peaks.

graphene and occurs due to the bond stretching (E_{2g}-*symmetry*)of all pairs of sp^2 atoms. In graphene this is a resonant process at the Γ point and is observed as a single Lorentzian peak unless the degeneracy of the mode is broken due to physical constraints.

The D band in graphene originates from the breathing modes of sp^2 atoms in rings and is a probe for the amount of disorder. In the figure 2.4, the D band is virtually nonexistent. This is direct evidence of the absence of a significant number of defects and thus the flawless lattice structure of graphene (exfoliated using micromechanical cleavage). Zone-boundary phonons give rise to this peak at 1350 cm^{-1} in defected graphite [90]. Since they do not satisfy the Raman fundamental selection rule, they are not seen in first order Raman spectra of defect-free graphite [91]. The scattering mechanism of the D peak involves a double resonance process which is a fourth order process, as schematically shown in figure 2.4. Photoexcitation due to the incident laser promotes the electron to a higher energy state followed by the scattering of this electron with a phonon. This phonon then undergoes a defect scattering process which then results in an electron/hole recombination. An important feature is that these scattering processes in graphene are resonant, i.e., electronic transitions occur into real states.

The 2D-band is the second order of the D-band, sometimes referred to as an overtone of the D-band. It is the result of scattering by two phonons with opposite momentum in the highest optical branch near the K point. Unlike the D-band, it does not need to be activated by proximity to a defect. As a result the 2D-band is principally strong in graphene even when no D-band is present, and it does not represent defects. The scattering mechanism is quite similar to the double resonance process of the D band, with the only difference being that the backscattering of the phonon does not occur through a defect but by a second phonon which has an equal and opposite momentum. The resulting 2D Raman frequency is twice the frequency of the scattering phonon and is observed as the most intense peak in the spectrum. This peak is usually a single Lorentzian function and is roughly 4 times as intense as the G peak. This band is also used for determining the number of graphene layers [92].

In practice, Raman spectroscopy is usually performed with a laser as the excitation source because this intense, collimated monochromatic light source enables measurement of relatively small Raman shifts, while simultaneously allowing for improved spatial resolution and signal-to noise ratio. In general, the Raman signal intensity is orders of magnitude weaker than the elastic scattering intensity, hence stray light can be a considerable issue. In the present work, lasers with wavelengths in the visible region of the spectrum have been used. Raman measurements were performed with a scanning con-

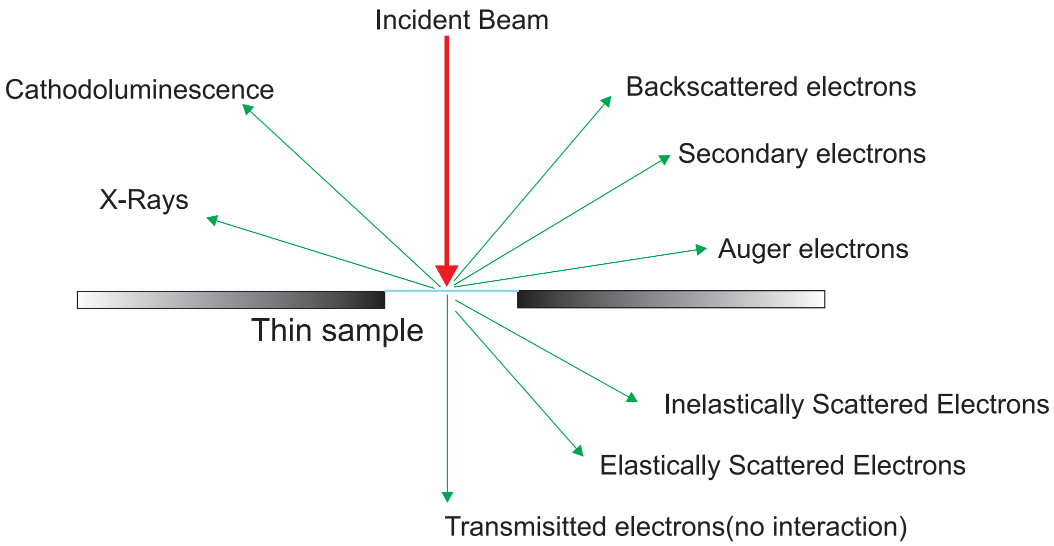

Figure 2.5: Interaction of an electron beam with a sample. Different signals can be extracted and studied for various characterization. In TEM the transmistted electrons are studied through a thin sample

focal setup using a solid-state laser with wavelengths of either 488 nm or 633 nm and an intensity of up to 12 mW focused to a diffraction-limited spot. Acquisition at each position was enabled by dispersing the backscattered light using a monochromator and detecting with a Peltier cooled charge coupled device (CCD) with variable accumulation times.

2.2.2 Transmission Electron Microscopy (TEM)

In a transmission electron microscope, a sample in the form of a thin foil is irradiated by electrons having energy of the order of hundreds of keV. In the interior of the crystal the electrons are either undeviated, scattered (elastically or inelastically), or reflected (Figure 2.5). Elastically scattered electrons interact with the electrostatic potential of nuclei of atoms. This potential disturbs the trajectory of incident electrons without any appreciable energy loss; i.e., only the direction is changed. In fact a small loss occurs because of the change of the momentum. However, because of the disparity of the mass of the scattered electron and the atom the loss is too small ($\Delta E/E_0 \sim 10^{-9}$ at aperture angles used in TEM) to affect the coherency of the beam.

In the inelastic case, energy of the incident electron is transferred to internal degrees of freedom in the specimen in several ways. This transfer may cause excitation or ionization of the bound electrons, excitations of free electrons or lattice vibrations and possibly heating or radiation damage of the specimen. Most common are interactions with the electrons in the crystal. In this case the energy loss $\Delta E^{\dagger}$ is important, because the interacting particles are of the same mass.

TEM also provides access to electron diffraction studies which yield useful crystallographic information from the sample. Data from the TEM are obtained as near-planar sections through k-space. The large electron wavevector provides an Ewald sphere that is nearly flat, allowing the handy approximation that a diffraction pattern from a single crystal is a picture of a plane in its reciprocal space. The magnitude of the diffraction vector, Δk, is obtained from the angle between the transmitted and diffracted beams. A modern TEM provides two modes for obtaining diffraction patterns from individual crystallites. The first is selected-area diffraction (SAD), which is useful for obtaining diffraction patterns from regions as small as 0.5 μm in diameter. The second method is convergent-beam electron diffraction (CBED), in which a focused electron probe beam is used to obtain diffraction patterns from regions as small as 10 Å. Both techniques provide a two-dimensional pattern of diffraction spots, which can be highly symmetrical when a single crystal is oriented precisely along a crystallographic direction.

A variety of material characterization is thus possible using a TEM setup. Among these, high resolution (down to atomic resolution) imaging is one of the most widely used microscopy techniques today. Image formation in a high resolution electron microscope is an interference phenomenon. A parallel, coherent incident beam is diffracted by the thin crystal placed in the object plane of the objective lens (figure 2.6). The lens forms in its image plane a magnified and inverted image $\psi(\vec{r'})$ of the wavefunction $\psi(\vec{r})$ at the exit face of the crystal. In the back focal plane, the electron beams converge and form a Fraunhofer diffraction pattern, representing a Fourier transform $\tilde{\psi}(\vec{q})$ of the wave $\psi(\vec{r})$. The path from the focal plane to the image plane may be described as an inverse Fourier transform. As the illumination of the object is coherent, image O′ of each of the points O results from an interference of several (spherical) waves admitted by the opening of the contrast aperture.

In practice, a transmission electron microscope is constituted of two or three condenser lenses to focus the electron beam on the sample, an objective lens to form the diffraction in the back focal plane and the image of the

---

[†] It is the primary process of excitation which is used for the Electron Energy Loss Spectrometry (EELS). This kind of spectrometry as well as different secondary processes of subsequent de-excitations of the target X-ray emission, Auger electrons emission, cathodoluminiscence etc. permit to link the structural aspect of the specimen with the information about its chemical nature, if the microscope is equipped by appropriate detectors.

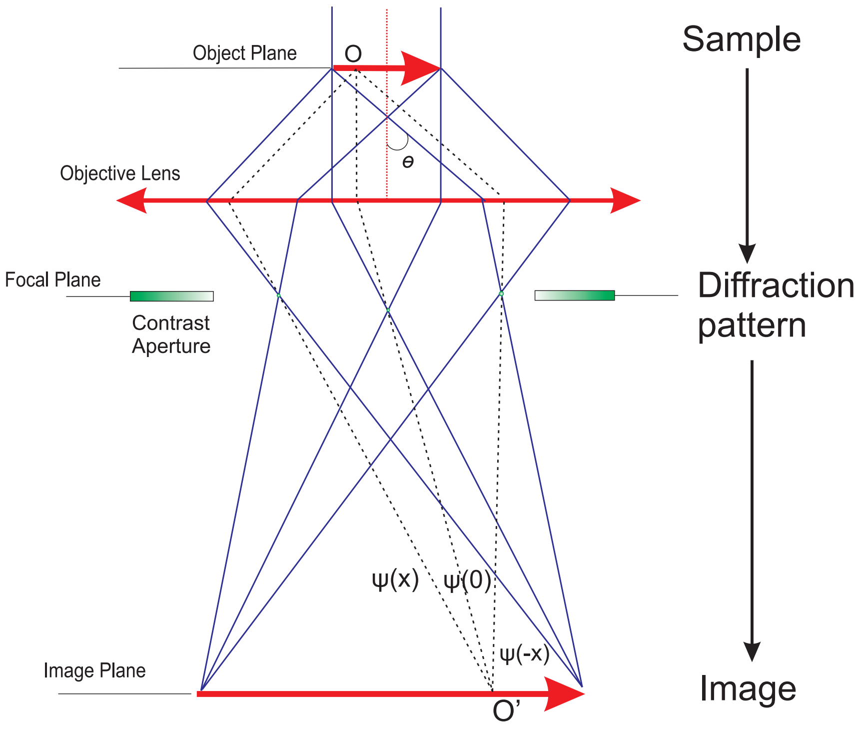

Figure 2.6: Image forming by a lens in TEM without aberrations

sample in the image plane. In addition some intermediate lenses are used to magnify the image or the diffraction pattern on the screen. If the sample is thin ($<$ 200 nm) and constituted of light chemical elements, the image presents a very low contrast when it is focused. To obtain an amplitude contrasted image, an objective diaphragm is inserted in the back focal plane to select the transmitted beam. The crystalline parts in Bragg orientation appear dark whereas the amorphous or not Bragg oriented parts appear bright. This imaging mode is called bright field mode. However, if the diffraction is constituted by many diffracting phases, each of them can be differentiated by selecting one of its diffracted beams with the objective diaphragm. To do that, the incident beam must be tilted so that the diffracted beam is put on the objective lens axis to avoid off-axis aberrations. This mode is called dark field mode.

In spite of the best efforts of lens designers, standard lenses in electron microscopes are far from perfect and posses a host of abberations which need to be corrected in order to achieve a resolution close to the electron wavelength (diffraction limit). The aberrations of real lenses deform the electron waves and decrease the resolution of the microscope. Fortunately, in the transmission electron microscopy one deals with electron beams that propagate close to the optical axis and under small angles to it. Thus, higher order aberrations can be neglected. Nevertheless, a correction has to be made for axial aberrations: defocus, spherical aberration, chromatic aberration, astigmatism and coma.

One of the basic limits to the resolution is determined by the quality of the objective lens and the wavelength, λ, of the electrons used to generate the image. This limit is called the point resolution limit [93] and is given by the formula $\sim C_s^{1/4}\lambda^{3/4}$, where C_s is the coefficient of spherical aberration, and is the main factor that determines lens quality. Rays passing through a spherically aberrated lens at a high angle to the optical axis are brought to a focus closer to the lens than the rays passing along or at a small angle to the optic axis. These incorrectly focused, high-angle rays produce a smearing in the image. Rays scattered to a high angle carry information about the smaller spacings in the object: if they are blocked by inserting a suitable aperture in the back focal plane of the lens, an image formed by the small angle rays only is obtained. Although, this correction brings the resolution down to the point resolution limit, further treatment is necessary to improve the resolution further.

One solution to the above issue is the use of higher acceleration voltages, thereby decreasing the electron wavelength thus decreasing the point resolution limit. This approach, however, involves the use of high end expensive equipment with acceleration voltages in the range of 1200 kV which brings the resolution down to 1 Å [94]. The most efficient solution came with the use of non-round (hexapole) lenses, the principle of which was first outlined by Scherzer [95] in 1947. These multipole lenses are capable of generating a negative value of C_s and thus can cancel the positive C_s of the round lens. The net effect of eliminating C_s is that rays scattered at high angles to the optic axis are now brought to the correct focus, and the point resolution limit is extended.

In the current study, an imaging-side aberration-corrected FEI titan 80-300 , operated at 80kV, was used to obtain atomic-resolution images of the suspended chemically derived graphene membranes. The spherical aberration is set to ca. 15 μm and imaging is done at Scherzer conditions (defocus ca. -100 nm)[†] Under these conditions, atoms appear black and images can be directly interpreted in terms of the atomic structure up to a resolution of ca.

[†] The focal distance of the electron lenses is variable, depending on the excitation current. The variation of the focal distance results in another phase shift which can in certain manner compensate the phase shift due to the spherical aberration. In 1949 Scherzer suggested an optimum defocus condition which occurs at $-(C_s\lambda)^{1/2}$.

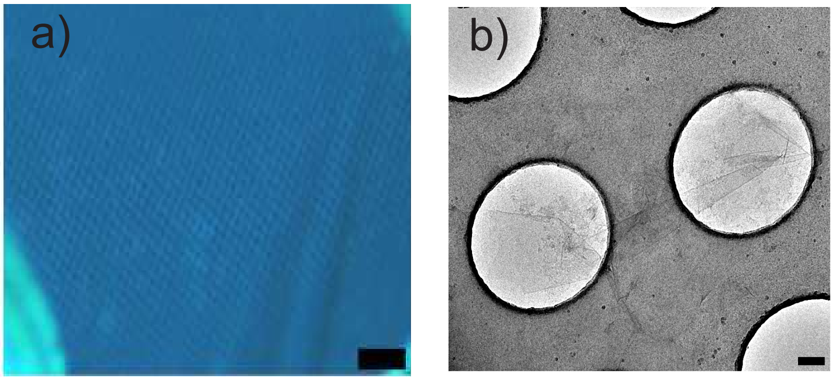

Figure 2.7: (a) Optical micrograph of graphene oxide sheets on the Quantifoil (QF) TEM grid (scale bar 10 μm). (b)TEM image of RGO sheets over holes on the QF grid (scale bar 200 nm).

~1.5 Å. The extraction voltage of the source is reduced from its standard value (3.8 kV) to 1.7 kV in order to reduce the energy spread resuulting in a clear improvement of resolution and contrast, both of which are limited by chromatic aberrations at 80 keV operation voltage. The sample stability in the 80 keV electron beam, instrumental sensitivity, and resolution is sufficient to determine the atomic configuration not only in the graphene lattice, but also in the defect configurations. The atomic configuration of most carbon atoms in these defects can be assigned, except for a small percentage of the atoms that have moved during the effective exposure time.

Sample preparation for the TEM analysis involved the suspension of graphene sheets on supports by different means. Initial studies on micromechanically exfoliated graphene involved a multistep process [96]. This process involved the identification and fabrication of graphene on Si/SiO_2 over which metal grids are lithographically patterned. The substrate is then etched away leaving graphene suspended between these metal grids. This step is significantly simpler in the present study due to the availability of GO sheets as a suspension. The GO suspension was deposited on Quantifoil(R)TEM grids with 0.6 μm holes on copper or gold grids by dipping the grids into the solution for 8-10 minutes, and subsequent chemical reduction by a hydrogen plasma as described earlier. In this manner, samples with a high yield of monolayers are obtained in an easy, cheap and fast way. In order to reduce contamination effects, samples were heated to 185 $°C$ in air for ten minutes prior to insertion to the TEM. Using the samples without prior heat treatment in the TEM resulted in an amorphous overlayer from residual contamination, thus preventing the analysis of the structures. Figure 2.7

shows an optical micrograph of a coated Quantifoil (QF) TEM grid, with graphene coverage visible as greyish patches. TEM imaging of the sample revealed that around 1% of the holes of the grid were covered with Reduced Graphene Oxide (RGO) sheets.

2.2.3 Near Edge X-Ray Absorption and Fine Structure (NEXAFS)

NEXAFS is based upon the excitation of electrons from core energy levels and the consequent emission of a photoelectron. The decay of the resulting core hole states results in the emission of Auger electron, for example, from valence molecular orbitals. Thus, the peak positions and spectral lineshape in a NEXAFS spectrum are directly related to the nature of these unoccupied electronic states. Decay of core holes may also occur via the emission of fluorescent photons, which originate from the top 200 nm of the film as opposed to Auger electrons, which arise from the top 10 nm (Figure 2.8(a)). Thus, this technique is both surface and bulk sensitive and has been used in literature to probe both carbon nanotube electronic structure as well as surface functional groups simultaneously [97].

NEXAFS spectra are usually recorded either through the fluorescent yield, in which emitted photons are monitored, or total electron yield, in which the sample is connected to ground and the neutralization current is monitored. X-rays are absorbed through excitations of core electrons to empty states above the vacuum or Fermi level. The created holes are then filled by Auger decay. The intensity of the emitted primary Auger electrons is a direct measure of the X- ray absorption process and is used in so-called Auger electron yield (AEY) measurements, which are highly surface sensitive.

An added advantage of NEXAFS spectroscopy is its polarization dependence. Linearly polarized X-rays are best suited for covalent systems like small molecules, macromolecules and polymers, which possess directional bonds. In this case the directional electric field vector of the X-rays can be used to determine the direction of chemical bonds of the atom selected by its absorption edge. This technique was first utilized for the benzene molecule, as shown in figure 2.8(b). Benzene, C_6H_6, has unoccupied orbitals of σ and π symmetry which are oriented parallel and perpendicular to the ring plane, respectively. When the electric field vector $\vec{E}$ is aligned normal to the benzene ring, peaks due to the out-of-plane π orbitals are seen and when $\vec{E}$ is parallel to the resonances due to the in-plane σ orbitals are dominant. This study revealed that benzene lies down on the Ag surface.

The detailed spectral resonances at the carbon K-edge, for instance, yield

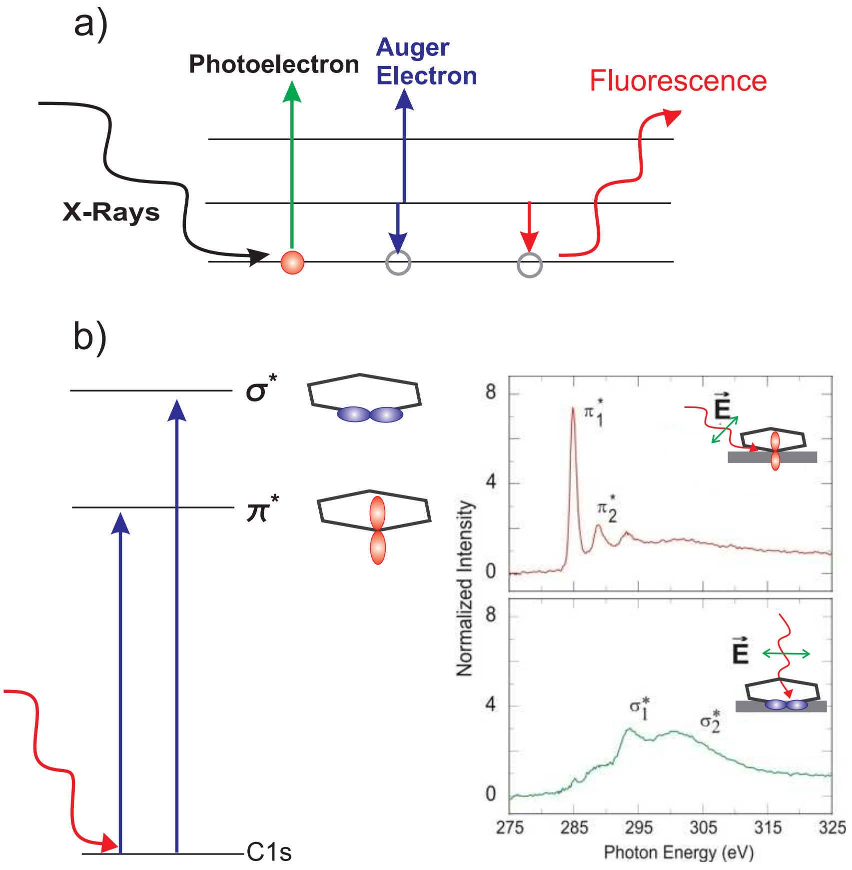

Figure 2.8: (a)The fundamental processes which contribute to NEXAFS spectra: photoabsorption of an X-ray into a core level followed by subsequent photoelectron emission, followed by either filling of the core hole by an electron in another level, accompanied by fluorescence; or filling of the core hole by an electron in another level with emission of an Auger electron.(b)Utilization of polarization dependent NEXAFS spectra of benzene chemisorbed on Ag(110), to determine molecular orientations [98].

information about the bonding environment of carbon atoms in the sample, such as the presence of functionalized species and chemisorbed impurities. In this thesis, NEXAFS at the carbon and oxygen K edge are used in order to again understanding of the chemical and electronic structure of graphene oxide sheets. Laterally resolved NEXAFS experiments were performed in collaboration with the surface/interface microscopy (SIM) beamline of the Swiss Light Source, using an Elmitec PEEM [‡] equipped with an energy analyzer. Element-specific PEEM contrast was obtained by dividing pairs of images recorded at the absorption edge and below the edge, thus reducing topographic effects and enhancing the chemical contrast. NEXAFS spectra were then acquired by processing stacks of PEEM images obtained by scanning the incident photon energy across C-K and O-K edges. The measured total electron yield (TEY) of the region of interest was then normalized to the TEY collected from an external area. Measurements were performed at grazing incidence (16°) with respect to the plane of the grid, with the linear polarization vector nearly-perpendicular ($E = \vec{E_1}$) or parallel to the grid ($E = \vec{E_2}$). The two configurations enhance transitions into final states of π or σ symmetry of graphene, respectively.

2.3 Electrical Characterization

2.3.1 Device Fabrication

Graphene oxide sheets were deposited and reduced (described in section 2.1) on degenerately doped silicon substrates with a thermally grown SiO_2 layer (300 nm thickness) modified with 3(aminopropyl)-triethoxysilane. These substrates are equipped with a marker array which aid in the physical location of the deposited sheets (figure 2.9).

All electrical measurements made in this work employed two (or four) electrodes for drain and source contacts and used a degenerately dope Si substrate as the back gate. These electrodes were defined using e-beam lithography, followed by metal evaporation and lift-off process. The steps involved in the fabrication are schematically shown in figure 2.10.

Polymethyl methacrylate (PMMA) resist was deposited on the samples via spin coating. Coordinates of electrodes defined after localization of the graphene sheets were fed into the e-beam lithography system (Raith e-Line) which then exposed the appropriate regions to an electron beam. The development of exposed samples was done using a 1:3 mixture of methyl isobutyl

---

[‡] Photo-Emission Electron microscopy (PEEM), is a widely used type of emission microscopy. PEEM utilizes local variations in electron emission to generate image contrast.

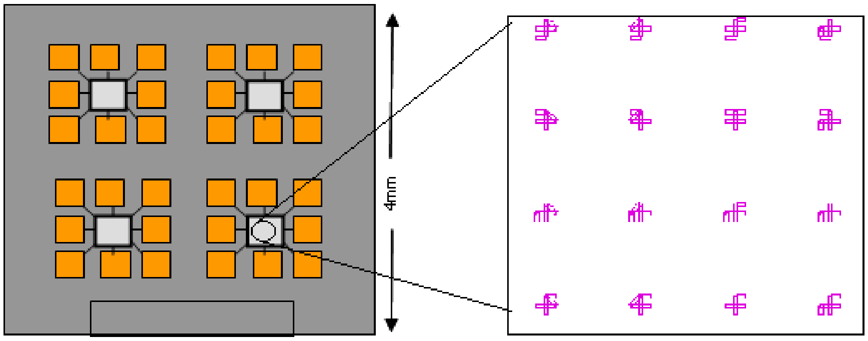

Figure 2.9: Architecture of the samples used for localizing the deposited graphene sheets.

ketone (MIBK) and iso-propanol. The samples were fabricated in a field effect transistor (FET) configuration as depicted in figure 2.10(b). The titanium/gold drain and source contacts were then evaporated under vacuum (p $\sim 10^{-6}$ $mbar$). Titanium serves as an adhesion layer to overcome the poor interface of Au on SiO_2. Finally, the lift-off was done by leaving the sample in N- Methylpyrrolidone at 55 °C for 2 hours along with subsequent rinsing with acetone and iso-propanol. The resulting device was then imaged by Atomic Force Microscopy (AFM) as shown in figure 2.10.

The fabricated FETs were characterized using the back gated configuration in most of the experiments. In certain cases, a polymer electrolyte top gate was employed in order to gain higher gating efficiencies. This gating approach has been successfully utilized on devices based on several carbon nanostructures [99–102]. In order to prepare such gates on fabricated FETs, a mixture of lithium perchlorate ($LiClO_4$)(10 mg/ml) and poly-ethylene Oxide (PEO)(20 mg/ml) was dissolved in a 4:1 mixture of methanol/water. The resulting solution was drop-casted on the samples and baked at 60 °C for half an hour, thus forming a gel on top of the substrate. A silver wire is used as the working electrode. Based upon the ionic conductivity of the medium, application of a gate voltage causes the formation of an electrochemical double layer (Debye layer) at the graphene-electrolyte interface. Variation of the gate voltage leads to charging and discharging of this layer, which shifts the Fermi level of the contacted graphene and thereby modulates its conductance. The electrochemical gating process is schematically depicted in figure

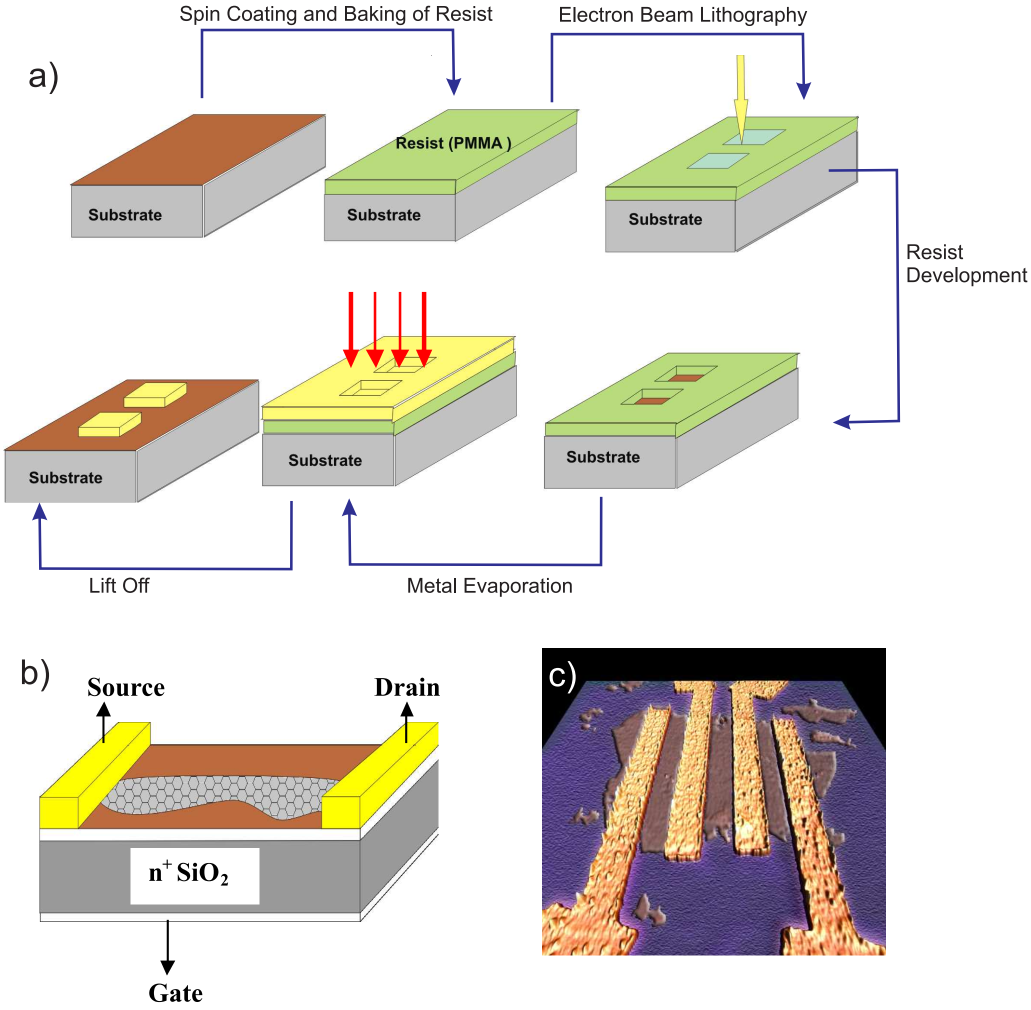

Figure 2.10: (a)A step-by-step scheme of the process employed for the deposition of contacts on the graphene sheets. (b)Devices were fabricated in a top contact bottom gated configuration. (c) AFM image of a fabricated device.

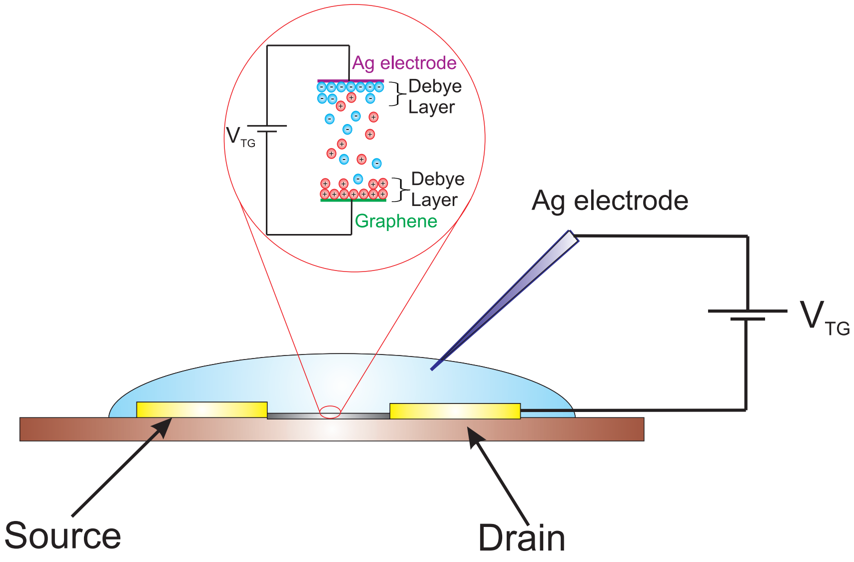

Figure 2.11: Illustration of polymer electrolyte top gating setup. The polymer gel covers the entire device, and a Ag wire is used to apply an electrochemical potential. Inset shows the gating mechanism with Li^+(red) and ClO_4^- (blue) ions and the Debye layers near each electrode.

2.11.

2.3.2 Electrical Transport

Electrical measurements were performed on a micromanipulator probe station connected to a setup comprising of the following instruments:

- A voltage source (Keithley 2400) that supplies the drain-source bias V_{ds}.
- A current-voltage converter in order to amplify the recorded current I_d which is then recorded by a Keithley 2000 multimeter.
- For gated measurements an additional Keithley 2400 source meter is employed to apply a gate-source voltage $V_{gs}$and is equipped with the capability to monitor the leakage current (I_g)through the back or top gate.

Device characterization was done depending on experimental requirements. Typically, a fabricated graphene device is tested for its $I-V$ characteristics first by acquiring I_d as a response to varying V_{ds}(usually a low bias voltage is used < 500 mV). In order to characterize the field-effect response, I-V characteristics were recorded by sweeping V_g. Linear fits of the recorded $I - V$ curves were then plotted as resistance at different gate voltages. Alternatively, in some cases I_d was directly plotted against varying V_g analogous to the transfer characteristics in conventional field-effect transistors. These measurements, however, are done in a two-probe configuration which includes resistance contribution from contacts which can in part be overcome by using a four-probe electrode geometry. In this configuration the resistance is calculated by monitoring the voltage drop across the inner two electrodes by passing a current across the outer electrodes. However, in case of carbon nanostructures, it has been shown that metal contacts possess an invasive nature. Thus, even the four-probe configuration is influenced by the contacts [103]. A detailed study of contacts on graphene devices is presented in Chapter 5.

Low temperature measurements were performed in an Oxford Instruments cryostat. Here, the sample is cooled in liquid He reservoir. The temperature of the sample is controlled using an heating element on the sample holder. The sample itself is under a low pressure of He and its temperature is recorded using a thermocouple placed close to the sample. The sample is placed in a chip carrier which is electrically connected to the sample using gold wire bonding. The chip carrier is mounted on the sample holder which is electrically wired out of the cryostat which is then connected to the acquisition setup described for ambient measurement to perform all the required experiments at temperatures between 260 K to 4.2 K.

2.3.3 Confocal Microscopy

Confocal microscopy is a technique to improve the resolution of optical images that would otherwise appear blurred when viewed with a conventional microscope. This is achieved by excluding most of the light from the specimen that is not from the microscope′s focal plane. This technique was pioneered by Marvin Minsky at Harvard University in 1955. By illuminating a single point at a time Minsky avoided most of the unwanted scattered light that obscures an image when the entire specimen is illuminated at the same time. Additionally, the light returning from the specimen passing through a second pinhole aperture rejects rays that were not directly from the focal point. The remaining ”desirable” light rays would then be collected by a photomultiplier and the image gradually reconstructed using a long-persistence screen.

A Leica TCS SP2 confocal microscope was used in the current study. Figure 2.12 illustrates the working principle of this setup. A laser is used as the primary light source which is first directed through a pin hole aperture

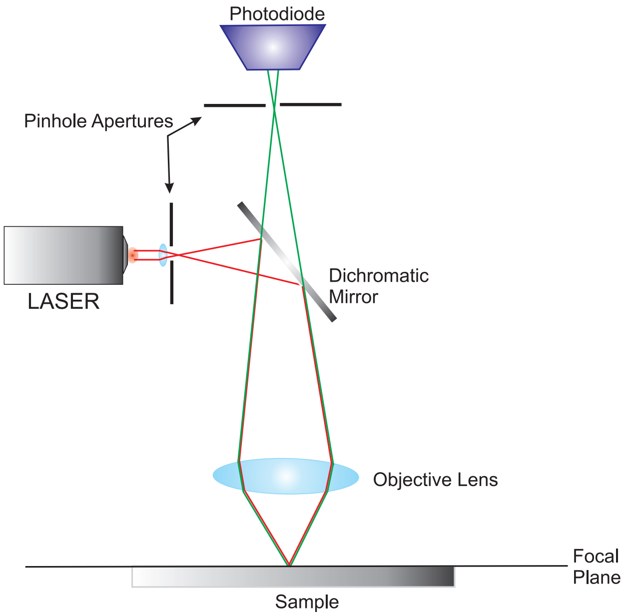

Figure 2.12: Schematic diagram of the optical pathway and principal components in a laser scanning confocal microscope.

for spatial filtering and redirected onto the objective using a dichromatic mirror. The high numerical aperture objective lens used in this work focuses the beam to a diffraction limited laser spot. The reflected light is then collected after eliminating out-of-focus light using a pin hole aperture by a photodiode which converts the optical signal to a processable electrical signal. This technique is a point by point acquisition technique. Hence in order to obtain information from the whole sample a raster scanning mechanism has to be employed. This can be achieved either by employing scanning mirrors or by moving the sample in the focal plane using a piezoelectric stage. The latter technique enables raster scans over larger areas, and was used in this thesis.

A confocal microscope as described above has been used for several microscopy and spectroscopy studies in the recent past [104–106]. For example, if the excitation wavelength can be filtered using a notch filter in the beam path of a confocal microscope, one can detect Raman shifts with the aid of a CCD detector, thus providing a high (spatial) resolution raman imaging technique. This advantage has recently been experimentally utilized in studying structural damage caused by laser irradiation on graphene layers [107]. The present thesis also deals with the utilization of confocal Raman spectroscopy to understand the nature of contacts to graphene devices (chapter

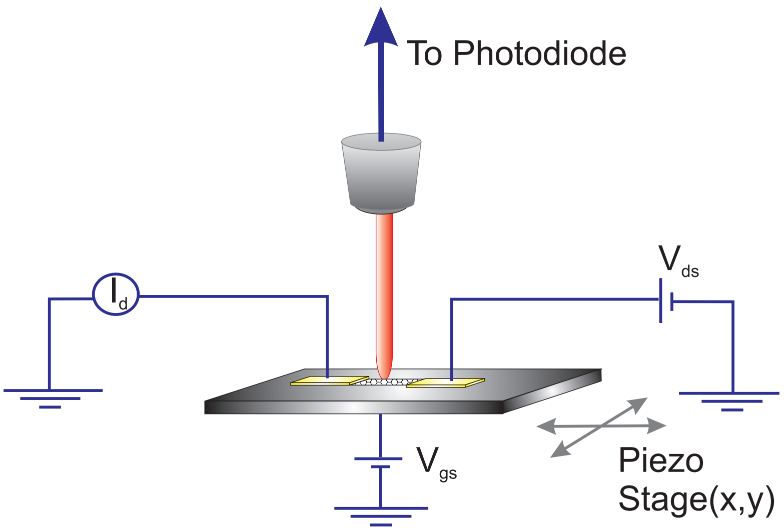

Figure 2.13: Scanning Photocurrent Microscopy: The laser spot is focussed onto the sample as a diffraction limited spot, and the sample is scanned in the focal plane. The photo-induced currents are recorded using an electrical transport setup. Spatial correlation is enabled by the simultaneous recording of the reflected light.

5). In addition, the contacts in these devices are studied by applying confocal microscopy to perform spatially-resolved photocurrent measurements. Scanning Photocurrent Microscopy (SPCM), has recently been applied to study devices with great success [103, 108–110]. This method involves the acquisition of currents generated in the device due to photoexcitation of charge carriers. Figure 2.13 depicts the setup used in the current study. The photocurrent measurements were performed by recording the drain-source current I_d as a function of spatial position by illuminating a device with a diffraction limited laser spot. In order to map the whole device, the sample is mounted on a piezo-controlled stage. The microscope was equipped with HeNe (wavelengths: 633 nm and 543 nm) and Ar (458 nm, 488 nm and 514.5 nm) laser lines. The photocurrent signal was measured after amplification through a current-voltage amplifier by a Keithley 2000 multimeter. Simultaneously, reflection images were recorded using a photodiode with the signal being amplified and recorded in the same way. Thus, by raster scanning the stage photocurrent maps were acquired simultaneously with reflection images thereby enabling spatial assignments of photocurrent signals. All photocurrent measurements in this thesis were performed under ambient conditions and at zero drain-source bias (V_{ds}). A Keithley 2400 sourcemeter was used in order probe the device at different gate voltages.

Chapter 3

Atomic and Electronic Structure of chemically derived graphene

The following chapter deals with exploring the physiochemical structure of chemically derived graphene. Graphene sheets obtained via chemical oxidation of graphite and subsequent reduction were analysed by Raman spectroscopy, Transmission Electron Microscpy (TEM), and Near Edge X-Ray absorption and Fine Structure (NEXAFS) measurements.

3.1 Raman Spectroscopy

Highly ordered graphite displays only a few discernible Raman-active bands, namely the in-phase C-C stretch vibration of the graphite lattice (G band) observed at 1600 cm^{-1} and the weak disorder band caused by the graphite edges (D band) at approximately 1355 cm^{-1}. The transformation of graphite to GO leads to the broadening of the G as well as the D band, due to disorder in the graphite lattice introduced upon oxidation. In addition, a shift of the G band towards higher frequencies was observed. This upshift can be attributed to the isolated double bonds which resonated at higher frequencies as compared to graphite [111]. The reduction of graphene oxide restores the postition of G band to almost the same position as that of graphene indicating a considerable restoration of the graphitic lattice [112].

The intensity ratio of the D and G band in figure 3.1 was used as the measure of disorder in the reduced graphene oxide lattice which arises from the presence of remnant oxygen functionalities (presence of sp^3 bonded carbons) in addition to structural defects from the synthesis process. The empirical

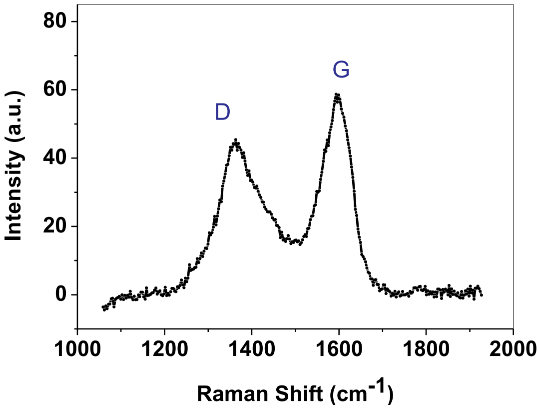

Figure 3.1: A typical Raman spectrum obtained from a reduced graphene oxide sheet ($\lambda = 633nm$). Strong D band contribution points towards a large amount of defects present due to strong synthesis and reduction processes

Tuinstra-König relation [113] relates the D/G intensity ratio to the crystallite size of graphitic samples which reported that the ratio of the D peak intensity [I(D)] to that of the G peak [I(G)] varied inversely with the average in plane crystallite size L_a:

$$\frac{I(D)}{I(G)} \propto \frac{1}{L_a} \tag{3.1}$$

Based on the above relation, it is concluded that the Reduced Graphene Oxide (RGO) sheets are comprised of ordered graphitic regions with a size of ∼6 nm surrounded by areas of oxidized carbon atoms or defects. This value is in reasonable agreement with the size of intact areas as observed in Scanning Tunneling Microscopy (STM) images reported in literature [72,112]. A direct confirmation of this analysis will be presented in the next section using Transmission Electron Microscopy measurements.

3.2 Transmission Electron Microscopy

A detailed study of the atomic structure of RGO was performed using high resolution Transmission Electron Microscopy (TEM). In contrast to mechanically exfoliated graphene, the chemically-derived graphene was found to contain a considerable amount of topological defects, which could not be detected by previous spectroscopic and microscopic investigations. Samples were prepared on carbon grids as described in section 2.2.2. Diffraction analysis was

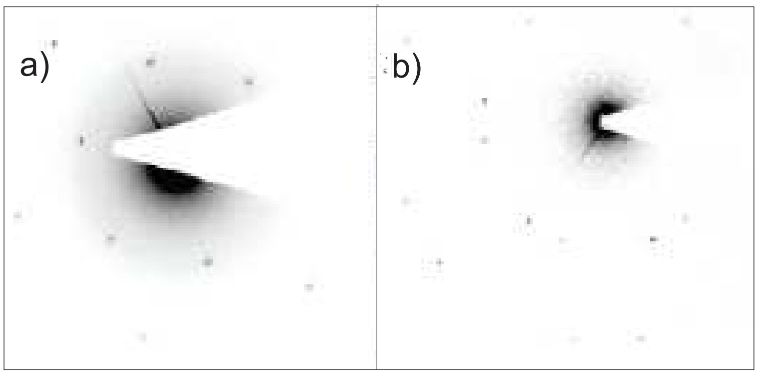

Figure 3.2: (a) Electron diffraction pattern of a single layer area. (b) Diffraction pattern from a bi-layer RGO showing the stacking with orientational mismatch of the sheets.

carried out to find holes covered by single layers. Single layers exhibited only one hexagonal pattern (figure 3.2(a)), which implies a long-range orientational hexagonal order in the sheets [96].

In contrast to mechanically exfoliated graphene, the few-layer regions always exhibited multiple hexagonal patterns (Figure 3.2(b)), implying that the multilayers are stacked in a turbostratic manner, unlike the AB Bernal stacking in graphite and mechanically exfoliated few-layer graphene [96]. This turbostratic stacking is characteristic of low interacting sheets.

Comprehensive high resolution imaging of single layers provided insight into the exact atomic structure of the RGO layers, as exemplified by Figure 3.3. Different regions of the image are marked by colors in Figure 3.3(b). It is apparent that the largest portion of the layer is comprised of clean well crystallized graphene areas where the hexagonal lattice is clearly observed (light gray color). Akin to mechanically exfoliated graphene, we also observe a significant amount of regions where carbonaceous adsorbates and also heavier atoms are trapped [114, 115] (dark gray). The average size of the visible well-crystallized areas is from 3 to 6 nm, and statistics reveal that they cover ∼60% of the surface. Another similarity to mechanically exfoliated graphene is the formation of larger holes under electron irradiation. However, in contrast to the latter, a significant amount of topological defects is observed within the clean areas. These can be further classified into isolated topological defects (pentagon-heptagon pairs, green), and extended (clustered) topological defects that appear as quasi-amorphous single layer carbon structures (marked in blue). The extended topological defects cover ca. 5% of the surface and exhibit typical sizes of 1-2 nm in diameter. Unfortunately, it is impossible to determine the RGO membrane structure below the adsorbed contamination, which constitutes ~30% of the total area. As the contaminations will preferably stick on defects, the portion of the defective regions is most likely underestimated. Surprisingly, despite the presence of such a significant amount of topological defects, the long-range orientational order is maintained. This can be discerned in the direct images, but is also clear from the diffraction patterns.

A closer investigation of clustered topological defects that are marked in blue in figure 3.3(b) and shown in figure 3.4(a),(b) revealed that they predominantly incorporate a larger number of carbon pentagons, heptagons, and rotated hexagons in a nanometer-sized area. Nevertheless, all carbon atoms in these areas are bonded to three neighbors in a planar sp^2 configuration. The absence of such defect configurations in mechanically exfoliated graphene identifies these clustered defects as a remnant of the oxidation-reduction process, which evolved from the originally strongly oxidized areas. While these clusters have not fully restored the crystalline, hexagonal graphene framework, they exhibit a planar geometry with a strong sp^2 character. Their quasi-amorphous character results in disordered single-layer inclusions dominated by pentagons, hexagons, and heptagons within the membrane. The intensity difference in the centers of these three types of polygons was used as a guide to discern the remaining disordered structure.

The observed separation of the defective and crystalline areas in RGO is in agreement with the model proposed by Lerf and co-workers [69]. This model gains further support by NMR studies [71] which suggest that the majority of the carbons with hydroxyl and epoxide groups are arranged within the highly oxidized areas which separate the undisturbed graphitic regions.

3.3 Local chemical structure probed by NEXAFS

Spatially resolved near-edge X-ray absorption fine-structure was applied to probe the chemical composition of oxidized patches present in graphene oxide. In Fig. 3.5(a), NEXAFS data recorded across the C-K edge of GO membranes are shown, using the nearly perpendicular photon polarization vector $\vec{E_1}$. The NEXAFS spectrum (thin line) of a single-layer region with an average spectrum (bold line) obtained from several regions that span the holes in the support film, was compared with a different number of layers. The inset of fig. 3.5(a) shows the C K-edge spectrum of a single-layer graphene membrane freely suspended across the hole of a Quantifoil(R) TEM grid,

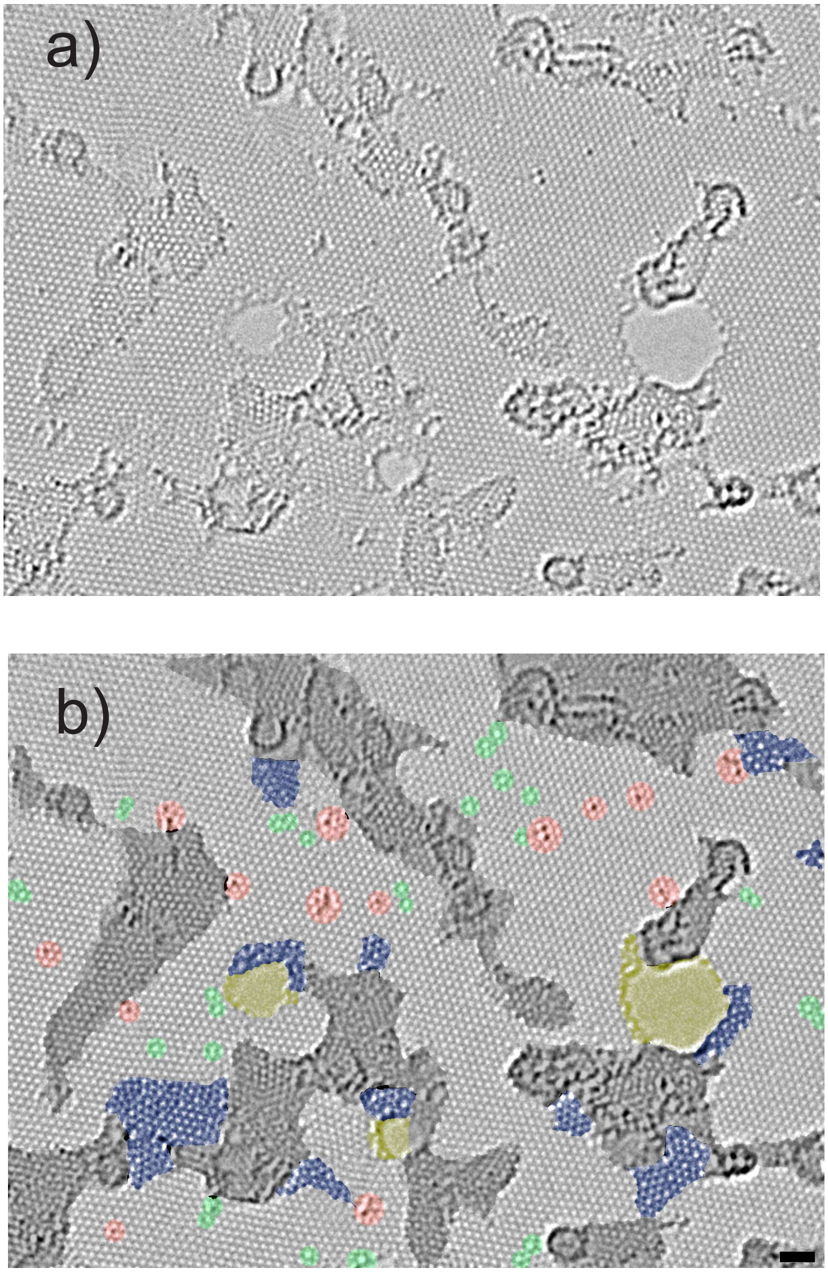

Figure 3.3: Atomic resolution, aberration-corrected TEM image of a single layer of reduced-graphene oxide. (a) Original image, and (b) with color added to highlight the different features. The defect free crystalline graphene area is displayed in the original light-gray color. Contaminated regions are shaded in dark gray. Blue regions are the disordered single-layer carbon networks, or extended topological defects. Red areas highlight individual ad-atoms or substitutions. Green areas indicate isolated topological defects, i.e. single bond rotations or dislocation cores. Holes and their edge reconstructions are colored in cyan. Scale bar is 1 nm.

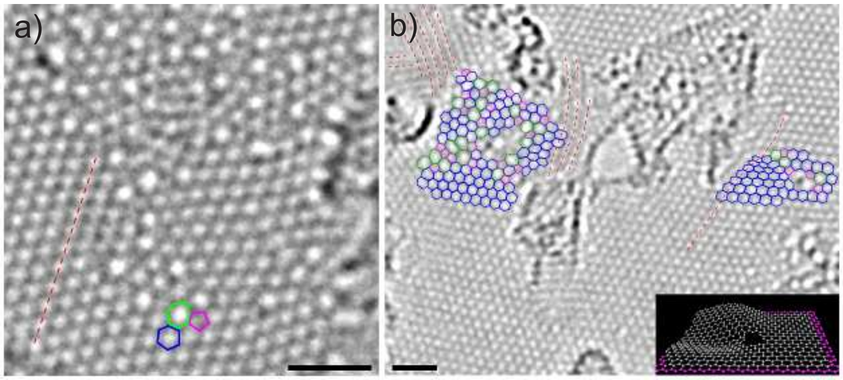

Figure 3.4: (a) Atomic resolution TEM image of a non-periodic defect configuration. (b) Partial assignment of the configurations in defective areas. Again, carbon pentagons, hexagons and heptagons are indicated in magenta, blue and green, respectively. All scale bars are 1nm.

taken by using $\vec{E} = \vec{E}_1$ (polarization ⊥ graphene lattice plane). The line shape of this spectrum is similar to that reported for single-layer graphene on SiO_2 substrates [116, 117].

Due to the polarization of the light, the C-K edge spectrum of graphene is dominated by the first resonance π^* at 285.5 eV, while, above the first σ^* resonance at 295 eV, high energy features are suppressed. This peculiarity of the NEXAFS spectrum of graphene [116] can be explained by the multiple scattering theory where scattering of the excited electron wave function by neighboring atoms is considered. Due to an open cage around the absorbing atom when the polarization of the light would select atoms above and below the graphene plane, high energy features of the C-K edge spectrum are suppressed. NEXAFS spectra of graphene and few layer graphene [116] showed that high energy features of the C-K edge spectrum are fully recovered above 5 layers. Interestingly, regardless of the number of layers, the same behavior is found here for GO membranes. In fact, above 310 eV, the spectrum of GO is almost featureless, reflecting the much higher interlayer distance (typically 0.6-0.7 nm [69, 70, 118]) of GO compared to that of graphite (0.34 nm). This finding shows that the electronic structure of GO is largely insensitive to the number of layers, as expected for a material composed of strongly decoupled layers.

Although the overall line shape of the absorption spectrum of GO (Fig. 3.5(a)) reflects the sp^2 hybridization of carbon atoms, interesting differences are found with respect to pristine graphene. First, the ratio between the

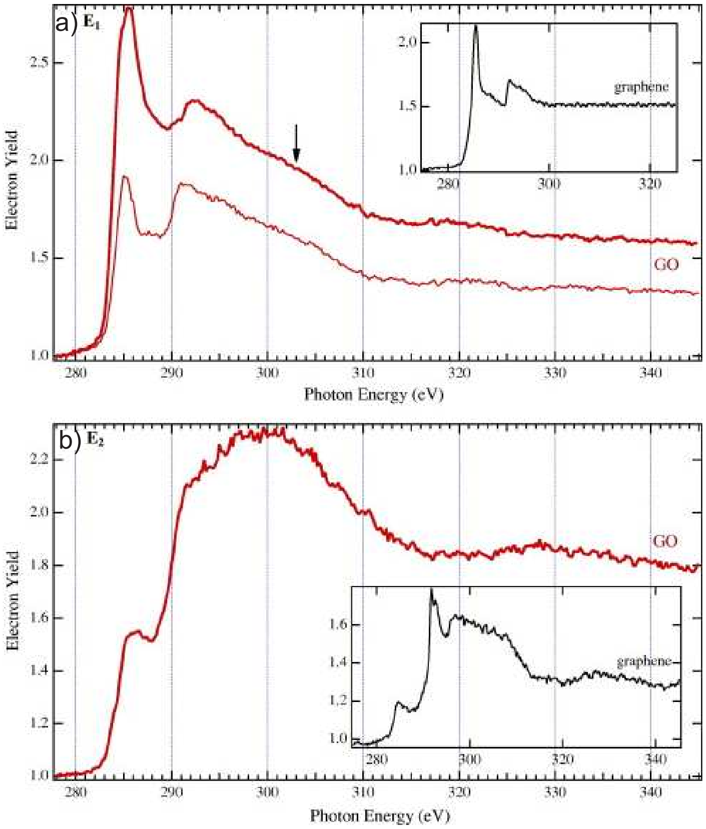

Figure 3.5: C K-edge absorption spectra of single-layer GO (thin line) and average few-layers (thick line) taken with a linear polarization vector: (a) nearly-perpendicular to the plane of the grid ($\vec{E_1}$); (b) parallel to the plane of the grid ($\vec{E_2}$). In the insets corresponding spectra, taken at $\vec{E_1}$ and $\vec{E_2}$, of a freely suspended single-layer pristine graphene membrane are displayed

π^* and first σ^* resonance (at about 292 eV) is reduced in the absorption spectrum of GO, indicating a new component of carbon atoms with sp^3 hybridization. In fig. 3.5 (b) the corresponding spectra of GO (average spectrum) and graphene (inset) are compared for the photon polarization vector $\vec{E_2}$. The spectrum of graphene exhibits a non-vanishing π^* peak, due to possible misalignments of the suspended flake with respect to the support grid, and a strong onset of the σ^* transition at 291.8 eV, with clear excitonic character [119]. Going from pristine graphene to GO (Fig. 3.5 (b)) the excitonic peak disappears, reflecting the existence of defects and lower order in GO. The broadening of the π^* resonance reflects a lowering of the local order in GO [116].

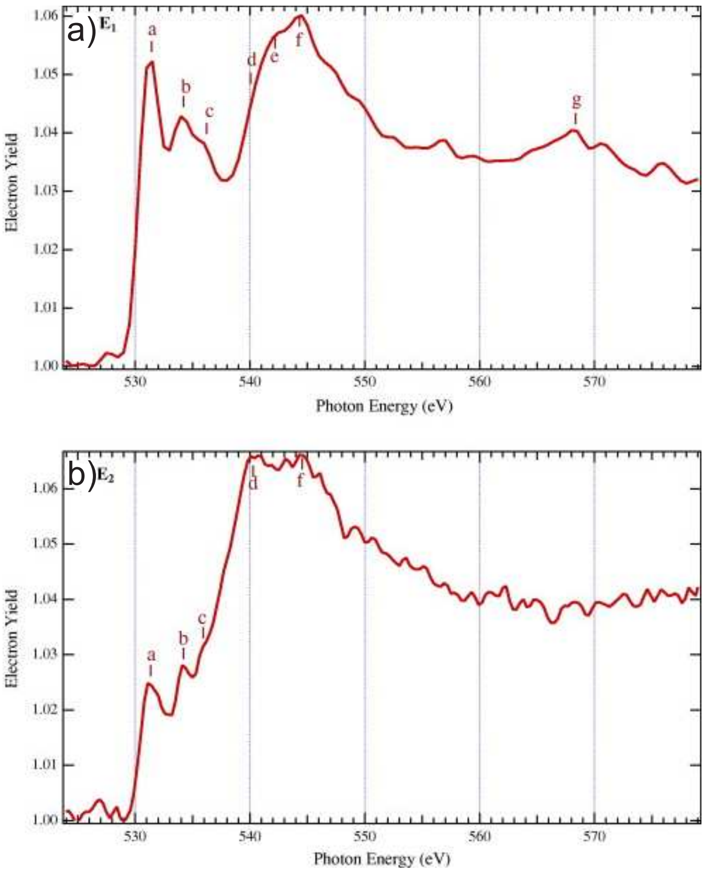

Figure 3.6: O K-edge absorption spectra of average few-layers GO taken with a linear polarization vector: (a) nearly-perpendicular to the plane of the grid ($\vec{E_1}$); (b) parallel to the plane of the grid ($\vec{E_2}$).

The origin of the sp^3 component is revealed by the O-K edge spectra (fig. 3.6), recorded with $\vec{E} = \vec{E_1}$ (a) and $\vec{E} = \vec{E_2}$ (b) corresponding to polarization perpendicular and parallel to the graphene lattice plane respectively. Peak a at 531.5 eV is assigned to the π^* state of $C = O$, which may belong to carbonyl groups bonded to an aromatic ring [120], or to $-COOH$ groups attached at the graphene oxide edge sites [121]. Peaks e and f, at 542.0 eV and 544.5 eV, respectively, are σ^* resonances again associated with carbonyl groups [120]. These peaks indicate that $C = O$ species directly bonded to aromatic rings of graphene do exist in the basal plane of GO, as previously argued by the line shape analysis of the C1s photoemission peak of GO [70]. Peak b at about 534 eV can be related to the π^* state of CO bond of the epoxide [122], while peak c at 535.5 eV is a fingerprint of $-OH$ groups [120].

Going from a photon polarization vector almost perpendicular to the grid ($\vec{E_1}$) to the parallel case ($\vec{E_2}$), (Fig. 3.6(b)) the broad peak centered at about 542 eV dominates the spectrum. In this configuration, the *d* peak at about 540 eV, assigned to CO σ^* states derived from basal phenolic groups [120], become more intense, while the *g* peak at about 568 eV (fig. 3.6(a)) disappears. This high energy feature can be related, in a multiple scattering theory approach, to the interference occurring between the forward-propagating emitted wave and the wave backscattered from the surrounding shells of atoms. The fine structure of the oxygen edge spectra reported in Fig. 3.6 exhibits remarkably sharp, distinct features, affected by the polarization of the light, suggesting a locally ordered arrangement of oxygen atoms [123].The intensity decrease of peak *a* going from $\vec{E_1}$ to $\vec{E_2}$ in fig. 3.6 (a) and (b)indicates that on the average carbonyl species are oriented along the graphene plane, in agreement with both the ScholzBoehm [67] and Dékány model [70].

3.4 Conclusions

The complex structure of graphene derived chemically from graphene oxide has been studied in this chapter. The strong D band contribution indicates a high degree of disorder in the lattice. The ratio of Raman D/G peak reveals the sizes of the crystalline lattice to be of the order of 6 nm surrounded by defects. TEM investigation of these layers has confirmed this model by real space atomic resolution imaging. NEXAFS measurements employed to investigate the local chemical structure of this material have demonstrated a dominant sp^2 hybridization of carbon atoms in the C K-edge spectra and show that the coupling between layers is strongly reduced with respect to the one of graphite.O K-edge spectra clarify the chemical composition of oxidized patches, showing carbonyl groups, together with epoxide and hydroxyl groups, attached to aromatic rings, and carboxyl groups likely attached to the edges of the membranes. Thus, the complex structure of graphene oxide and reduced graphene oxide emerges as a combination of the model suggested by Lerf et al. [69] with respect to its lattice structure and that by Scholz-Boehm [67] with respect to its chemical functionalities.

Chapter 4

Charge Carrier Transport

Graphene oxide is an insulator. In order to obtain electrically viable graphene from graphene oxide a chemical reduction step is required as described in section 2.1.4. This step can restore the graphene lattice structure in these sheets, although a considerable number of structural defects are concomitantly created in the process. Accordingly, graphene obtained via this method consists of a structure where graphene islands separated by defect clusters. This deviation from the flawless structure of pristine graphene has strong implications on the nature of electrical transport in this material. This chapter reports an in-depth investigation of the electrical properties of these sheets in order to classify the electrical conduction mechanism.

4.1 Room Temperature Measurements

Reduced graphene oxide sheets were characterized by two-probe transport measurements by contacting the lithographically defined electrodes using a tungsten needle probe or bonded Au wires. Figure 4.1 shows the $I - V$ characteristics of both graphene oxide (GO) and reduced graphene oxide (RGO). The electrical conductivity of the reduced GO monolayers increased by around 3 orders of magnitude upon reduction by 5 seconds of hydrogen plasma treatment. Room temperature measurements yielded conductivity values in the range of 0.1-3 Scm^{-1} in accordance with literature reports. [72]. This range is about 3 orders of magnitude below the values reported for pristine graphene [2].

The measured resistance in a two probe configuration can be represented as a combination of contributions from the graphene sheet and the contacts. In case of mechanically exfoliated graphene, this presents a significant issue because the metal contacts possess an invasive nature [103] and 100 % ac-

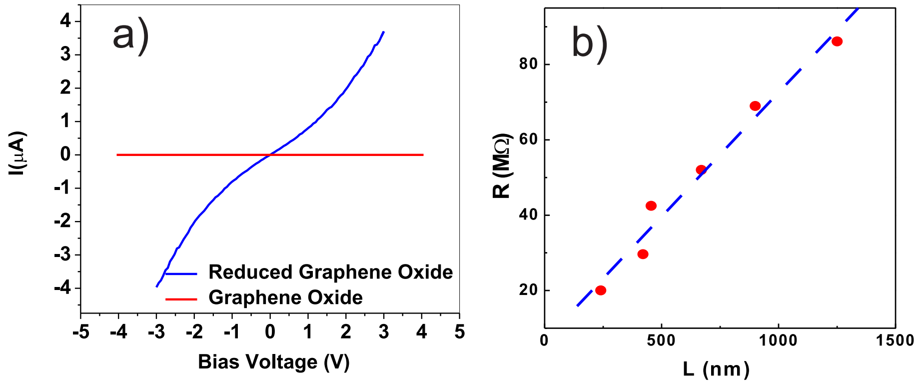

Figure 4.1: (a) $I-V$ characteristics of graphene oxide (red) and reduced graphene oxide (green) sheets at room temperature. 5 seconds of H_2 plasma converts insulating GO to its conductive reduced form. (b) Room-temperature resistance (measured at a voltage of (100 mV) increasing linearly with channel length, evidencing that it comprises primarily of the intrinsic resistance of the GO sheet with an insignificant contribution due to contact resistance

curate measurements cannot be made even using a four-probe configuration. The situation is different in case of RGO devices. Here, contact contribution is minimal, and hence the major voltage drop occurs along the channel. Figure 4.1 (b) shows the two-probe resistance measurements measured at 100 mV drain-source bias from devices with varying channel lengths. The linearly increasing resistance with the abscissa passing through origin confirms that the resistance measured purely originates from the RGO channel.

The contacted RGO sheets showed ambipolar behavior (figure 4.2) similar to that of mechanically exfoliated graphene [2]. The resistance of the bare graphene displays a maximum at a gate voltage of approximately +30 V, a finding attributable to p-type doping upon contact with the ambient, which causes a shift of the charge neutrality-point toward positive gate voltages. This shift is significantly restored by measuring in vacuum. Similar shifts have been reported for mechanically exfoliated graphene and single-walled carbon nanotubes, which are explained by doping due to oxygen and/or water absorption [124]. Carrier mobilities were estimated by applying the Drude model $\mu = (ne\rho)^{-1}$ which resulted in values of up to 1 $cm^2V^{-1}s^{-1}$.

The adsorption of water molecules at the defect sites and dangling bonds on carbon nanotubes has been well documented [125]. Water also acts as an

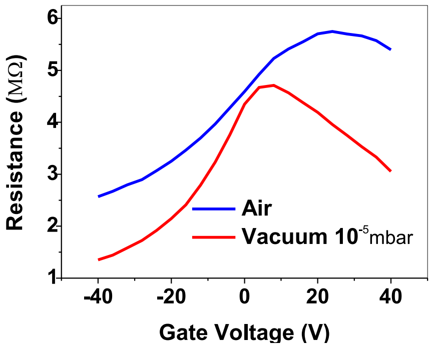

Figure 4.2: Room temperature gate dependence of resistance of a RGO sheet measured in air and under vacuum.

electron acceptor when adsorbed on the graphene surface as verified by recent experimental [16] and theoretical investigations [124]. It has been reported that the adsorption of water on the surface of graphene is accompanied by hole injection. A p-type doping is thus expected when the electron affinity of the adsorbate molecule (water) is greater than the work function of the substrate (graphene). This is possible only if the adsorbate possesses unoccupied electronic states lower in energy than the highest occupied state of the substrate. Theoretical calculations show that this condition is satisfied in the case of this system [124].

4.2 Low Temperature Measurements

Low temperature electrical measurements were performed from room temperature down to 2 K as a function of source-drain bias and gate voltage to investigate the nature of conduction in RGO devices. In Figure 4.3 (a) and (b), the current I measured between 2 K and 200 K through a reduced GO sheet at different gate voltages V_g from -20 to +20 V is compared at high and low values of bias voltage V_{ds}. In each case, the current is smallest for zero gate voltage, at which the charge neutrality point was observed (Figure 4.3(c)). All plots exhibit an asymmetry between the effect of positive and negative gate voltages, with negative V_g values producing a greater increase in conductance than corresponding positive values. A common feature of the plots is that at higher temperatures the natural logarithm of the current shows a linear dependence on $T^{-1/3}$, which is indicative of two-dimensional (2D) Variable Range Hopping (VRH) conduction [126]. This

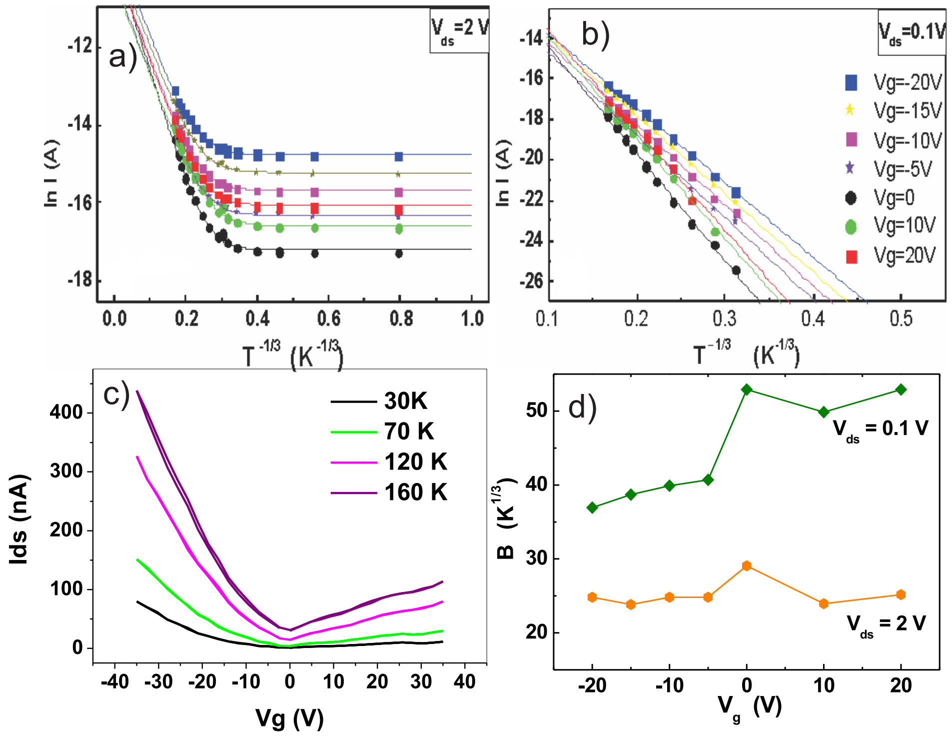

Figure 4.3: Natural logarithm of the measured current I vs 1/T$^{1/3}$ (points) and their fits (lines) according to equation 4.1 representing 2D variable-range hopping in parallel with a temperature-independent term, for different values of the gate voltage V_g as indicated, for bias voltages (a) V_{ds}= 2 V, (b) V_{ds}= 0.1 V. (c)Low-bias transfer characteristics of a fully reduced GO monolayer measured as a function of back gate voltage at different temperatures (V_{ds}= 0.1 V). (d) Hopping parameter B for the fits in (a) and (b), plotted as a function of gate voltage V_g for different values of bias voltage V_{ds}.

behaviour is in stark contrast to the phonon limited mechanism present in pristine graphene [127].

For low bias voltages V_{ds}= 0.1 V), all the measured data follow the 2D VRH law (from 216 K down to 34 K). For the largest bias voltage (V_{ds}= 2 V), at all values of gate voltage there is a deviation from the 2D VRH behavior below ~100 K, with essentially temperature-independent behavior below 25 K down to the limit of measurements at 2 K. It is also interesting to note that this flattening occurs faster at negative gate voltages. The overall temperature dependent conductance ($G(T) = I/V_{ds}$) in Figure 4.3 is in excellent agreement with the expression

$$G(T) = G_1 \exp\left(-\frac{B}{T^{1/3}}\right) + G_0 \tag{4.1}$$

where the first term represents the usual 2D VRH conduction expression and the second term represents purely field-driven conduction without thermal activation. The hopping parameter B depends on the density of states $N(E_F)$ near the Fermi level and the localization length L_l of the electronic wave functions involved; for 2D VRH its value is given by [126]

$$B = \left(\frac{3}{k_B N(E_F) L_l^2}\right)^{1/3} \tag{4.2}$$

where k_B is Boltzmanns constant. The fitted values of this hopping parameter B are plotted in figure 4.3(d) as a function of V_g for high and low bias voltages. It can be seen that in each case, the value of B shows a peak when the gate voltage V_g is zero, reflecting the expected minimum in the graphene density of states. At small bias voltages, there is an obvious asymmetry in the effect of applying the gate voltage. The application of a negative gate voltage significantly decreases the value of B, as would be expected for an increase in the hole density of states as the gate voltage shifts the Fermi level away from the charge neutrality point. However, the values of B for positive gate voltages are considerably larger than those for the corresponding negative gate voltages, indicating (according to equation 4.1) shorter localization lengths L_l and/or fewer electron carriers.

The origin of electron-hole conduction asymmetry in graphene has been atrributed to pinning of charge density below metal electrodes [128] or imbalanced carrier injection from graphene electrodes due to dopants [129]. However, the total resistance of the reduced GO sheet is dominated by the channel rather than by electrode effects. Thus, asymmetric scattering by charged impurities [130, 131] appears to be a more plausible mechanism. Greater scattering could reduce the mobility of electron carriers and decrease their localization lengths L_l relative to hole carriers.

The dependence of the conductance $G(T, E)$ on the bias electric field strength E (for small fields) is calculated [126] by including a second multiplicative exponential term so that equation 4.1 becomes

$$G(T) = G_1 \exp\left(-\frac{B}{T^{1/3}}\right) \exp\left(-\frac{0.18er(T)}{kT}E\right) + G_0 \tag{4.3}$$

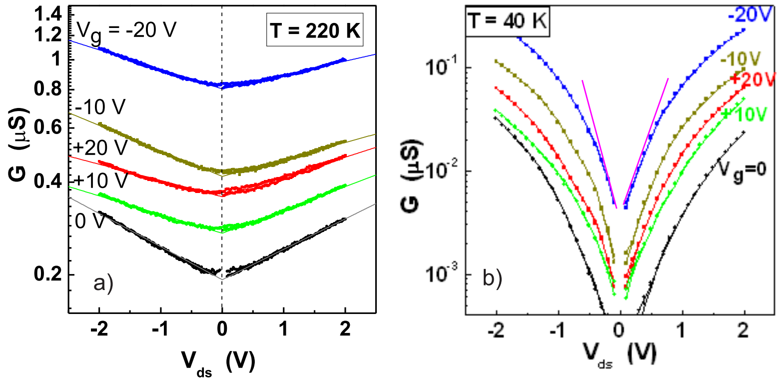

Figure 4.4: Conductance, G of a a reduced graphene oxide monolayer sample, plotted on a base 10 logarithmic scale as a function of bias voltage V_{ds} for different gate voltages V_g, at a temperature of (a) 220 K, (b) 40 K. The lines are fits to equation 4.3 for 2D VRH.

where e is electronic charge and $r(T)$ is the mean low-field hopping distance that increases as temperature is lowered. On the basis of this equation, the conductance at fixed temperature is expected to initially increase exponentially with the strength of the applied field E or bias voltage V_{ds}, starting from its value $G(T, 0)$ in the zero-field limit. Such an exponential increase with field E is demonstrated by figure 4.4(b) where the conductance G at 220 K is plotted on a logarithmic scale versus bias voltage V_{ds}. The slope of the fitted lines in figure 4.4(a) (averaged over positive and negative values of V_{ds}) is 0.238 V^{-1} for V_g=0,decreasing to 0.135 V^{-1} for V_g =+20 V, and 0.125 V^{-1} for V_g=-20 V (similar for positive and negative values of V_g , i.e., for electrons and holes). This trend of decreasing bias field effect with increasing gate voltage is as expected from equation 4.3, since the hopping distance $r(T)$ decreases at larger shifts in Fermi level away from the neutrality point, thus further reinforcing the validity of the VRH model to describe the charge transport in the reduced GO sheets.

Quantitative estimation of the hopping distances $r(T)$ reveals that VRH occurs only in part of the sample. If the bias electric field E producing the hopping were uniform across the sample, the hopping distances calculated from the experimental values of the slopes in figure 4.4 would be $r(220K)$= 63 nm for V_g= 0 and 33 nm for V_g=-20 V. These values are considerably larger than the size of 6 nm for the ordered graphene islands inferred from Raman and TEM investigation (Chapter 3). This implies that electric field is non-uniform across the length of the sample. It is hence concluded that the actual fields in the hopping regions are an order of magnitude larger than the average field strength, leading to much shorter hopping distances. This suggests the presence of relatively high conductance within the intact graphene islands that retain the hexagonal structure, with thin barrier regions representing a small fraction of the path across which most of the voltage drop occurs. We note that conduction will be dominated by paths with the thinnest barriers, and even a narrow highly conducting path between ordered lattice area would short out hopping barrier regions and greatly reduce the fraction of path where conduction is by hopping.

At the lower temperature of 40 K, the corresponding plots of conductance G versus bias voltage V_{ds} in figure 4.4(b) show a much stronger dependence on the electric field, as expected from equation 4.3 for 2D VRH upon decreasing temperature. The slope of the straight lines drawn in figure 4.4(b) showing a typical data trend at low bias voltage V_{ds} is much larger than the average slope at 220 K (figure 4.4 (a)), as expected from the exponent in equation 4.3 at lower temperatures. However, it is apparent that the increase of log_{10}G with V_{ds} is no longer linear so at this lower temperature the field E used is too strong for equation 4.3 to be valid. As the field becomes large, calculations predict a trend to saturation of log_{10}G with V_{ds}, as has been documented for germanium films at lower temperatures [126].

The lack of temperature dependence below 10 K as seen in figure 4.3(a) shows that purely field-driven conduction mechanisms start setting in as V_{ds} increases, namely, direct tunneling (that requires no thermal excitation) through disordered barriers between delocalized electron states in the graphene islands (where these barriers are thin), and field driven hopping through thicker barriers. The fact that at V_{ds} >2 V there is significant increase in the field-driven conduction at 2 K (figure 4.3(a)) indicates that this bias voltage yields a potential drop across disordered barrier regions in the heterogeneous structure of the sheets that is a significant fraction of the typical barrier energy. The spacing of the barriers must be larger than the size of the intact graphene islands (∼6 nm), and could be considerably larger if some barriers are short-circuited by highly conducting paths. Taking the separation of barrier centers ∼20 nm, and assuming the voltage drop across the highly conducting intact graphene islands to be small, the typical voltage drop across the barriers would be of order of 13-36 mV for a voltage of 2 V applied between the electrodes. Thus, the minimum tunneling barrier heights involved are on the order of 40 meV. The thermal energy k_BT at a temperature of 10 K is only ∼0.9 meV, confirming that thermally assisted conduction across such barriers would be very small below 10 K.

4.3 Conclusions

Graphene obtained via chemical reduction of graphene oxide exhibits ambipolar transfer characteristics similar to pristine exfoliated graphene. However, due to its inherent disorder as demonstrated in chapter 3, the mechanism electrical transport in reduced graphene oxide is significantly different. RGO sheets exhibit only moderate room-temperature conductivities of upto 5 Scm^{-1} and carrier mobilities of up to 1 $cm^2V^{-1}s^{-1}$, predominantly as a consequence of disorder that cannot be healed during the reduction process. These defects form barriers to electronic transport which takes place through a composite mechanism of 2D Variable Range Hopping (VRH) and field driven tunneling. At higher temperatures, both the temperature- and electric field-dependence of conductance follow the behavior predicted for 2D VRH. The derived values of the mean hopping distance point toward the presence of regions of delocalized states and relatively high conductance that are separated by disordered regions with localized states where the conduction is by hopping, a heterogeneous scenario that is consistent with Raman and TEM data. The temperature-independent conductance remaining at low temperatures can be ascribed to tunneling between regions with delocalized states and field-driven hopping in the barriers. Thus, reduced graphene oxide exhibits sufficient technological potential based on its electrical properties. However, an improvement in its conductivity and mobility could prove very useful for more demanding applications. A novel approach for this purpose will be described in chapter 5. An interesting feature of RGO devices is that the resistance measured stems almost entirely from the sheet which is of relevance for the next chapter.

Chapter 5

Device Aspects

This chapter deals with device-related studies which are important for the foreseen application of chemically derived graphene. Two issues related to understanding the nature of contacts and quality enhancement of this material shall be described in the following two sections :

- Investigation of contacts to graphene based field effect transistors (FET). A study of the nature of contacts to high quality graphene shall be presented followed by experiments to investigate metal contacts to reduced graphene oxide devices.
- Improvement of the quality of reduced graphene oxide by chemical vapour deposition treatment. The electrical and structural characterization of graphene obtained by this novel approach will be described in the second part of this chapter.

5.1 Role of contacts in graphene FETs

The performance of nanoelectronic devices based on carbon nanostructures is strongly governed by the properties of the implemented electrical contacts [132]. In the early stages of carbon nanotube research, the poor quality of the metal contacts impeded the exploration of intriguing phenomena such as ballistic conduction or spin injection. Later on, metals like palladium were found to provide close-to-ideal contacts, which enabled the realization of ballistic field-effect transistors from individual single-wall carbon nanotubes [133]. Moreover, the availability of suitable ferromagnetic metal contacts led to the development of spinvalves incorporating carbon nanotubes [134]. Thus, a clear understanding of the role played by contacts in graphene-based devices is important for its application in several areas. In the following, this task is approached using Scanning Photocurrent Micrscopy (SPCM) and Raman Spectroscopy.

5.1.1 Nature of the graphene-metal interface

The large variety of novel electronic phenomena exhibited by graphene based make it a promising contender for future high performance applications. For this purpose, properties of metal-graphene interfaces have gained considerable attention recently [103, 128, 135]. These interfaces crucially affect the performance of graphene-based electronic devices, for example in high frequency applications [136]. In order to better understand the role of contacts, a detailed study of the metal-graphene interface in field effect transistors has been using SPCM complemented by Raman spectroscopy measurements.

High quality graphene sheets were prepared by CVD on Cu foils similar to the process used in ref [50, 51]. This approach provides the advantage of easy processibility and properties close to that of pristine graphene [49]. The Cu foil samples were loaded into a quartz furnace tube and evacuated to 60 mTorr. In order to remove native CuO, the foils were then heated in forming gas at 800 °C for 30 minutes. This procedure also aided in the increase of Cu grain size. The graphene deposition was done by exposing the Cu foils to ethylene (6 sccm, 500 mTorr) at 875°C for 30 minutes.

In order to transfer the grown graphene onto another substrate, polymethyl methacrylate (PMMA) was spin-coated on top of the graphene layer on one side of the Cu foil. The Cu foil was then dissolved in 1 M aqueous $FeCl_3$ which leaves the PMMA layer floating on the liquid surface. The PMMA + graphene is then cleaned by transfer to a dilute HCl bath followed by de-ionized (DI) water bath. Subsequently, the floating PMMA +graphene layer is picked up on glass or ITO/Al_2O_3 substrates. The PMMA is then dissolved in hot acetone. In order to clean the graphene sheet further, the substrates along with transferred graphene were annealed at 200 °C for 2 to 3 hours under forming gas.(See figure 5.1(a-c)).

Devices were fabricated in a two probe-top contact configuration as shown in the AFM image in figure 5.1 (d). The graphene sheet was initially patterned using e-beam lithography and oxygen plasma etching [†] to create sheets with channel lengths of 1 or 2 μm and widths of 2 μm. This was followed by defining contacts to these sheets using a second lithography step and e-beam evaporation of 20 nm of gold. (The choice of this thickness was based on optimization for both good electrical contact and Raman signal). A third

---

[†] Oxygen plasma at 50 W power for 30 seconds was used to pattern the graphene sheet by etching the area uncovered by PMMA, thus forming uniform sheets of width 2 μm.

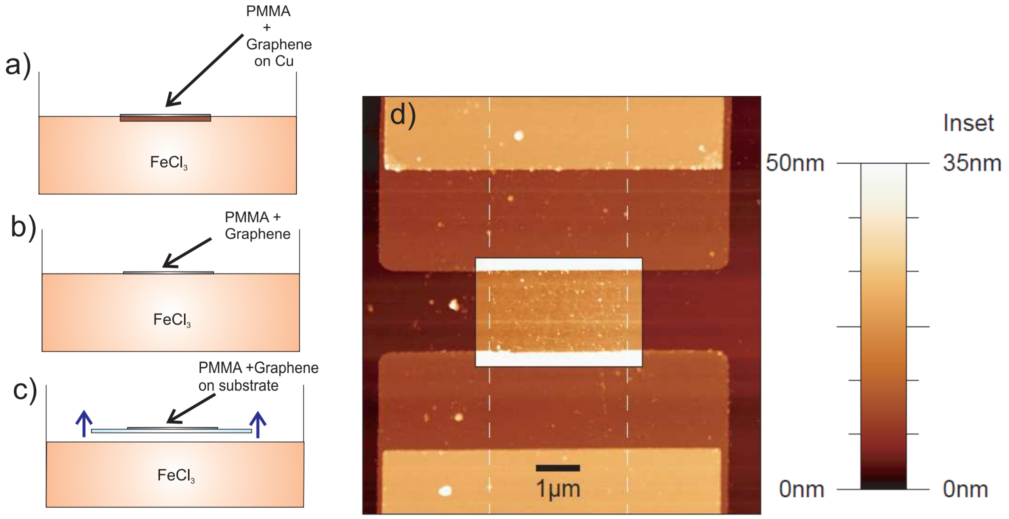

Figure 5.1: Process of transfer of graphene grown on Cu foils on to substrates. (a) PMMA coated foil is placed in an $FeCl_3$ bath to etch away the Cu. (b) Graphene adheres on to the left over PMMA and floats on top of the surface of the liquid etchant; subsequently this composite is scooped up on the desired substrate, and (c) the PMMA is dissolved using warm acetone. (d) AFM image of a device fabricated using transferred CVD graphene. The inset shows the presence of a number of domains which is typical of graphene grown by this technique. The dashed lines indicate the location of the etched graphene sheet under the contacts.

lithography step was then used to define thicker (0.5 nm Ti and 50 nm Au) and wider (100 x 100 μm) pads (in electrical contact with the 20 nm electrodes evaporated in the second step) to enable device connection using a micromanipulator stage and probe needles.

The fabricated samples were characterized in a field-effect transistor configuration. Using a polymer electrolyte gate instead of the more traditional back gate configuration (details of preparation of PEO-$LiClO_4$ gate in chapter 2). Figure 5.2 shows transfer characteristics of a 2 μm channel device, which exhibits a clear ambipolar field effect. In order to determine the carrier mobility, intrinsic carrier concentration and contact resistance, equation (5.1) to analyze the two-point resistive behavior of patterned graphene transistors [137].

$$R = R_C + \frac{L}{We\mu_{FE}\sqrt{n_0^2 + n^2}} \tag{5.1}$$

where R is the measured resistance, n is the modulated carrier concentra-

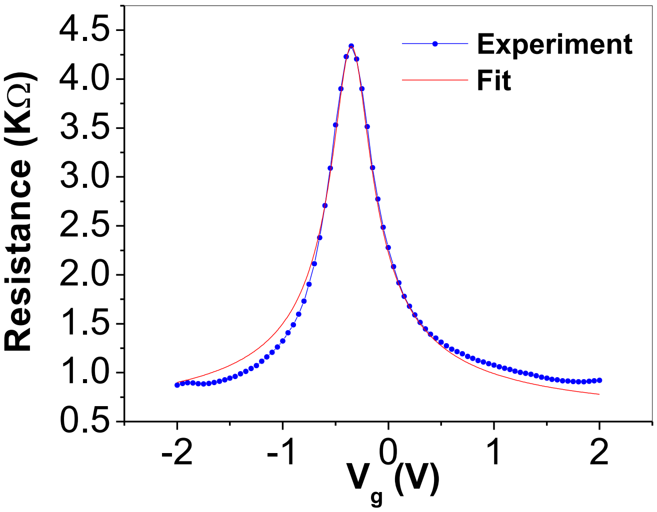

Figure 5.2: Room temperature transfer characteristics of a 2 μm channel graphene-device measured using PEO-$LiClO_4$ top gate. A fit according to equation 5.1 allowed the extraction of device performance parameters.

tion, e is the electronic charge, and L and W are the length and width of the graphene channel, respectively. This allows for determination of the intrinsic field-effect mobility (μ_{FE}), contact resistance (R_C), and intrinsic carrier concentration (n_0). The fit shown in figure 5.2 resulted in a mobility value of 1400 $cm^2V^{-1}s^{-1}$, contact resistance of 0.8 kΩ and n_0= 1.5 × 10^{12} cm^{-2}.

Scanning photocurrent microscopy measurements were carried out to study the effects of electrical contacts on fabricated devices. The setup used for this purpose was similar to the one detailed in section 2.3.3 albeit with certain changes. Here, the laser beam (λ=633 nm) was passed through the transparent substrate, thereby providing access to the graphene-metal interface covered by the metal contacts. This approach enables the study of the photo-electronic processes occuring in this previously inaccessible region. figure 5.3 schematically shows the setup comprising of a customized inverted optical microscope equipped with a closed-loop, 3-axes piezoelectric scanning stage (PI) to raster scan the graphene devices. The optical setup is also equipped with 100x, oil-immersion microscope objective having a numerical aperture of 1.25 (Zeiss) that enables small optical excitation volumes and high collection efficiencies. In this manner, the resolution of a microscope

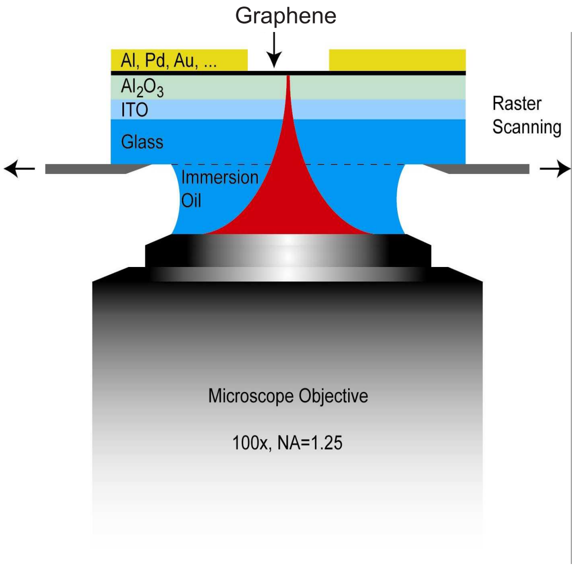

Figure 5.3: Schematic representation of the modified setup used for the scanning photocurrent microscopy and Raman spectroscopy study of the graphene-metal interface

can be increased below the diffraction limit[‡]. Spatial resolutions below 350 nm in photocurrent microscopy (illuminaton) mode and below 300 nm in reflection (confocal) mode could be achieved, respectively. Signal collection efficiencies are increased by one order of magnitude as compared to the air objective case (NA = 0.8). Thus, oil immersion microscopy plays a crucial role in highly sensitive studies like Raman spectroscopy.

Figure 5.4(a) shows a SPCM image of a graphene device taken at zero bias and zero gate voltage. Several photocurrent signals can be observed along the graphene channel. These can be attributed to charge carrier separation aided by local built-in electric fields due to the presence of electron-hole puddles in graphene [103, 138]. In addition to these finer features, strong photocurrent responses are observed around the region of the metal contacts.

[‡] The resolution of a microscope is defined as the minimum separation needed between two objects under examination in order to discern them as separate objects. If two objects are separated by a distance shorter than δ, they will appear as a single object in the microscope. A measure of the resolving power of a lens is given by its numerical aperture, NA:

$\delta = \frac{\lambda}{NA}$

where λ is the wavelength of light. To achieve a good resolution (small δ) a high numerical aperture is required. The numerical aperture of a lens is defined as $NA = n \sin\theta$, where θ is the angle spanned by the objective lens seen from the sample, and n is the refractive index of the medium between the lens and specimen.

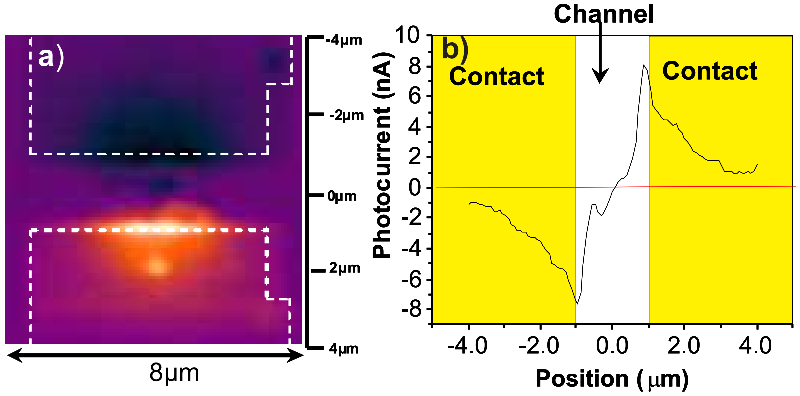

Figure 5.4: (a) A scanning photocurrent micrscopy image (dotted lines indicate the position of the metal contacts as derived from a simultaneously recorded reflection image) of the device shown in figure 5.2 at $V_d = V_g = 0V$. (b) Photocurrent section profile along the vertical axis in panel (a).

This observation is in accordance with previous SPCM studies [103, 139] where the strong photocurrent signal has been attributed to the separation of photo-excited charge carriers due to the strong electrostatic potential step at the contacts.

In order to explain these features further, it is worthwhile to consider the origin of the potential barrier at the contacts. The adsorption of gold on graphene is primarily mediated by an attractive interaction between the d-orbitals of gold atoms and the π-orbitals of the sp^2-hybridized carbon. Calculations based on density functional theory predict a weak chemical bonding of 0.03 eV per carbon atom. According to theory, the charge carrier redistribution at the graphene-gold interface caused by the chemical interaction is almost completely compensated by the charge transfer due to the chemical potential (work function) difference between gold and graphene [135]. This results in the formation of an interfacial dipole manifested in the form of a potential step (figure 5.5(a)), as has been experimentally confirmed by studying the effects of Ti and Au contacts in pristine graphene devices. In these experiments, it was found that the magnitude of this step is dependant on the difference in work function of graphene ($\Phi_{graphene}$) and the metal in contact ($\Phi_{contact}$) plus the Fermi level shift imparted by the metal doping on the graphene ($\Delta E_{F,0}$) at zero gate voltage. $\Delta E_{F,0}$ can be tuned by application of finite gate voltages [103]. The dependance of the potential step at the contacts on the applied gate voltage (V_g) can be expressed as follows:

$$\Delta V = (\Phi_{contact} - \Phi_{graphene}) - \Delta E_{F,doping} \tag{5.2}$$

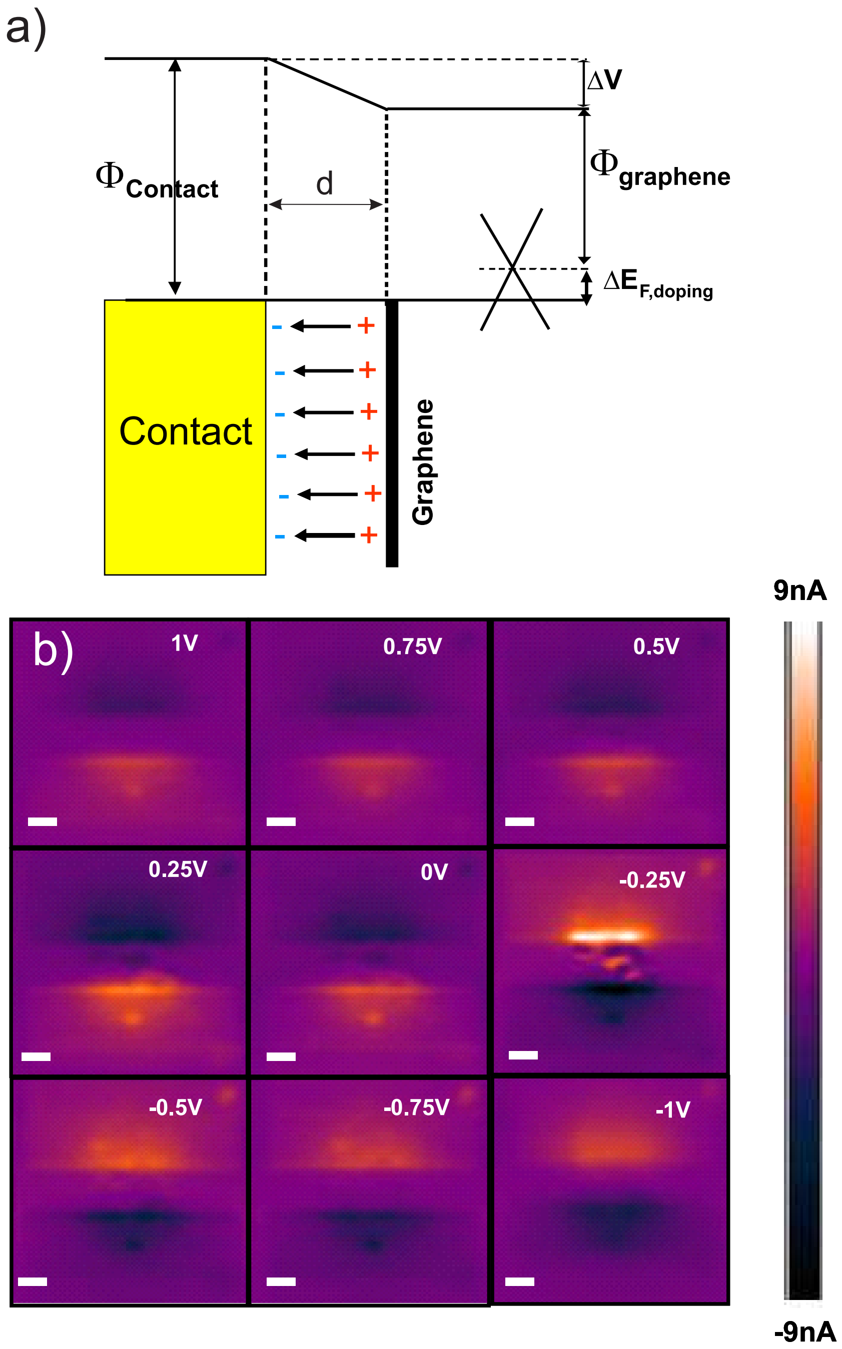

Figure 5.5: (a) Schematic illustration of the potential step formation at the metal-graphene interface where $\Phi_{graphene}$ is the work function of graphene,$\Phi_{contact}$ that of the metal in contact and $\Delta E_{F,doping}$ the Fermi level shift imparted by doping on the graphene, respectively.(b) Gate dependant photocurrent measurements illustrating switching of photocurrent polarity at the contacts.

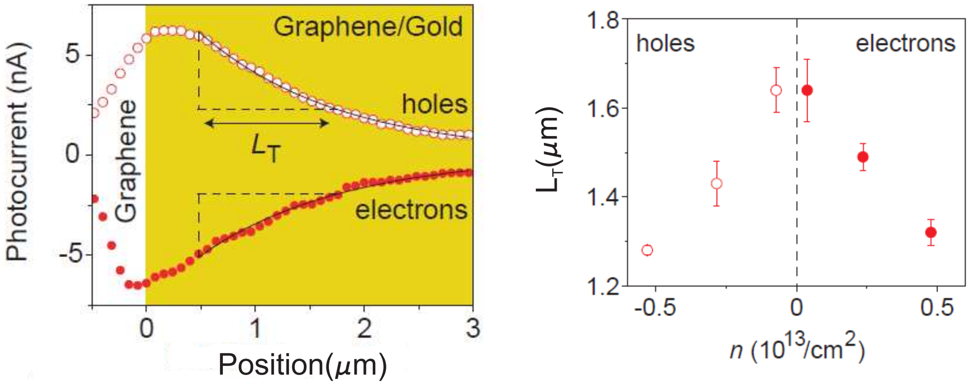

Figure 5.6: (a) Cross-section of the photocurrent maps of figure 5.5 (b) plotted at two different gate voltages on either side of the neutrality point depicting the decay of photocurrent away from the gold contact edge (x=0) further into the contact. (b) Variation of transfer lengths of charge carriers from graphene into the gold L_T upon modulation of the charge carrier density by application of a gate voltage

$$\Delta E_{F,doping} = \Delta E_{F,0} + sgn(V_g - V_g^{dirac})\hbar\nu_F\sqrt{\pi\alpha(V_g - V_g^{dirac})} \tag{5.3}$$

where $\alpha = 7.2 \times 10^{10}\ cm^2V^{-1}$ is the gate coupling factor and $\hbar\nu_F = 5.52\ eV$ [20, 140]. Thus, by application of gate voltage one can reverse the sign of the potential step and as a result the sign of the photocurrent by changing $\Delta E_{F.doping}$ according to equation (5.3). This can be experimentally observed by recording photocurrent maps of the entire device. Figure 5.5(b) shows photocurrent maps of the same device at different gate voltages. Switching of photocurrent signal at the contact regions upon sweeping the gate voltage from V_g=-1 V to 1V confirms the above theoretical prediction.

An important feature in the photocurrent map of figure 5.4 is the persistence of photocurrent signals under the gold contacts. This is also exemplified by the long decay tail of the photocurrent profile in figure 5.4(b)and 5.6. This finding implies that the separated charge carriers travel a distance L_T under the metal before transferring into the gold contact. The closed-circuit photocurrent is proportional to the local potential gradient that separates optically excited charge carriers, where x=0 is the position of the graphene-gold contact edge as depicted in fig. 5.6. The cross-sections taken from photocurrent scan images for two representative charge carrier densities (gate voltages) on either side of the neutrality point reveal that, despite some variations of the magnitude and functional form of the photocurrent in the vicinity of the contact edges, the photocurrent amplitude generally decays exponentially with distance from the contact edge. Fitting this decay thus delivers the transfer length L_T. In fig. 5.6(b), L_T values are plotted as a function of charge carrier density [‡]. Values as high as 1.6 μm were observed and the variation for electrons and holes is symmetrically distributed with respect to the charge neutrality point.

Accordingly, the contact resistance of a graphene device with gold contacts contains a contribution due to the scattering of the charge carriers in the graphene sheet below the contact, in addition to the scattering due to potential barrier for the transfer into the metal. Hence, the contact resistance is proportional to L_T which exhibits a maximum at the charge neutrality (Dirac) point (figure 5.6 (b)).

In order to further investigate the graphene in contact with a gold electrode the laser signal was collected back through the setup and recorded using a spectrograph (HR550, Horiba/YobinYvon) equipped with a grating having 300 grooves/mm and a liquid nitrogen cooled, back-illuminated, deep-depleted CCD array. The measured Raman spectra (integration times: 30 sec) were background-corrected before fitting the individual Raman features and deriving spectral peak positions as functions of charge carrier densities and current levels, respectively. Raman spectra were recorded by parking the laser spot at the region of interest. In order to avoid complexities arising due to the plasmon enhancement at the contact edge all measurements were taken at sufficient (>500 nm) distances from the edge of the gold film.

The Raman G peak in graphene arises due to a carbon-carbon E_{2g}-symmetry vibration, and is energetically located around 1585 cm^{-1} (as described in detail in chapter 2). The position of Raman G-band has been established to depend on charge carrier density in the sheet [101]. Confocal Raman measurement allows us to probe locally both the peak shift and the electron-phonon coupling in graphene upon application of gate voltage. Increasing the charge carrier density via the polymer gate (inset figure 5.7) results in G peak stiffening and a decrease in linewidth for both electron and hole doping. This G peak stiffening is due to the nonadiabatic removal of the Kohn anomaly from the Γ point [141](as described in more detail in Appendix I).

[‡] In polymer gate configuration, the charge carrier density is determined as function of according to the method of ref [101]:

$$V_{polymergate} - V_{Dirac} = \frac{\hbar \nu_F \sqrt{\pi n}}{e} + \frac{ne}{C_{polymergate}} \tag{5.4}$$

with the Fermi velocity $\nu_F = 1.1 \times 10^6 \ ms^{-1}$ and $C_{polymergate} = 2.2 \times 10^{-6} \ Fcm^{-2}$, corresponding to a Debye length of 2nm in the PEO gate.

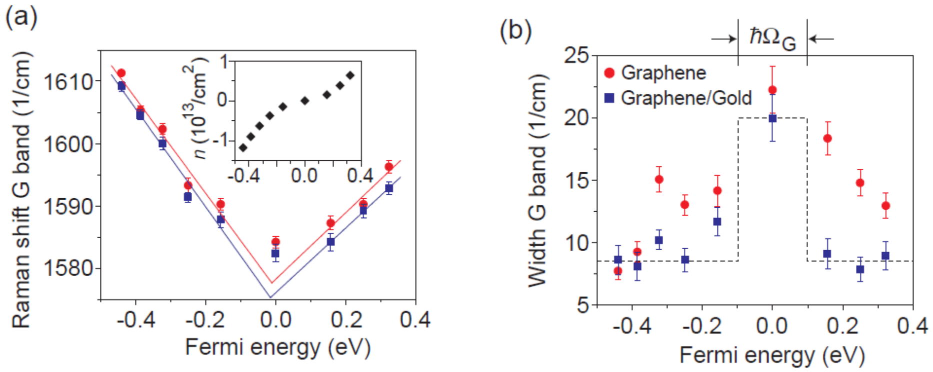

Figure 5.7: (a) Raman G peak shift plotted as a function of Fermi energy (tuned by gate voltage). The corresponding charge carrier density n is plotted as function of E_F in the inset. (b) Variation of the Raman G peak FWHM upon tuning the Fermi level. Dotted line indicates the step-like functional behavior of the G-band width around $E_F = \pm\hbar\Omega_G/2$ due to Landau damping.

In fig. 5.7(a), the Raman G band position is plotted as a function of the Fermi-energy [†]. Sweeping the Fermi energy in the graphene device across the charge neutrality point, results in a shift of the G-band frequency for both electron doping ($E_F > 0$) and hole doping ($E_F < 0$) (Appendix I) not only the graphene channel, but also in the area under Au. These shifts occur with about the same rate($52.1 \pm 0.9\ cm^{-1}eV^{-1}$ for electron doping and $79 \pm 7\ cm^{-1}eV^{-1}$ for hole doping), indicating that the electronic structure of graphene, including the charge neutrality (Dirac) point, is preserved in the gold-covered area in accordance with theoretical predictions described earlier.

Calculations based upon time dependant perturbation theory and the linear dispersion of graphene close to the Dirac point suggest the G band phonon energy to depend on the carrier density in the following manner [142]:

$$\Delta E_G(n) = \hbar\Omega_G - \hbar\Omega_G^0 = \lambda\left[|E_F| + \frac{\hbar\Omega_G}{4}\ln\left|\frac{2|E_F| - \hbar\Omega_G}{2|E_F| + \hbar\Omega_G}\right|\right] \qquad (5.6)$$

At higher charge carrier densities the linear term dominates over the logarithmic term in equation (5.6), such that the slopes of linear fits can be

---

[†] The Fermi energy as function of charge carrier densities is obtained by solving equation (5.4):

$$E_F(n) = sgn(n)\hbar\nu_F\sqrt{\pi|n|} \qquad (5.5)$$

used to determine the dimensionless coefficient λ and hence the electron-phonon coupling M_Γ as $\lambda = A_{uc}M_\Gamma^2/2\pi\hbar\Omega_G\nu_F^2 m_{carbon}$, where A_{uc} the area of graphene's unit cell, M_Γ the electron-phonon coupling of the longitudinal optical Γ-point phonon with E_{2g}-symmetry, and m_{carbon} is the atomic mass of carbon. Fitting the experimental data in the regimes of higher charge carrier densities (larger E_F-values) yields similar slopes for both areas of graphene (in the channel and under gold) as demonstrated by figure 5.7 (a). Thus, the electron-phonon coupling in the gold-covered graphene area that is close to the value obtained in the center of the graphene , providing further support to the hypothesis of weak perturbation of graphene by gold. The best fit to the data obtained in the gold-plated graphene segment delivers $M_\Gamma = 14 \pm 2$ for $E_F > 0$ and $M_\Gamma = 17 \pm 5$ for $E_F < 0$, in excellent agreement with results obtained for mechanically exfoliated, high-quality graphene [141].

Further evidence stems from the coincidence of the two curves at zero E_F which confirms the absence of significant Fermi level shifts associated with the gold graphene interface. Based on the model reported in ref. [135], the unperturbed Fermi level by the gold indicates an average distance of 3.2 Åbetween the gold and graphene layer, close to the theoretical equilibrium separation of 3.3 Å.

The similar G band widths (around $20cm^{-1}$) observed at the charge neutrality point in the two graphene areas (see Fig. 5.7 (b)) as well as their similar response to a change in charge carrier density, reveal that the decay pathways of optical phonons in graphene are only weakly affected by the presence of gold. At low carrier densities ($\Delta E_F = \hbar\Omega_G/2$ due to Pauli blocking above these carrier densities [see Appendix I]), the G band is damped due to decay processes associated with the formation of electron hole pairs [142]. This Landau damping process manifests itself in a step-like functional behavior of the G-band width (as shown in figure 5.7 (b)), which is even more pronounced in the gold-contacted graphene. This suggests that the gold layer effectively screens local potential heterogeneities, such as, trapped charge carriers in the dielectric substrate underneath the graphene [143] that are likely to cause the deviation from the step-like function for the graphene channel [142].

An important consideration in the performance of graphene based devices is the energy dissipation of charge carriers, especially in the case of devices where a large current is employed, or when the devices are operated at high frequencies (example, RF applications). The dissipated electrical power can then raise the operating temperatures to levels where device performance begins to get affected. The position of the Raman-active 2D-band around $2700cm^{-1}$ is strongly dependent on temperature and can be used as a local temperature probe [144].In fig. 5.8(b), the temperatures ex-

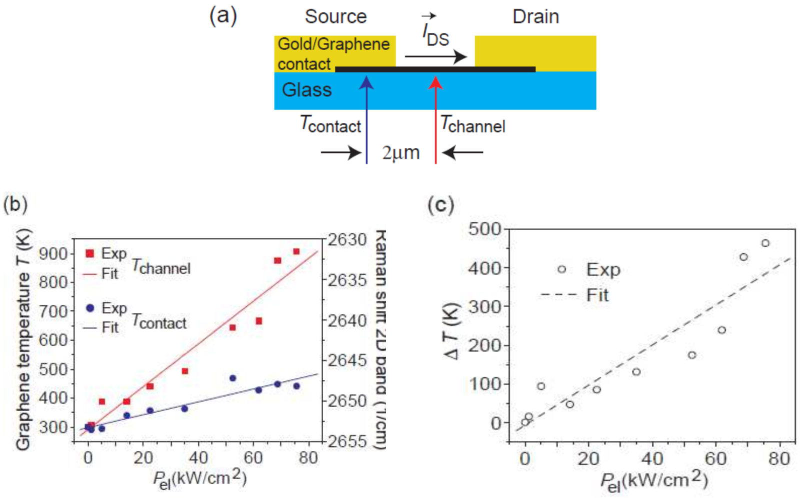

Figure 5.8: (a)Schematic of a current-carrying, two terminal graphene device without electrolyte polymer layer on top. The gold contacts serve as electrodes for charge carrier injection. The locations for the temperature measurement at the graphene-gold contact and in the graphene channel are separated by 2 μm (b) Temperatures, extracted by Raman spectra 2D peak shifts, plotted as a function of applied electrical power density, $P_{el} = V_{ds}I_{ds}/LW$ for the graphene in the channel (blue) and under the gold contact (red). (c)Measured temperature difference (rings) between the channel center and the gold contact of the graphene device and a linear fit (solid line) to the data.

tracted at the graphene-gold contact are compared with those obtained in the channel center of the same device as a function of electrical power density $P_{el} = V_{ds}I_{ds}/LW$. It is apparent that both graphene segments heat up linearly as function of P_{el}, albeit at different rates. The resulting temperature difference between device channel and contact increases linearly, plotted in fig. 5.8(c), reaches values as high as $\Delta T = 500K$. Such pronounced gradients impose a substantial risk of structural fragmentation and electrical breakdown in particular at the contact edges.

5.1.2 Non-invasive character of metal contacts in RGO devices

The charge transfer at the graphene-metal interface (as described in section 5.1.1) leads to a charge inhomogeneity that surrounds the metal contacts and extends to considerable distances inside the graphene channel, which manifests itself in a notable asymmetry between electron and hole conductance in such devices [128]. Moreover, the invasiveness of the metal contacts on graphene can notably influence electrical measurements even in the four-probe geometry [145]. In contrast, non-invasive metal contacts can be realized on chemically derived graphene obtained through the graphene oxide route.

The deposited GO monolayers with sizes of ~20 x 20 μm^2 were etched using oxygen plasma (200 W, 0.3 Torr, 15 seconds), followed by chemical reduction through two subsequent steps comprising hydrogen plasma treatment (0.8 mbar H_2 at 30 W power for ~6 seconds) and thermal annealing (by inserting sample in a preheated furnace at 400°C for 1 hour). Individual reduced and annealed monolayers with heights of ~1 nm, as identified by atomic force microscopy, were contacted with Ti/Au (1 nm / 30 nm) electrodes via a standard e-beam lithography process, resulting in a bottom-gated FET configuration with four probes as shown in figure 5.9(a). SPCM measurements were performed using a diffraction limited laser spot ($\lambda = 514$ nm, spot size ~0.4 μm, power ~100 kW cm^{-2}).

Electrical characterization of the as-fabricated RGO devices revealed two-probe resistances of 4 to 7 MΩ under ambient conditions. SPCM was employed to investigate the potential profile of the device. The reflection image of a device with four electrodes is depicted in figure 5.9(b), while figure 5.9(c) depicts the corresponding SPCM image recorded at zero source-drain and gate bias. The latter image reveals numerous spots of fluctuating sign throughout the sheet. This signal pattern, which displayed only a weak modulation upon sweeping the back gate voltage between ±60 V, reflects surface potential variations that may arise from defective sp^3-hybridized regions and areas of clustered topological defects remaining after the chemical reduction (as described in chapter 3). A small contribution could also be attributed to charged impurities located on the substrate akin to signatures of electron-hole puddles in SPCM images of pristine graphene [103, 139].

The photocurrent distribution in the as-fabricated devices clearly differs from exfoliated graphene with evaporated gold contacts by the absence of distinguishable signals at the contacts. It thus follows that no appreciable potential barriers are present at the interface between gold and the RGO, resulting in non-invasive contacts. This conclusion is corroborated by the

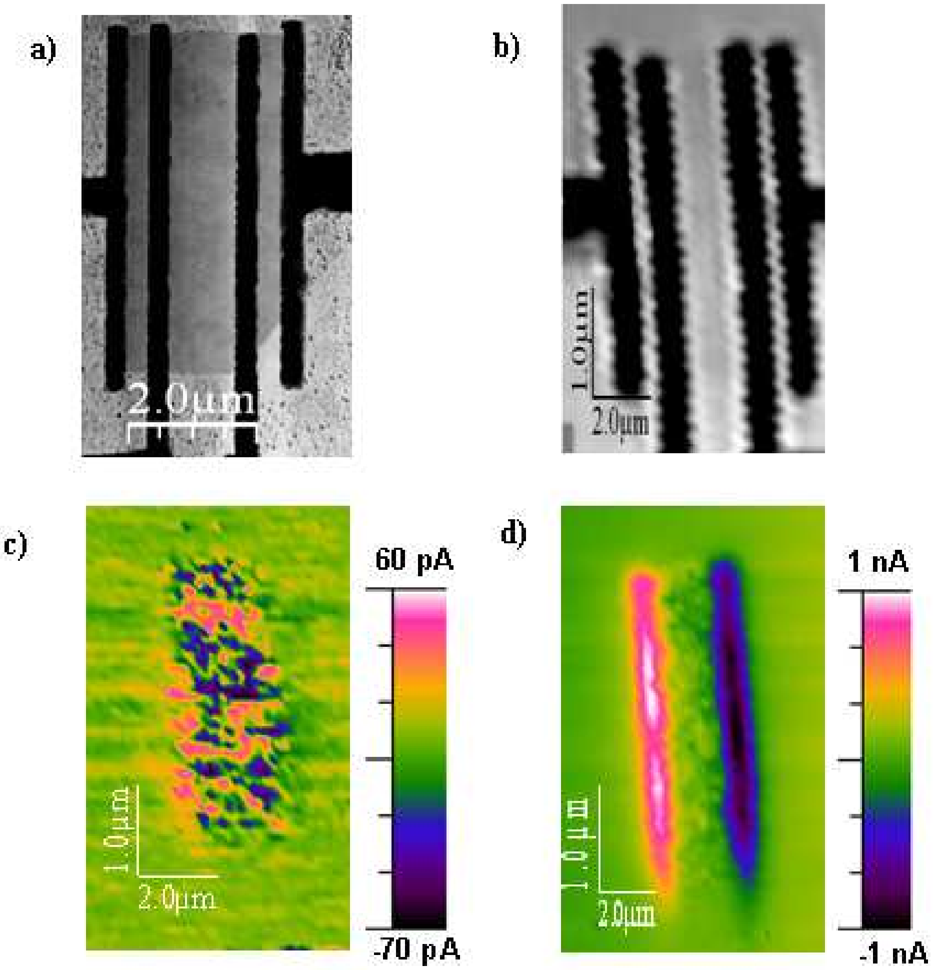

Figure 5.9: (a) AFM tapping mode image of an RGO layer contacted with four contact probes of Ti (1nm)/Au (30nm). (b) Reflection image measured during the acquisition of the photocurrent images for spatial correlation. (c) and (d) Photocurrent images taken at $V_d = V_g = 0$ V of the as-fabricated and annealed device (at 300 $°C$), respectively.

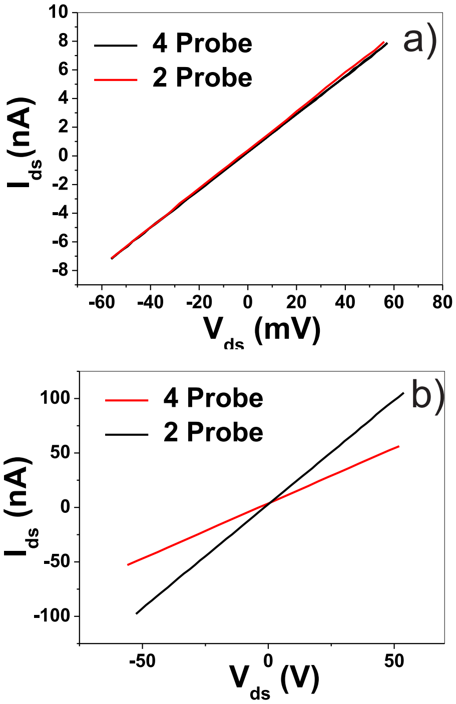

Figure 5.10: Four- and two-probe measurements at room temperature of an (a) as prepared and (b)annealed device.

fact that four- and two-probe electrical measurements on the devices yielded approximately the same electrical resistance as shown in figure 5.10(a). The absence of potential barriers may be attributed to the substantial density of defects (e.g., topological defect clusters) contained in the RGO , which block the formation of an intimate gold-graphene interface [146].

The above hypothesis, was tested by annealing the RGO devices. We found that a treatment above 300 °C (for 1 hour under argon atmosphere) causes a significant change in the SPCM response, specifically the emergence of pronounced photocurrent signals close to the contacts, indicative of the creation of local potential barriers (figure 5.9(d)). This change thus signifies the annealing-induced formation of intimate contacts between gold and the carbon with concomitant transfer of charge at the gold-carbon interface. As a further change after annealing, the transfer characteristics measured under a He atmosphere display a shift of the current minimum (i.e., Dirac point) toward more positive gate voltages by ∼60 V (figure 5.11(a). Such positive

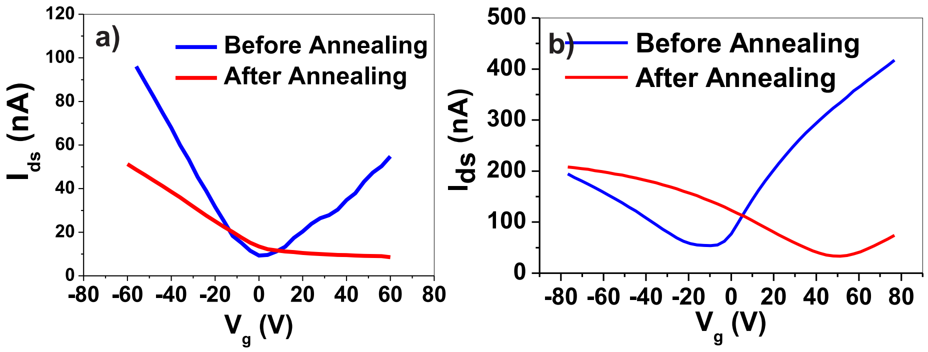

Figure 5.11: (a) Transfer characteristics ($I_{ds} - V_g$ curves) of an RGO device measured at 100 mV bias under Helium atmosphere at 240 K before and after annealing at 300°C. (b) Comparison of the transfer characteristics (acquired at V_{bias}= 1 mV) of a mechanically exfoliated graphene device before and after annealing under the same conditions as in panel (a).

shift is indicative of p-type doping of the RGO channel. The sheet doping is likely to originate from the lateral diffusion of gold atoms from the contacts along the RGO sheet during the annealing process. Indeed, noble metal induced p-type doping of graphene has been documented for gold-decorated epitaxial graphene upon annealing [147].

A similar doping effect, as manifested in a pronounced positive shift of the Dirac point, could also be observed for gold-contacted mechanically exfoliated graphene after annealing under the same conditions (figure 5.11(b). However, while in the latter case the slope of the hole branch (for not too negative gate voltages) remains largely unaltered, it is strongly reduced in the RGO device. One plausible explanation for this difference involves reduced Klein tunneling in the disordered RGO, which would impede the charge transport through the potential barriers formed between the p-doped contact regions and the central RGO channel whose Fermi level position is modulated by the applied back gate voltage (figure 5.12).The suppression of Klein tunneling by the presence of disorder in graphene is in accord with theoretical predictions [148]. Support for the relevance of this effect in the annealed RGO devices derives from the finding of an increasingly suppressed slope of the hole branch with the magnitude of the photocurrent signal detected close to one of the contacts, as is apparent from the plots in figure 5.13 belonging to three different RGO devices that reflect the sample-to-sample variation despite their identical treatments. The observed trend is consistent with the change of the photocurrent signal, which is proportional to the local electric potential

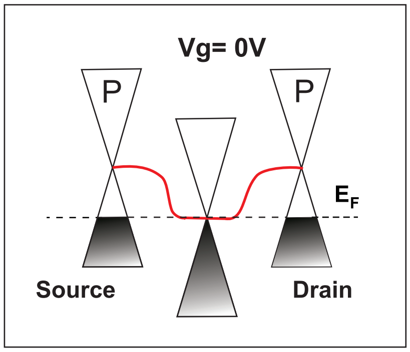

Figure 5.12: Schematic representation of the potential barriers formed within an annealed RGO device at zero back gate voltage. Upon application of a back gate voltage, the Fermi level of the p-doped regions close to the gold contacts remain pinned, while it shifts within the central graphene channel.

gradient in these devices. It is interesting to note that for the RGO devices at $V_g = 0$ V, the resistance increase due to the suppression of Klein tunneling is roughly compensated by the resistance decrease due to gold-induced p-type doping, whereas the latter effect is predominant in the exfoliated graphene device which accordingly displays a resistance decrease at $V_g = 0$ V.

5.2 Conductivity improvement of RGO by CVD repair

Chemical reduction converts the close-to-insulating GO into sheets with up to four orders of magnitude higher electrical conductivity (see chapter 2). Such chemically derived graphene is a versatile basis for fabricating thin conductive films on solid supports, thus opening access to transparent flexible electrodes. For monolayers of reduced GO, only moderate values (0.15 Scm^{-1}) of electrical conductivity have been found , as described in chapter 4. This is attributed to the presence of topological defects or residual functional groups remaining after reduction. Although such values of conductivity are sufficient for many applications, strategies to heal these defects are needed for more demanding device applications. In this section, a novel Chemical Vapor Deposition (CVD) based approach is explored that enables the substitution of carbon atoms contained within the defective areas. In this manner, chemically derived graphene sheets of large dimension and with two orders of magnitude enhanced conductivity, compared to the RGO, can be obtained.

The CVD induced healing process starts with the deposition of the GO

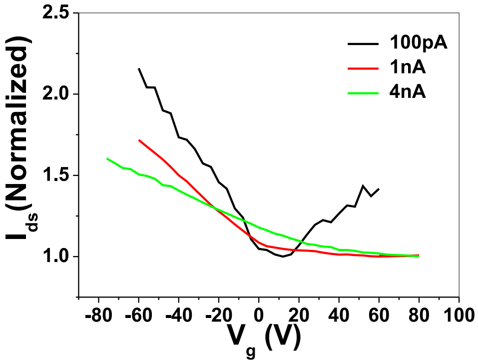

Figure 5.13: Transfer characteristics of three different RGO devices (after annealing at 300 °C) exhibiting different photocurrent magnitudes detected close to one of the gold electrodes.

sheets onto degenerately doped silicon substrates covered by a thermally grown SiO_2 layer (300nm thickness). These samples were then placed in a quartz tube furnace and subjected to a flow of mixture comprising 1500 sccm of H_2 and 200 sccm of Ar for 20 min at 500 °C. The two-probe electrical conductivity of the hydrogen-treated sheets was found to range between 0.1 and 2 Scm^{-1} at room temperature. These values are in close correspondence to those observed after GO reduction by hydrazine or hydrogen plasma, as described in chapter 4. Increasing the reduction temperature to 900 °C or the reaction time up to 60 min provided very similar results. This finding suggests that the electrical conductivity is limited by the presence of defects in the form of vacancies, which cannot be healed by annealing or reduction.

The main CVD step, which turned out to be crucial for obtaining improved conductivity, is performed after reduction in the same furnace. The CVD is carried out using ethylene as a carbon source, under conditions (2 sccm ethylene for 3 min at 800 °C) that are very similar to those in the CVD synthesis of single-wall carbon nanotubes on SiO_2 substrates [149], however without the need of metal catalysts as in the latter case.

AFM characterization of the same monolayers before and after the two-step process showed no detectable height and lateral increase within the resolution of the AFM, ruling out the possibility of growth of a second layer of graphene. Figure 5.14 illustrates the improvement in conductivity of reduced GO and CVD treated GO in comparison with GO and pristine graphene. The resulting monolayers (CVDGO) exhibited room temperature conductivities in the range of 10-350 Scm^{-1}, corresponding to an average increase

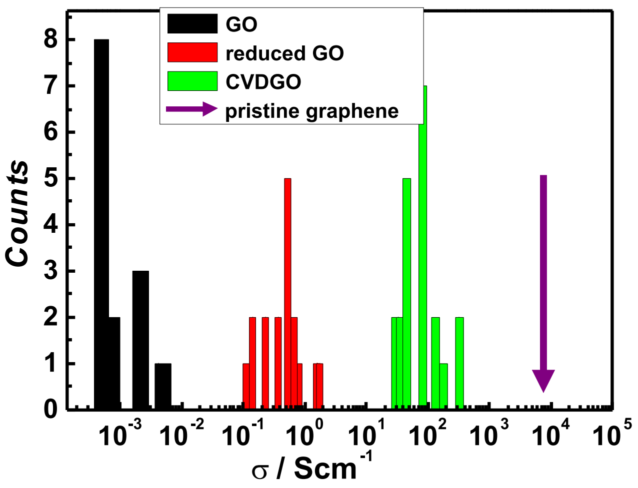

Figure 5.14: Histogram of the experimentally determined electrical conductivity distribution for monolayers of GO, reduced GO,CVDGO and the conductivity of pristine graphene extracted from ref. [2]

in conductivity of two orders of magnitude over the RGO sheets. The CVD step proved to be quite insensitive to variations in the flux rate (nominally 16 sccm) and deposition time (nominally 16 min), whereas a critical dependence on temperature was observed (optimum value ~800 °C). Lower temperatures resulted in samples with unaltered conductivity, while higher temperatures led to complete degradation of the reduced GO layers.

Four-probe electrical measurements on CVDGO monolayers indicate that contact resistances make a measurable contribution to the overall resistance of the contacted monolayers. As a representative example, a sheet showing a total resistance of 14 kΩ exhibits a contact resistance of 4 kΩ. The latter value is in agreement with the extrapolation from the corresponding dependence of resistance on contacted length (fig. 5.15(a)). At the same time, the linear dependence of the plot rules out ballistic transport through these devices. Low temperature four-probe measurements revealed that the contact resistance does not become dominant even at low temperatures. Further support for this contact resistance contribution can be drawn from SPCM image of the device shown in figure 5.15(b)and (c) (at zero bias and gate conditions). The similarity of the photocurrent features to that exhibited by pristine graphene devices [103] reflects the presence of potential steps at the gold contacts due to charge transfer.

Electrical studies were also performed in field-effect transistor (FET) con-

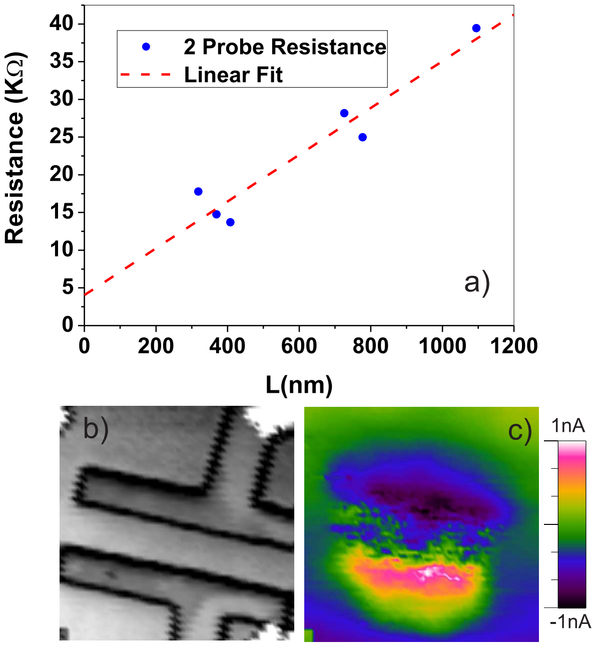

Figure 5.15: (a) Room-temperature two-probe resistance as a function of channel length measured on the device. The resistance increases linearly with channel length with an intercept at 4 kΩ, which corresponds to the contact resistance. (b) Confocal microscopy reflection image and (c) the corresponding SPCM image clearly showing signals at contacts

figuration, with the degenerately doped silicon wafer utilized as back gate (fig. 5.16). From the acquired transfer characteristics, room-temperature field-effect hole mobilities up to 100 $cm^2V^{-1}s^{-1}$ were extracted for CVDGO (corresponding to a more than 50-fold increase over the RGO). For all CVDGO samples, even when measured under an He atmosphere, a pronounced shift of the current minimum (Dirac point) toward positive gate voltage was observed. Such p-type doping is in contrast to the behavior of mechanically exfoliated graphene, in which the Dirac point moves closely to V_g=0 V upon oxygen removal [16]. Significant p-type doping has also been observed in other chemically derived graphene samples, and attributed to the presence of positively charged species screening the gate-induced electric field [150].

Despite the improved conductivity of the samples, evidence for a significant number of defects in the CVDGO was obtained from Raman spectra, which exhibit a very intense D-line at ~1350 cm^{-1} in addition to the G-line

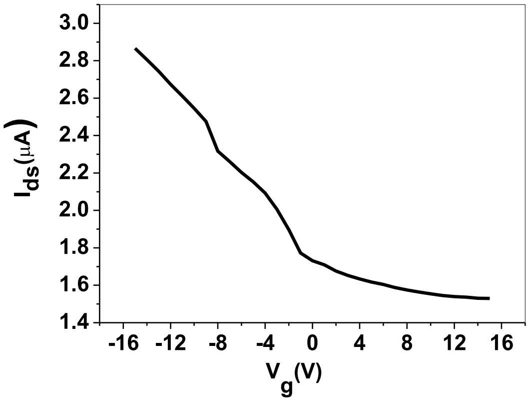

Figure 5.16: Transfer characteristic of a CVD repaired GO device. Drain-source current as a function of back gate voltage for a device at 240 K under a helium atmosphere

below 1600 cm^{-1}. In addition, the D/G intensity ratio in CVDGO is found to be larger than for chemically reduced GO as shown in figure 5.17 (a and b). The CVDGO exhibits an approximately linear rise of electrical conductivity with increasing D/G ratio (Figure 5.17(c)), a trend that appears counter-intuitive on first impression. One possible reason for these features is the deposition of amorphous carbon onto the substrate during the CVD process. However, this scenario can be excluded in view of the essentially preserved AFM height and area of the sheets, as well as the fact that no carbon-related Raman signal could be detected upon examination of the Si/SiO_2 substrate background. An alternative, plausible explanation draws upon the above-mentioned model underlying the TuinstraKönig relation which as a measure for the size of sp^2-domains,(as applied in chapter 3) based upon the assumption that the G-peak scales with the domain area and thus grows with the square its radius r^2, whereas its defectcontaining circumference changes as r. This model involves the creation of small patches of graphene within holes and amorphous areas of the reduced GO simultaneously by carbon incorporation during the CVD step. The small size of these holes is expected to restrict the size of the new graphene islands to just a few nanometers, and to promote a certain mismatch with respect to the surrounding graphene lattice (illustrated in figure 5.18). On this basis, the increased D/G ratio emerges as a direct consequence of the increased number of small nascent regions.

The CVDGO monolayers display a decrease in conductivity by more than

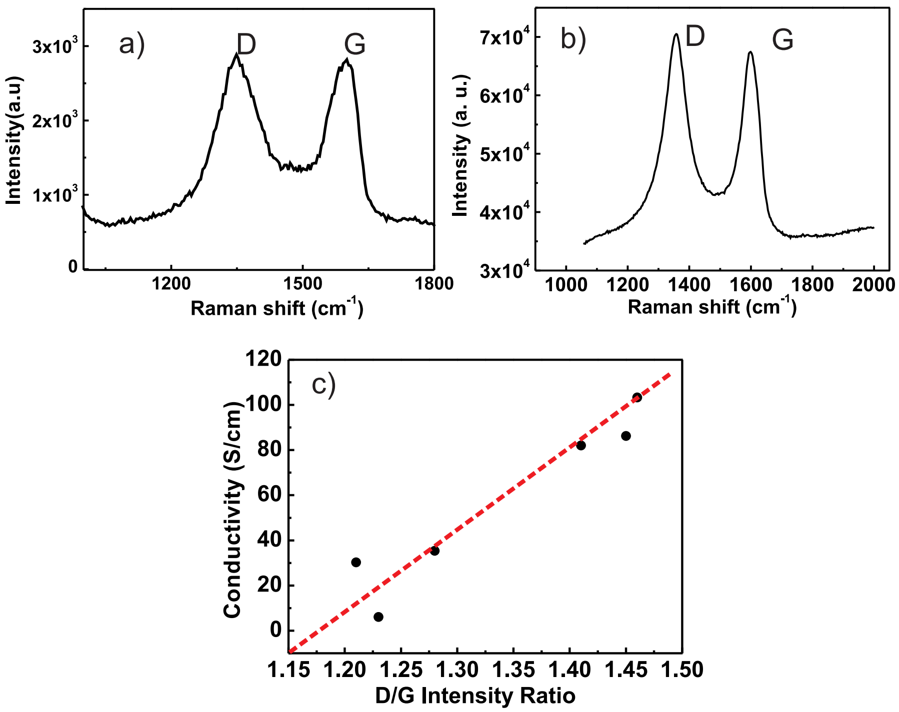

Figure 5.17: Representative Raman spectrum of (a) RGO monolayer and (b) CVDGO monolayer displaying a D/G ratio larger than RGO. (c) Plot of conductivity vs. D/G intensity ratio displaying a monotonic rise with conductivity.

one order of magnitude upon cooling from room temperature to 4 K, in contrast to exfoliated graphene that exhibits a conductivity decrease with increasing temperature due to the enhanced electron-phonon scattering [127]. This difference provides evidence that the electrical transport mechanism in the present samples is, despite the significant higher conductivity, more akin to chemically reduced GO. In fact, the temperature dependence of the measured source-drain current (see fig. 5.18 (b)and (c)) fits well to the following relation describing two-dimensional variable-range hopping (chapter 4) in parallel with electric field-driven tunneling I_0 as :

$$I(T) = I_1 \exp\left(-\frac{B}{T^{1/3}}\right) + I_0 \tag{5.7}$$

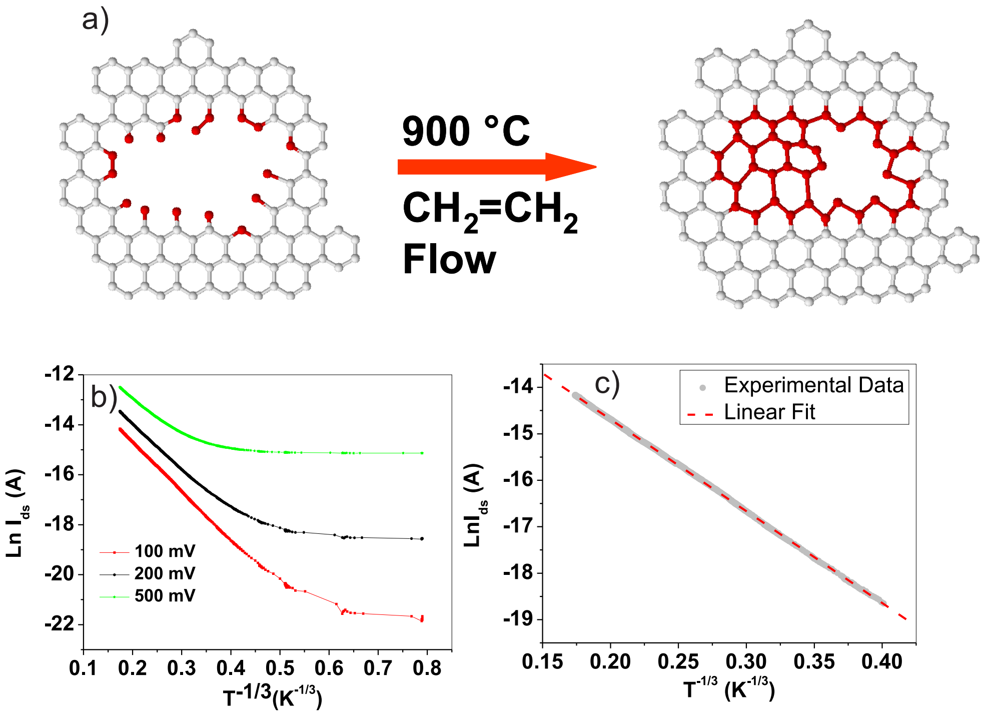

Figure 5.18: (a) Schematic illustration of the process of defect healing in RGO using CVD process. The newly formed carbon lattice exists with a mismatch to the parent lattice. (b) Plot of drainsource current (I_{ds}) against $T^{-1/3}$ at different V_{ds} applied to a CVDGO monolayer. (c) Magnified view of the hopping regime at low bias (100 mV). A two dimensional variable range hopping model yields a perfect linear fit.

$$B = \left(\frac{3}{k_B N(E_F) L_l^2}\right)^{1/3} \tag{5.8}$$

where T is the temperature and B the hopping parameter, defined by equation (5.8), k_B is the Boltzmanns constant, $N(E_F)$ the density of mobile carriers, and L_l the localization length. For this transport mechanism, the tunneling term (I_0) becomes the dominant contribution at lower temperatures and high electric fields. Compared to chemically reduced GO monolayers, the CVDGO sheets exhibit a lower slope (upto 50 %) in the $\ln(I/A)$ vs. $T^{-1/3}$ plots, implying either a larger localization length, L_l, or a larger density of mobile carriers, $N(E_F)$. Both possibilities are consistent with the creation of new nanometer-sized sp^2 islands, as these would contribute more mobile charges and also enhance carrier delocalization due to reduced the defect areas.

5.3 Conclusions

Influence of gold contacts on CVD graphene devices have been studied by photocurrent measurements which revealed a strong potential step manifested by the form of photocurrent maxima at the gold contact-graphene edge. Furthermore, this photocurrent shows an exponential decay into the contact away from the edge. The charge carriers travel along the graphene sheet over lengths above 1 μm. An accurate physical origin of the local potential drop at the contact edge and its exponential functional form is still not classified. Nonetheless, an asymmetrically screened electrostatic dipole field at the contact edges caused by the charge transfer is likely to be responsible for the charge carrier separation. This model is consistent with the observed gate-dependent polarity change of the measured photocurrent. Raman spectroscopy data reveal that the charge neutrality point and electron-phonon coupling in graphene, remain intact upon gold deposition. The charge carrier density in gold-covered graphene can be tuned with high efficiency. Thermal coupling at the graphene-gold interface enables the gold contacts to act as heat sinks that results in strong temperature differences which might play an essential role in the thermal management of future graphene-based electronics.

The inherent defective nature of chemically derived graphene prepared by the GO route results in non-invasive (gold) contacts characterized by the absence of potential steps. This behavior is in contrast to exfoliated graphene, wherein metal contacts principally generate macroscopic charge inhomogeneities which interfere with four-probe measurements. At only moderately high temperatures (ca. 350 °C), both types of graphene are prone to diffusion of gold atoms from the contacts, a property that should be considered in the future fabrication of graphene-based devices.

Finally, chemically derived graphene with good electrical conductivity is accessible through CVD-based defect healing in reduced graphene oxide. The obtained material displays, despite its significant content of residual defects, a mobility exceeding that of the molecular semiconductors currently used in organic electronics (upto 100 $cm^2V^{-1}s^{-1}$). The contained defects may be exploited as suitable anchor sites for chemical functionalization, or for optical applications [151, 152]. Moreover, the easy up-scalability of the two-step process could establish chemically derived graphene as useful component of a wide range of flexible, low-cost electronic devices. Finally, further advancement in the CVD synthesis of carbon nanostructures [50] could act as a driving force to successfully grow more extended sp^2 regions inside the sheets, and hence further approach the electrical performance of pristine graphene.

Chapter 6

Summary and Outlook

The extraordinary properties of graphene have spurred extensive research on alternative and scalable methods of its synthesis. In this thesis, one such alternative based on the chemical exfoliation and reduction of graphite oxide has been explored. To this end, graphene oxide and reduced graphene oxide were prepared by the chemical oxidation of graphite and their structure and electrical properties, evaluated in detail.

In the first part of this thesis, the complex atomic structure of chemically derived graphene was unraveled using Raman spectroscopy, TEM and NEXAFS. The analysis revealed a considerable amount of disorder in the carbon lattice as evidenced initially by a strong D band contribution. The Raman D/G peak ratio was used to calculate the average size of the crystalline lattice which was of the order of 6 nm. Further insight was provided by TEM investigation of these layers by real space atomic resolution imaging, which confirm the presence of a substantial amount of various topological defects after reduction. The local chemical structure of this material probed by NEXAFS exhibit majority sp^2 hybridized carbon atoms, along with oxidized patches, containing carbonyl groups, epoxide and hydroxyl groups attached to aromatic rings as well, as carboxyl groups likely attached to the edges of the membranes.

Reduced graphene oxide, like its mechanically exfoliated counterpart, exhibits ambipolar transfer characteristics with room-temperature conductivities of up to 5 Scm^{-1} and carrier mobilities of up to 1 $cm^2V^{-1}s^{-1}$. These moderate values are a consequence of defects in the lattice that cannot be healed during the reduction process. A strong difference in the charge carrier transport of this material in comparison pristine graphene is apparent at low temperatures. Unlike structurally perfect graphene where coherent transport is limited by phonon scattering, defects in RGO form barriers to electronic transport. The charge transport thus takes place through 2D variable range hopping in parallel with field driven tunneling. The calculated mean hopping distance is in accordance the presence of regions of high conductance that are separated by regions of hopping conduction (localized states in defective areas).

Graphene based devices are promising for application in high performance electronics as a possible successor of silicon. However, the performance graphene based devices is strongly governed by the nature of the metal contacts. Thus, a detailed study of the graphene-metal interface performed using SPCM and Raman spectroscopy for both high quality graphene and RGO. SPCM of gold contacts to CVD graphene clearly demonstrated their intrusive nature as reflected by the presence of a strong potential steps at the edge of the contact. The graphene under the gold contact away from the edge, however, seems to be largely unperturbed by adsorbed gold. Raman spectroscopy reveals that charge neutrality point and electron-phonon coupling in graphene, remain intact upon gold adsorption. The charge carrier density in gold-covered graphene area can be tuned with high efficiency. SPCM data of graphene under gold indicates that the charge carriers travel above 1 μm in the graphene before transferring into the gold contact. This phenomenon suggests scaling limitations for gold contacts in electronic devices. Further more the thermal coupling at the graphene-gold interface is expected play an essential role in the thermal management of future graphene-based electronics. By contrast, contacts (Gold) to reduced graphene oxide devices exhibit a non-invasive nature characterized by the absence of photocurrent signals in the region of the contacts. This behavior is preserved until 300 °C after which gold forms intimate contact with the RGO interface resulting in a potential barrier at the contact similar to high quality graphene devices.

The synthesis of graphene based materials by chemical reduction graphene oxide is a versatile, cost effective and upscalable technique that can be utilized to fabricate functional devices with moderate performance. In order to render this technique more competitive a chemical vapor deposition based treatment was devised to improve the electrical conductivity of the graphene. A detailed study of the properties of GO sheets after defect healing by CVD revealed monolayer with conductivities upto 350 Scm^{-1} and mobilities up to 100 $cm^2V^{-1}s^{-1}$ representing an increase over conventionally reduced graphene oxide. With the aid of Raman spectroscopy and low temperature transport measurements, it was found that the improved material still contains a significant amount of residual defects.

The ability to synthesize chemically derived graphene in solution provides unique advantages. For example, it enables the controlled placement of the sheets , which represents an essential prerequisite for the fabrication of integrated device architectures. This advantage has been put to practical use

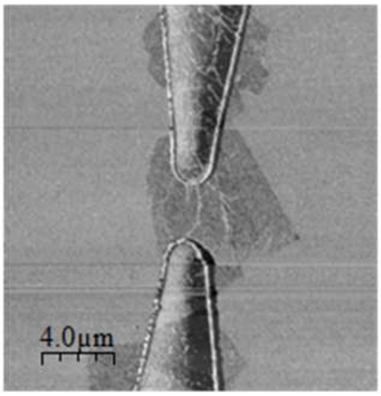

Figure 6.1: AFM micrograph of a graphene oxide flake trapped between two gold electrodes using dielectrophoresis

in this work by fabricating GO based devices by dielectrophoretic deposition from its suspension over pre-patterned electrodes (figure 6.1). This technique utilizes the force exerted on a dielectric object within a non-uniform electric field, there by eliminating the need for time consuming lithography.

Disorder in graphene oxide can be utilized in the study of defect mediated physics. One such example is the photoluminescence of graphene oxide. The presence of nanometer sized graphene islands in this material results in the opening of an optical band gap due to quantum confinement [152] as can be discerned in the photoluminescence spectrum in figure 6.2. Harnessing this phenomenon in graphene oxide could pave the way toward graphene-based optoelectronics.

In addition, defects in GO constitute useful sites for the chemical modification of graphene using established carbon surface chemistry. Chemical functionalization of these sheets to realize of highly selective sensors, while preserving the unprecedented surface-to-volume ratio provided by the 2D structure of graphene. Devices prepared by the dielectrphoretic deposition method were equipped with a microfluidic channel in order to test the device response to liquid gating [‡]. Measurements were performed using AC bias instead of a traditional DC method to efficiently overcome offsets arising due to charged species in liquids. A sample measurement performed to characterize the liquid gating response of unfunctionalized reduced graphene oxide

---

[‡] Gating by utilization of ions presence in liquids. Application of a voltage splits the ions in the liquid thereby forming an electrochemical Debye layer over the surface of the graphene sheet. The magnitude and polarity of this layer can be controlled by the applied voltage. A specific advantage of the liquid gating, the voltages required to switch from the p- to n-type regime are quite low.

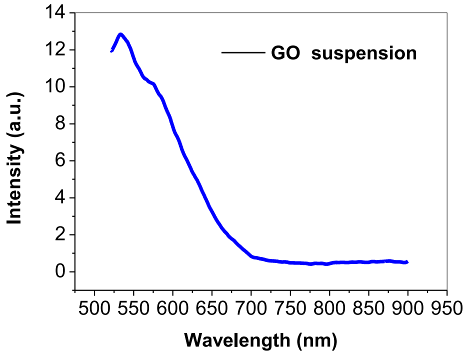

Figure 6.2: Photoluminescence spectra of suspension of graphene oxide excited at 514 nm

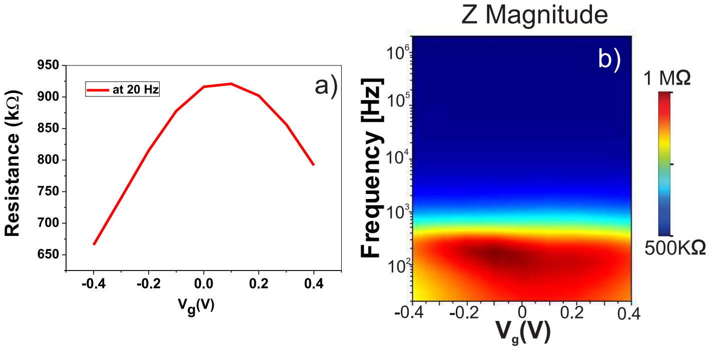

Figure 6.3: (a) Low frequency impedance measurement of liquid gating in Phosphate buffer (pH=7, 10mM and 0.1M NaCl) (b) A colour scale map of the real part of the impedance as a function of varying frequency and liquid gate voltages

is shown in figure 6.3. On this basis, first steps have been undertaken toward detecting the β-amyloid peptide.

Amyloid beta (Aβ) is a peptide composed of 39-43 amino acids that appears to be the main constituent of amyloid plaques in the brain of Alzheimer's disease patients. The strategy for the electrical detection of this peptide relies upon on the utilization of the $-COOH$ functionalities on RGO. The carboxylic acid functionalities are first activated by the well established EDC-NHS coupling [153]. The activated groups are then exposed to the Aβ antibodies, which then couple to the carboxylic acid functionalities. To test the sensing capability, a control measurement is first perfomed in pH=7 phosphate buffer. Figure 6.4 shows a change in the transfer characteristics when more than 50 pM Aβ peptide is introduced. Thus, the utilization of rem-

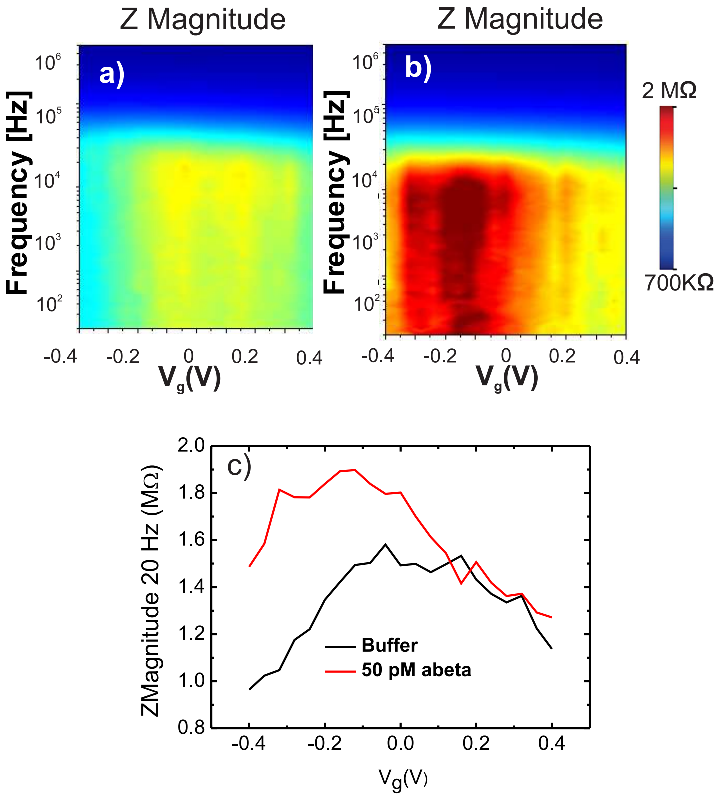

Figure 6.4: Colour scale map of the real part of the impedance as a function of varying frequency and liquid gate voltage when RGO device functionlized with Aβ antibodies upon exposure to (a) phosphate buffer (pH=7, 10mM and 0.1M NaCl), and (b)50 pM Aβ peptide in the same buffer. (c) Low frequency impedance response showing the shift of the transfer characteristics upon exposure to 50 pM Aβ peptide.

nant functional groups in reduced graphene oxide by appropriate chemical modification results in a device that is highly selective towards the target analyte. Further optimization of this approach (for example based upon the more abundant $-OH$ groups on RGO) could lead to sensors with higher sensitivity.

Appendix I

Non-Adiabatic Removal of the Kohn Anomaly in Graphene

The adiabatic Born Oppenheimer approximation assumes that the atomic vibrations are screened adiabatically by the adjustment of lighter electrons. This approximation fails in graphene which enables the calculation of doping levels in graphene by Raman G peak stiffening.

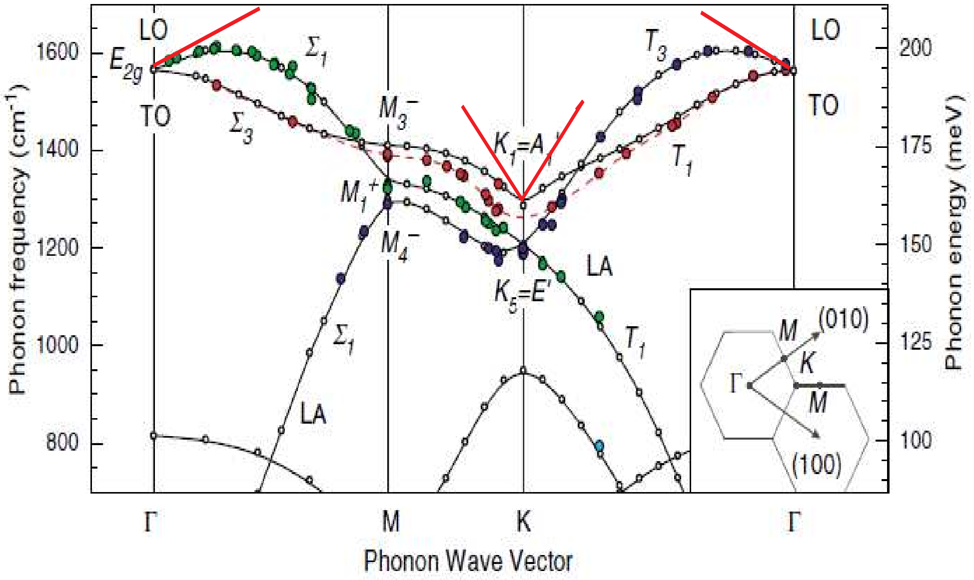

Figure A: Phonon dispersion of graphene obtained from ref. [154]. The red lines are guides for the eye, emphasizing the presence of the two Kohn anomalies at Γ and K. Inset shows the Brillouin zone construction of graphene with its high symmetry points.

The Raman G peak in graphene corresponds to E_{2g} symmetry vibration near the Γ point of the Brillouin zone. At this point, the phonon dispersion of graphene exhibits a Kohn anomaly (abrupt change in the vibrations associated with points in the Brillouin zone) which manifests itself as a softening of the phonon wave vector $\vec{q} \sim 2\vec{k_F}$, where $\vec{k_F}$ is the Fermi surface wavevector (figure A). Physically, the Kohn anomaly can be attributed to the electron-phonon coupling in a material.

In graphene, Kohn anomalies occur at the $\Gamma(\vec{q} = 0)$ and $K(\vec{q} = K)$ points, as indicated by red lines in figure A. By doping graphene, the change in the Fermi surface moves the Kohn anomaly away from $\vec{q} = 0$. Thus, since Raman scattering probes $\vec{q} = 0$ phonons, one intuitively expects a stiffening of the $\vec{q} = 0$ G peak. Within the adiabatic Born Oppenheimer approximation, the variation of electronic energy as function of displacement of constituent atoms u (E_{2g} symmetry vibrations) can be calculated [141] as:

$$\Delta E(u) = \frac{4A}{(2\pi)^2} \int\limits_{\epsilon(k,\pi^*,u)<\epsilon_F} \epsilon(k,\pi^*,u) d^2k \tag{1}$$

where $\epsilon_F > 0$ and A= 5.24 Å^2 is the unit cell area. From this equation, it follows that the Raman G peak does not depend on the doping level in contradiction to experiments reported in refs. [101, 141] and chapter 5 of this thesis. The G peak shift can be described analytically by considering non-adiabatic contributions as:

$$\Delta E(u) = \hbar\Omega_G - \hbar\Omega_G^0 = \lambda \left[|E_F| + \frac{\hbar\Omega_G}{4} \ln \left| \frac{2|E_F| - \hbar\Omega_G}{2|E_F| + \hbar\Omega_G} \right| \right] \tag{2}$$

where the dimensionless coefficient $\lambda = A_{uc}M_\Gamma^2/2\pi\hbar\Omega_G\nu_F^2 m_{carbon}$, A_{uc} the area of graphene's unit cell, M_Γ the electron-phonon coupling of the longitudinal optical Γ-point phonon with E$_{2g}$-symmetry, and m_{carbon} is the atomic mass of carbon. Thus, non-adibatic processes are responsible for the stiffening of the Raman G peak.

Sharpening of Raman G peak width due to doping

The Raman G peak width (Γ_G) exhibits a sharpening upon tuning the Fermi level, as exemplified in chapter 5 and refs. [101,142]. At low carrier densities, this can be understood as a Landau damping phenomenon where the vibrational mode decays into electron hole pairs as depicted in figure B. When

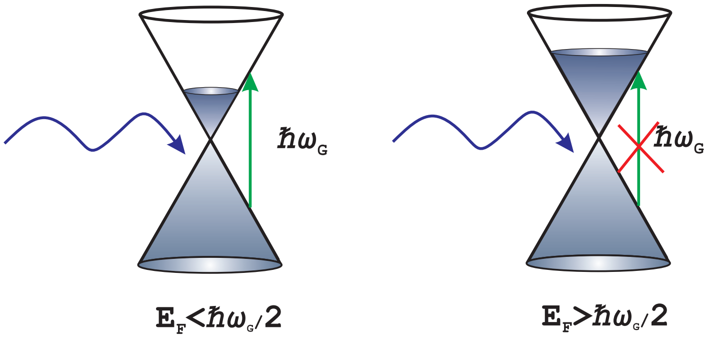

Figure B: Schematic representation of the Landau damping processes leading to G peak broadening at $E_F < \hbar\omega_G/2$ and sharpening at $E_F > \hbar\omega_G/2$ due to forbidden electron hole pair formation due to Pauli's exclusion principle.

the Fermi level is increased beyond $\hbar\omega_G/2$ (where ω_G is the Γ point phonon frequency), these decay processes are suppressed due to Pauli's exclusion principle, which causes narrowing of the G peak at higher carrier densities.

Bibliography

[1] Simon C Morris. *Life's Solution: Inevitable Humans in a Lonely Universe*. Cambridge University Press, 2003.

[2] K. S. Novoselov, A. K. Geim, S. V. Morozov, D. Jiang, Y. Zhang, S. V. Dubonos, I. V. Grigorieva, and A. A. Firsov. Electric field effect in atomically thin carbon films. *Science*, 306(5696):666–669, October 2004.

[3] Nicholas Kybert A.T. Charlie Johnson Brett Goldsmith, Ye Lu. Dna-decorated graphene chemical sensors. *Bulletin of the American Physical Society APS March Meeting 2010*, 2010.

[4] INFINEON. *Ed:CNTFET*.

[5] Zhihong Chen, Yu-Ming Lin, Michael J. Rooks, and Phaedon Avouris. Graphene nano-ribbon electronics. *Physica E: Low-dimensional Systems and Nanostructures*, 40(2):228 – 232, 2007. International Symposium on Nanometer-Scale Quantum Physics.

[6] H. W. Kroto, J. R. Heath, S. C. Obrien, R. F. Curl, and R. E. Smalley. C(60): Buckminsterfullerene. *Nature*, 318:162, November 1985.

[7] Sumio Iijima. Helical microtubules of graphitic carbon. *Nature*, 354(6348):56–58, November 1991.

[8] A. K. Geim and K. S. Novoselov. The rise of graphene. *Nature Materials*, 6(3):183–191, March 2007.

[9] Mikhail I. Katsnelson. Graphene: carbon in two dimensions. *Materials Today*, 10(1-2):20 – 27, 2007.

[10] K. S. Novoselov, Z. Jiang, Y. Zhang, S. V. Morozov, H. L. Stormer, U. Zeitler, J. C. Maan, G. S. Boebinger, P. Kim, and A. K. Geim. Room-temperature quantum hall effect in graphene. *Science*, 315(5817):1379+, March 2007.

[11] Yuanbo Zhang, Yan-Wen Tan, Horst L. Stormer, and Philip Kim. Experimental observation of the quantum hall effect and berry's phase in graphene. *Nature*, 438(7065):201–204, November 2005.

[12] K. S. Novoselov, E. McCann, S. V. Morozov, V. I. Fal/'ko, M. I. Katsnelson, U. Zeitler, D. Jiang, F. Schedin, and A. K. Geim. Unconventional quantum hall effect and berry's phase of 2p in bilayer graphene. *Nature Physics*, 2(3):177–180, February 2006.

[13] K.I. Bolotin, K.J. Sikes, Z. Jiang, M. Klima, G. Fudenberg, J. Hone, P. Kim, and H.L. Stormer. Ultrahigh electron mobility in suspended graphene. *Solid State Communications*, 146(9-10):351 – 355, 2008.

[14] K. S. Novoselov, A. K. Geim, S. V. Morozov, D. Jiang, M. I. Katsnelson, I. V. Grigorieva, S. V. Dubonos, and A. A. Firsov. Two-dimensional gas of massless dirac fermions in graphene. *Nature*, 438(7065):197–200, November 2005.

[15] S. V. Morozov, K. S. Novoselov, M. I. Katsnelson, F. Schedin, D. C. Elias, J. A. Jaszczak, and A. K. Geim. Giant intrinsic carrier mobilities in graphene and its bilayer. *Phys. Rev. Lett.*, 100(1):016602, Jan 2008.

[16] F. Schedin, A. K. Geim, S. V. Morozov, E. W. Hill, P. Blake, M. I. Katsnelson, and K. S. Novoselov. Detection of individual gas molecules adsorbed on graphene. *Nature Materials*, 6(9):652–655, July 2007.

[17] PR Wallace. The Band Theory of Graphite. *Physical Review*, 71(9):622–634, 1947.

[18] Riichiro Saito, Gene Dresselhaus, and Mildred S Dresselhaus. *Physical Properties of Carbon Nanotubes.* World Scientific Publishing, 1998. ISBN 978-1-86094-093-4 (hb) ISBN 978-1-86094-223-5 (pb).

[19] Gordon W. Semenoff. Condensed-matter simulation of a three-dimensional anomaly. *Phys. Rev. Lett.*, 53(26):2449–2452, Dec 1984.

[20] K S Novoselov, A K Geim, S V Morozov, D Jiang, M I Katsnelson, I V Grigorieva, S V Dubonos, and A A Firsov. Two-dimensional gas of massless dirac fermions in graphene. *Nature*, 438(7065):197–200, 2005.

[21] YB Zhang, YW Tan, HL Stormer, and P Kim. Experimental observation of the quantum Hall effect and Berry's phase in graphene. *Nature*, 438(7065):201–204, NOV 10 2005.

[22] K. S. Novoselov, Z. Jiang, Y. Zhang, S. V. Morozov, H. L. Stormer, U. Zeitler, J. C. Maan, G. S. Boebinger, P. Kim, and A. K. Geim. Room-temperature quantum hall effect in graphene. *SCIENCE*, 315(5817):1379, MAR 9 2007.

[23] Xu Du, Ivan Skachko, Anthony Barker, and Eva Y Andrei. Approaching ballistic transport in suspended graphene. *Nature Nanotechnology*, 3(8):491–495, 2008.

[24] Xiaogan Liang, Zengli Fu, and Stephen Y. Chou. Graphene transistors fabricated via transfer-printing in device active-areas on large wafer. *Nano Letters*, 7(12):3840–3844, 2007.

[25] Li Song, Lijie Ci, Wei Gao, and Pulickel M. Ajayan. Transfer printing of graphene using gold film. *ACS Nano*, 3(6):1353–1356, 2009. PMID: 19438194.

[26] Crombeen J.E. Van Tooren A. Van Bommel, A.J. Leed and auger electron observations of the sic(0001) surface. *Surface Science*, 48(2):463–472, 1975. cited By (since 1996) 211.

[27] Mrtensson P. Owman, F. The sic(0001)6v3 6v3 reconstruction studied with stm and leed. *Surface Science*, 369(1-3):126–136, 1996. cited By (since 1996) 54.

[28] Walt A. de Heer, Claire Berger, Xiaosong Wu, Phillip N. First, Edward H. Conrad, Xuebin Li, Tianbo Li, Michael Sprinkle, Joanna Hass, Marcin L. Sadowski, Marek Potemski, and Grard Martinez. Epitaxial graphene. *Solid State Communications*, 143(1-2):92 – 100, 2007. Exploring graphene - Recent research advances.

[29] Claire Berger, Zhimin Song, Xuebin Li, Xiaosong Wu, Nate Brown, Ccile Naud, Didier Mayou, Tianbo Li, Joanna Hass, Alexei N. Marchenkov, Edward H. Conrad, Phillip N. First, and Walt A. de Heer. Electronic Confinement and Coherence in Patterned Epitaxial Graphene. *Science*, 312(5777):1191–1196, 2006.

[30] Konstantin V. Emtsev, Aaron Bostwick, Karsten Horn, Johannes Jobst, Gary L. Kellogg, Lothar Ley, Jessica L. McChesney, Taisuke Ohta, Sergey A. Reshanov, Jonas Roehrl, Eli Rotenberg, Andreas K. Schmid, Daniel Waldmann, Heiko B. Weber, and Thomas Seyller. Towards wafer-size graphene layers by atmospheric pressure graphitization of silicon carbide. *Nature Materials*, 8(3):203–207, MAR 2009.

[31] A. Al-Temimy, C. Riedl, and U. Starke. Low temperature growth of epitaxial graphene on sic induced by carbon evaporation. *Applied Physics Letters*, 95(23):231907, 2009.

[32] G. M. Rutter, N. P. Guisinger, J. N. Crain, E. A. A. Jarvis, M. D. Stiles, T. Li, P. N. First, and J. A. Stroscio. Imaging the interface of epitaxial graphene with silicon carbide via scanning tunneling microscopy. *Phys. Rev. B*, 76(23):235416, Dec 2007.

[33] J. B. Hannon and R. M. Tromp. Pit formation during graphene synthesis on sic(0001): In situ electron microscopy. *Phys. Rev. B*, 77(24):241404, Jun 2008.

[34] K. V. Emtsev, F. Speck, Th. Seyller, L. Ley, and J. D. Riley. Interaction, growth, and ordering of epitaxial graphene on sic0001 surfaces: A comparative photoelectron spectroscopy study. *Phys. Rev. B*, 77(15):155303, Apr 2008.

[35] J. Hass, J. E. Millán-Otoya, P. N. First, and E. H. Conrad. Interface structure of epitaxial graphene grown on 4h-sic(0001). *Phys. Rev. B*, 78(20):205424, Nov 2008.

[36] J. Hass, R. Feng, J. E. Millán-Otoya, X. Li, M. Sprinkle, P. N. First, W. A. de Heer, E. H. Conrad, and C. Berger. Structural properties of the multilayer graphene/ 4h-sic($000\overline{1}$) system as determined by surface x-ray diffraction. *Phys. Rev. B*, 75(21):214109, Jun 2007.

[37] Taisuke Ohta, Aaron Bostwick, J. L. McChesney, Thomas Seyller, Karsten Horn, and Eli Rotenberg. Interlayer interaction and electronic screening in multilayer graphene investigated with angle-resolved photoemission spectroscopy. *Phys. Rev. Lett.*, 98(20):206802, May 2007.

[38] P. Mallet, F. Varchon, C. Naud, L. Magaud, C. Berger, and J.-Y. Veuillen. Electron states of mono- and bilayer graphene on sic probed by scanning-tunneling microscopy. *Phys. Rev. B*, 76(4):041403, Jul 2007.

[39] C. Riedl, U. Starke, J. Bernhardt, M. Franke, and K. Heinz. Structural properties of the graphene-sic(0001) interface as a key for the preparation of homogeneous large-terrace graphene surfaces. *Phys. Rev. B*, 76(24):245406, Dec 2007.

[40] M. Sprinkle, D. Siegel, Y. Hu, J. Hicks, A. Tejeda, A. Taleb-Ibrahimi, P. Le Fèvre, F. Bertran, S. Vizzini, H. Enriquez, S. Chiang, P. Soukiassian, C. Berger, W. A. de Heer, A. Lanzara, and E. H. Conrad. First direct observation of a nearly ideal graphene band structure. *Phys. Rev. Lett.*, 103(22):226803, Nov 2009.

[41] Jing Kong, Alan M. Cassell, and Hongjie Dai. Chemical vapor deposition of methane for single-walled carbon nanotubes. *Chemical Physics Letters*, 292(4-6):567 – 574, 1998.

[42] J Kong, HT Soh, AM Cassell, CF Quate, and HJ Dai. Synthesis of individual single-walled carbon nanotubes on patterned silicon wafers. *Nature*, 395(6705):878–881, OCT 29 1998.

[43] Alpha T N'Diaye, Johann Coraux, Tim N Plasa, Carsten Busse, and Thomas Michely. Structure of epitaxial graphene on ir(111). *New Journal of Physics*, 10(4):043033, 2008.

[44] Peter W. Sutter, Jan-Ingo Flege, and Eli A. Sutter. Epitaxial graphene on ruthenium. *Nature Materials*, 7(5):406–411, MAY 2008.

[45] Keun Soo Kim, Yue Zhao, Houk Jang, Sang Yoon Lee, Jong Min Kim, Kwang S. Kim, Jong-Hyun Ahn, Philip Kim, Jae-Young Choi, and Byung Hee Hong. Large-scale pattern growth of graphene films for stretchable transparent electrodes. *Nature*, 457(7230):706 – 710, 2009.

[46] A.N. Obraztsov, E.A. Obraztsova, A.V. Tyurnina, and A.A. Zolotukhin. Chemical vapor deposition of thin graphite films of nanometer thickness. *Carbon*, 45(10):2017 – 2021, 2007.

[47] Alfonso Reina, Xiaoting Jia, John Ho, Daniel Nezich, Hyungbin Son, Vladimir Bulovic, Mildred S. Dresselhaus, and Jing Kong. Large area, few-layer graphene films on arbitrary substrates by chemical vapor deposition. *Nano Letters*, 9(1):30–35, 2009.

[48] Xuesong Li, Weiwei Cai, Jinho An, Seyoung Kim, Junghyo Nah, Dongxing Yang, Richard Piner, Aruna Velamakanni, Inhwa Jung, Emanuel Tutuc, Sanjay K. Banerjee, Luigi Colombo, and Rodney S. Ruoff. Large-Area Synthesis of High-Quality and Uniform Graphene Films on Copper Foils. *Science*, 324(5932):1312–1314, 2009.

[49] Sukang Bae, Hyeongkeun Kim, Youngbin Lee, Xiangfan Xu, Jae-Sung Park, Yi Zheng, Jayakumar Balakrishnan, Tian Lei, Hye Ri Kim, Young Il Song, Young-Jin Kim, Kwang S. Kim, Barbaros Ozyilmaz,

Jong-Hyun Ahn, Byung Hee Hong, and Sumio Iijima. Roll-to-roll production of 30-inch graphene films for transparent electrodes. *Nature Nanotechnology*, 5(8):574–578, AUG 2010.

[50] Dacheng Wei, Yunqi Liu, Yu Wang, Hongliang Zhang, Liping Huang, and Gui Yu. Synthesis of n-doped graphene by chemical vapor deposition and its electrical properties. *Nano Letters*, 9(5):1752–1758, 2009. PMID: 19326921.

[51] Mark P. Levendorf, Carlos S. Ruiz-Vargas, Shivank Garg, and Jiwoong Park. Transfer-free batch fabrication of single layer graphene transistors. *Nano Letters*, 9(12):4479–4483, 2009. PMID: 19860406.

[52] Anchal Srivastava, Charudatta Galande, Lijie Ci, Li Song, Chaitra Rai, Deep Jariwala, Kevin F. Kelly, and Pulickel M. Ajayan. Novel liquid precursor-based facile synthesis of large-area continuous, single, and few-layer graphene films. *Chemistry of Materials*, 22(11):3457–3461, 2010.

[53] Zhengzong Sun, Zheng Yan, Jun Yao, Elvira Beitler, Yu Zhu, and James M. Tour. Growth of graphene from solid carbon sources. *Nature*, 468(7323):549–552, NOV 25 2010.

[54] Xiaolin Li, Guangyu Zhang, Xuedong Bai, Xiaoming Sun, Xinran Wang, Enge Wang, and Hongjie Dai. Highly conducting graphene sheets and Langmuir-Blodgett films. *Nature Nanotechnology*, 3(9):538–542, SEP 2008.

[55] Yenny Hernandez, Valeria Nicolosi, Mustafa Lotya, Fiona M. Blighe, Zhenyu Sun, Sukanta De, I. T. McGovern, Brendan Holland, Michele Byrne, Yurii K. Gun'ko, John J. Boland, Peter Niraj, Georg Duesberg, Satheesh Krishnamurthy, Robbie Goodhue, John Hutchison, Vittorio Scardaci, Andrea C. Ferrari, and Jonathan N. Coleman. High-yield production of graphene by liquid-phase exfoliation of graphite. *Nature Nanotechnolgy*, 3(9):563–568, SEP 2008.

[56] Cristina *Vallés*, Carlos Drummond, Hassan Saadaoui, Clascidia A. Furtado, Maoshuai He, Olivier Roubeau, Luca Ortolani, Marc Monthioux, and Alain Penicaud. Solutions of negatively charged graphene sheets and ribbons. *Journal of the American Chemical Society*, 130(47):15802–15804, 2008.

[57] Xiaolin Li, Xinran Wang, Li Zhang, Sangwon Lee, and Hongjie Dai. Chemically Derived, Ultrasmooth Graphene Nanoribbon Semiconductors. *Science*, 319(5867):1229–1232, 2008.

[58] Zhuang Liu, Joshua T. Robinson, Xiaoming Sun, and Hongjie Dai. Pegylated nanographene oxide for delivery of water-insoluble cancer drugs. *Journal of the American Chemical Society*, 130(33):10876–10877, 2008. PMID: 18661992.

[59] Na Liu, Fang Luo, Haoxi Wu, Yinghui Liu, Chao Zhang, and Ji Chen. One-step ionic-liquid-assisted electrochemical synthesis of ionic-liquid-functionalized graphene sheets directly from graphite. *ADVANCED FUNCTIONAL MATERIALS*, 18(10):1518–1525, MAY 23 2008.

[60] Rui Hao, Wen Qian, Luhui Zhang, and Yanglong Hou. Aqueous dispersions of tcnq-anion-stabilized graphene sheets. *Chem. Commun.*, pages 6576–6578, 2008.

[61] B.C. Brodie. Sur le poids atomique du graphite. *Ann. Chim. Phys.*, 59:466, 1860.

[62] WS Hummers and RE Offeman. Preaparation Of Graphitic Oxide. *Journal Of The American Chemical Society*, 80(6):1339, 1958.

[63] L. Staudenmaier. Verfahren zur darstellung der graphitsäure. *Berichte der deutschen chemischen Gesellschaft*, 31(2):1481–1487, 1898.

[64] R. Hoffman, U.and Holst. ber die formel der graphitsure. *Ber. Dtch. Chem. Ges.*, 72:754, 1939.

[65] G. Ruess. ber das graphitoxyhydroxyd (graphitoxyd). *Monatshefte fr Chemie / Chemical Monthly*, 76:381–417, 1947. 10.1007/BF00898987.

[66] Alexander Clause, Reinhold Plass, H.-P Boehm, and Ulrich Hofmann. Untersuchungen zur struktur des graphitoxyds. *Zeitschrift fr anorganische und allgemeine Chemie*, 291:205–220, 1957.

[67] W. Scholz and H. P. Boehm. Untersuchungen am graphitoxid. vi. betrachtungen zur struktur des graphitoxids. *Zeitschrift fr anorganische und allgemeine Chemie*, 369(3-6):327–340, 1969.

[68] T Nakajima and Y Matsuo. Formation Process and Structure of Graphite Oxide. *Carbon*, 32(3):469–475, 1994.

[69] Anton Lerf, Heyong He, Michael Forster, and Jacek Klinowski. Structure of graphite oxide revisited? *The Journal of Physical Chemistry B*, 102(23):4477–4482, 1998.

[70] Tamás Szabó, Ottó Berkesi, Péter Forgó, Katalin Josepovits, Yiannis Sanakis, Dimitris Petridis, and Imre Dékány. Evolution of surface functional groups in a series of progressively oxidized graphite oxides. *Chemistry of Materials*, 18(11):2740–2749, 2006.

[71] Weiwei Cai, Richard D. Piner, Frank J. Stadermann, Sungjin Park, Medhat A. Shaibat, Yoshitaka Ishii, Dongxing Yang, Aruna Velamakanni, Sung Jin An, Meryl Stoller, Jinho An, Dongmin Chen, and Rodney S. Ruoff. Synthesis and Solid-State NMR Structural Characterization of 13C-Labeled Graphite Oxide. *Science*, 321(5897):1815–1817, 2008.

[72] Cristina Gómez-Navarro, R. Thomas Weitz, Alexander M. Bittner, Matteo Scolari, Alf Mews, Marko Burghard, and Klaus Kern. Electronic transport properties of individual chemically reduced graphene oxide sheets. *Nano Letters*, 7(11):3499–3503, 2007. PMID: 17944526.

[73] Scott Gilje, Song Han, Minsheng Wang, Kang L. Wang, and Richard B. Kaner. A chemical route to graphene for device applications. *Nano Letters*, 7(11):3394–3398, 2007.

[74] Dmitriy A Dikin, Sasha Stankovich, Eric J Zimney, Richard D Piner, Geoffrey H B Dommett, Guennadi Evmenenko, Sonbinh T Nguyen, and Rodney S Ruoff. Preparation and characterization of graphene oxide paper. *Nature*, 448(7152):457–460, 2007.

[75] Cristina Gómez-Navarro, Marko Burghard, and Klaus Kern. Elastic properties of chemically derived single graphene sheets. *Nano Letters*, 8(7):2045–2049, 2008. PMID: 18540659.

[76] Arndt Simon, Richard Dronskowski, Bernt Krebs, and Bernhard Hettich. The crystal structure of mn2o7. *Angewandte Chemie International Edition in English*, 26(2):139–140, 1987.

[77] Klaus R. Koch. Oxidation by mn207: An impressive demonstration of the powerful oxidizing property of dimanganeseheptoxide. *Journal of Chemical Education*, 59(11):973, 1982.

[78] Hannes C. Schniepp, Je-Luen Li, Michael J. McAllister, Hiroaki Sai, Margarita Herrera-Alonso, Douglas H. Adamson, Robert K.

Prud'homme, Roberto Car, Dudley A. Saville, and Ilhan A. Aksay. Functionalized single graphene sheets derived from splitting graphite oxide. *The Journal of Physical Chemistry B*, 110(17):8535–8539, 2006.

[79] Sasha Stankovich, Richard D. Piner, Xinqi Chen, Nianqiang Wu, SonBinh T. Nguyen, and Rodney S. Ruoff. Stable aqueous dispersions of graphitic nanoplatelets via the reduction of exfoliated graphite oxide in the presence of poly(sodium 4-styrenesulfonate). *J. Mater. Chem.*, 16:155–158, 2006.

[80] Sasha Stankovich, Dmitriy A. Dikin, Richard D. Piner, Kevin A. Kohlhaas, Alfred Kleinhammes, Yuanyuan Jia, Yue Wu, SonBinh T. Nguyen, and Rodney S. Ruoff. Synthesis of graphene-based nanosheets via chemical reduction of exfoliated graphite oxide. *Carbon*, 45(7):1558 – 1565, 2007.

[81] Hyeon-Jin Shin, Ki Kang Kim, Anass Benayad, Seon-Mi Yoon, Hyeon Ki Park, In-Sun Jung, Mei Hua Jin, Hae-Kyung Jeong, Jong Min Kim, Jae-Young Choi, and Young Hee Lee. Efficient reduction of graphite oxide by sodium borohydride and its effect on electrical conductance. *Advanced Functional Materials*, 19(12):1987–1992, 2009.

[82] Guoxiu Wang, Juan Yang, Jinsoo Park, Xinglong Gou, Bei Wang, Hao Liu, and Jane Yao. Facile synthesis and characterization of graphene nanosheets. *The Journal of Physical Chemistry C*, 112(22):8192–8195, 2008.

[83] Zhong-Shuai Wu, Wencai Ren, Libo Gao, Bilu Liu, Chuanbin Jiang, and Hui-Ming Cheng. Synthesis of high-quality graphene with a predetermined number of layers. *Carbon*, 47(2):493 – 499, 2009.

[84] M. J. Fernandez-Merino, L. Guardia, J. I. Paredes, S. Villar-Rodil, P. Solis-Fernandez, A. Martinez-Alonso, and J. M. D. Tascon. Vitamin c is an ideal substitute for hydrazine in the reduction of graphene oxide suspensions. *The Journal of Physical Chemistry C*, 114(14):6426–6432, 2010.

[85] Xiaobin Fan, Wenchao Peng, Yang Li, Xianyu Li, Shulan Wang, Guoliang Zhang, and Fengbao Zhang. Deoxygenation of exfoliated graphite oxide under alkaline conditions: A green route to graphene preparation. *Advanced Materials*, 20(23):4490–4493, 2008.

[86] Inhwa Jung, Dmitriy A. Dikin, Richard D. Piner, and Rodney S. Ruoff. Tunable electrical conductivity of individual graphene oxide sheets reduced at low temperatures. *Nano Letters*, 8(12):4283–4287, 2008.

[87] CV Raman. A change of wave-length in light scattering. *Nature*, 121:619, JAN-JUN 1928.

[88] CV Raman and KS Krishnan. A new type of secondary radiation. *Nature*, 121:501–502, JAN-JUN 1928.

[89] AC Ferrari and J Robertson. Raman spectroscopy in carbons: from nanotubes to diamond. *Philosophican Transactions of the Royal Society of London Series A-Mathematica Physical and Engineering Sciences*, 362(1824):2269–2270, NOV 15 2004.

[90] F. Tuinstra and J. L. Koenig. Raman spectrum of graphite. *The Journal of Chemical Physics*, 53(3):1126–1130, 1970.

[91] R. J. Nemanich and S. A. Solin. First- and second-order raman scattering from finite-size crystals of graphite. *Phys. Rev. B*, 20(2):392–401, Jul 1979.

[92] A. C. Ferrari, J. C. Meyer, V. Scardaci, C. Casiraghi, M. Lazzeri, F. Mauri, S. Piscanec, D. Jiang, K. S. Novoselov, S. Roth, and A. K. Geim. Raman spectrum of graphene and graphene layers. *Phys. Rev. Lett.*, 97(18):187401, Oct 2006.

[93] O. Scherzer. The theoretical resolution limit of the electron microscope. *Journal of Applied Physics*, 20(1):20–29, 1949.

[94] Hoschen R. Osaki M. Mobus G. Ruhle M. Phillipp, F. New high-voltage atomic resolution microscope approaching 1 point resolution installed in stuttgart. *Ultramicroscopy*, 56(1-3):1–10, 1994. cited By (since 1996) 116.

[95] O. Scherzer. ber einige fehler von elektronenlinsen. *Zeitschrift fr Physik*, 101(9-10):593–603, 1936. cited By (since 1996) 129.

[96] Jannik C. Meyer, A. K. Geim, M. I. Katsnelson, K. S. Novoselov, T. J. Booth, and S. Roth. The structure of suspended graphene sheets. *Nature*, 446(7131):60–63, MAR 1 2007.

[97] Joachim Stöhr. Nexafs spectroscopy. *Springer Berlin*, 1992.

[98] J.L. Solomon, R.J. Madix, and J. Sthr. Orientation and absolute coverage of benzene, aniline, and phenol on ag(110) determined by nexafs and xps. *Surface Science*, 255(1-2):12 – 30, 1991.

[99] S Rosenblatt, Y Yaish, J Park, J Gore, V Sazonova, and PL McEuen. High performance electrolyte gated carbon nanotube transistors. *Nanoletters*, 2(8):869–872, AUG 2002.

[100] M Kruger, MR Buitelaar, T Nussbaumer, C Schonenberger, and L Forro. Electrochemical carbon nanotube field-effect transistor. *Applied Physics Letters*, 78(9):1291–1293, FEB 26 2001.

[101] A. Das, S. Pisana, B. Chakraborty, S. Piscanec, S. K. Saha, U. V. Waghmare, K. S. Novoselov, H. R. Krishnamurthy, A. K. Geim, A. C. Ferrari, and A. K. Sood. Monitoring dopants by Raman scattering in an electrochemically top-gated graphene transistor. *Nature Nanotechnology*, 3(4):210–215, APR 2008.

[102] Adarsh Sagar, Eduardo J. H. Lee, Kannan Balasubramanian, Marko Burghard, and Klaus Kern. Effect of stacking order on the electric-field induced carrier modulation in graphene bilayers. *Nano Letters*, 9(9):3124–3128, 2009. PMID: 19645421.

[103] Eduardo J. H. Lee, Kannan Balasubramanian, Ralf Thomas Weitz, Marko Burghard, and Klaus Kern. Contact and edge effects in graphene devices. *Nature Nanotechnology*, 3(8):486–490, AUG 2008.

[104] C. Casiraghi, A. Hartschuh, E. Lidorikis, H. Qian, H. Harutyunyan, T. Gokus, K. S. Novoselov, and A. C. Ferrari. Rayleigh imaging of graphene and graphene layers. *Nano Letters*, 7(9):2711–2717, 2007.

[105] Jacques Lefebvre, David G. Austing, Jeffery Bond, and Paul Finnie. Photoluminescence imaging of suspended single-walled carbon nanotubes. *Nano Letters*, 6(8):1603–1608, 2006.

[106] D. Graf, F. Molitor, K. Ensslin, C. Stampfer, A. Jungen, C. Hierold, and L. Wirtz. Raman imaging of graphene. *Solid State Communications*, 143(1-2):44 – 46, 2007. Exploring graphene - Recent research advances.

[107] B. Krauss, T. Lohmann, D.-H. Chae, M. Haluska, K. von Klitzing, and J. H. Smet. Laser-induced disassembly of a graphene single crystal into a nanocrystalline network. *Phys. Rev. B*, 79(16):165428, Apr 2009.

[108] Kannan Balasubramanian, Marko Burghard, Klaus Kern, Matteo Scolari, and Alf Mews. Photocurrent imaging of charge transport barriers in carbon nanotube devices. *Nano Letters*, 5(3):507–510, 2005.

[109] M. Freitag, Y. Martin, J. A. Misewich, R. Martel, and Ph. Avouris. Photoconductivity of single carbon nanotubes. *Nano Letters*, 3(8):1067–1071, 2003.

[110] Xiaodong Xu, Nathaniel M. Gabor, Jonathan S. Alden, Arend M. van der Zande, and Paul L. McEuen. Photo-thermoelectric effect at a graphene interface junction. *Nano Letters*, 10(2):562–566, 2010. PMID: 20038087.

[111] A. C. Ferrari and J. Robertson. Interpretation of raman spectra of disordered and amorphous carbon. *Phys. Rev. B*, 61(20):14095–14107, May 2000.

[112] Konstantin N. Kudin, Bulent Ozbas, Hannes C. Schniepp, Robert K. Prud'homme, Ilhan A. Aksay, and Roberto Car. Raman spectra of graphite oxide and functionalized graphene sheets. *Nano Letters*, 8(1):36–41, 2008. PMID: 18154315.

[113] F. Tuinstra and J. L. Koenig. Raman spectrum of graphite. *The Journal of Chemical Physics*, 53(3):1126–1130, 1970.

[114] Jannik C. Meyer, C. O. Girit, M. F. Crommie, and A. Zettl. Imaging and dynamics of light atoms and molecules on graphene. *Nature*, 454(7202):319–322, JUL 17 2008.

[115] Mhairi H. Gass, Ursel Bangert, Andrew L. Bleloch, Peng Wang, Rahul R. Nair, and A. K. Geim. Free-standing graphene at atomic resolution. *Nature Nanotechnology*, 3(11):676–681, NOV 2008.

[116] D. Pacilé, M. Papagno, A. Fraile Rodríguez, M. Grioni, L. Papagno, Ç. Ö. Girit, J. C. Meyer, G. E. Begtrup, and A. Zettl. Near-edge x-ray absorption fine-structure investigation of graphene. *Phys. Rev. Lett.*, 101(6):066806, Aug 2008.

[117] M. Papagno, A. Fraile Rodrguez, .. Girit, J.C. Meyer, A. Zettl, and D. Pacil. Polarization-dependent c k near-edge x-ray absorption fine-structure of graphene. *Chemical Physics Letters*, 475(4-6):269 – 271, 2009.

[118] M Mermoux, Y Chabre, and A Rousseau. Ftir and 13c nmr study of graphite oxide. *Carbon*, 29(3):469 – 474, 1991.

[119] P. A. Brühwiler, A. J. Maxwell, C. Puglia, A. Nilsson, S. Andersson, and N. Mårtensson. π^* and σ^* excitons in c 1s absorption of graphite. *Phys. Rev. Lett.*, 74(4):614–617, Jan 1995.

[120] J. T. Francis and A. P. Hitchcock. Inner-shell spectroscopy of p-benzoquinone, hydroquinone, and phenol: distinguishing quinoid and benzenoid structures. *The Journal of Physical Chemistry*, 96(16):6598–6610, 1992.

[121] Vincent Lee, Luisa Whittaker, Cherno Jaye, Kristen M. Baroudi, Daniel A. Fischer, and Sarbajit Banerjee. Large-area chemically modified graphene films: Electrophoretic deposition and characterization by soft x-ray absorption spectroscopy. *Chemistry of Materials*, 21(16):3905–3916, 2009.

[122] H. K. Jeong, H. J. Noh, J. Y. Kim, M. H. Jin, C. Y. Park, and Y. H. Lee. X-ray absorption spectroscopy of graphite oxide. *EPL*, 82(6), JUN 2008.

[123] D. Pandey, R. Reifenberger, and R. Piner. Scanning probe microscopy study of exfoliated oxidized graphene sheets. *Surface Science*, 602(9):1607 – 1613, 2008.

[124] Stephen J. Sque, Robert Jones, and Patrick R. Briddon. The transfer doping of graphite and graphene. *physica status solidi (a)*, 204(9):3078–3084, 2007.

[125] Mark D. Ellison, Adam P. Good, Carrie S. Kinnaman, and Nicholas E. Padgett. Interaction of water with single-walled carbon nanotubes:? reaction and adsorption. *The Journal of Physical Chemistry B*, 109(21):10640–10646, 2005. PMID: 16852291.

[126] N. F. Mott and E. A. Davis. *Electronic processes in non-crystalline materials / by N.F. Mott and E.A. Davis.* Clarendon Press ; Oxford University Press, Oxford : New York :, 2nd ed. edition, 1979.

[127] K. I. Bolotin, K. J. Sikes, J. Hone, H. L. Stormer, and P. Kim. Temperature-dependent transport in suspended graphene. *Phys. Rev. Lett.*, 101(9):096802, Aug 2008.

[128] B. Huard, N. Stander, J. A. Sulpizio, and D. Goldhaber-Gordon. Evidence of the role of contacts on the observed electron-hole asymmetry in graphene. *Phys. Rev. B*, 78(12):121402, Sep 2008.

[129] Damon B. Farmer, Roksana Golizadeh-Mojarad, Vasili Perebeinos, Yu-Ming Lin, George S. Tulevski, James C. Tsang, and Phaedon Avouris. Chemical doping and electron-hole conduction asymmetry in graphene devices. *Nano Letters*, 9(1):388–392, 2009.

[130] D. S. Novikov. Numbers of donors and acceptors from transport measurements in graphene. *Applied Physics Letters*, 91(10):102102, 2007.

[131] J. H. Chen, C. Jang, S. Adam, M. S. Fuhrer, E. D. Williams, and M. Ishigami. Charged-impurity scattering in graphene. *Nature Physics*, 4(5):377–381, MAY 2008.

[132] Zhihong Chen, Joerg Appenzeller, Joachim Knoch, Yu-ming Lin, and Phaedon Avouris. The role of metal-nanotube contact in the performance of carbon nanotube field-effect transistors. *Nano Letters*, 5(7):1497–1502, 2005. PMID: 16178264.

[133] A Javey, J Guo, Q Wang, M Lundstrom, and HJ Dai. Ballistic carbon nanotube field-effect transistors. *Nature*, 424(6949):654–657, AUG 7 2003.

[134] S. Sahoo, T. Kontos, C. Schonenberger, and C. Surgers. Electrical spin injection in multiwall carbon nanotubes with transparent ferromagnetic contacts. *Applied Physics Letters*, 86(11):112109, 2005.

[135] G. Giovannetti, P. A. Khomyakov, G. Brocks, V. M. Karpan, J. van den Brink, and P. J. Kelly. Doping graphene with metal contacts. *Phys. Rev. Lett.*, 101(2):026803, Jul 2008.

[136] Ercag Pince and Coskun Kocabas. Investigation of high frequency performance limit of graphene field effect transistors. *Applied Physics Letters*, 97(17):173106, 2010.

[137] Damon B. Farmer, Hsin-Ying Chiu, Yu-Ming Lin, Keith A. Jenkins, Fengnian Xia, and Phaedon Avouris. Utilization of a buffered dielectric to achieve high field-effect carrier mobility in graphene transistors. *Nano Letters*, 9(12):4474–4478, 2009. PMID: 19883119.

[138] J. Martin, N. Akerman, G. Ulbricht, T. Lohmann, J. H. Smet, K. Von Klitzing, and A. Yacoby. Observation of electron-hole puddles in graphene using a scanning single-electron transistor. *Nature Physics*, 4(2):144–148, FEB 2008.

[139] Fengnian Xia, Thomas Mueller, Roksana Golizadeh-Mojarad, Marcus Freitag, Yu-ming Lin, James Tsang, Vasili Perebeinos, and Phaedon Avouris. Photocurrent imaging and efficient photon detection in a graphene transistor. *Nano Letters*, 9(3):1039–1044, 2009.

[140] S. Piscanec, M. Lazzeri, Francesco Mauri, A. C. Ferrari, and J. Robertson. Kohn anomalies and electron-phonon interactions in graphite. *Phys. Rev. Lett.*, 93(18):185503, Oct 2004.

[141] Simone Pisana, Michele Lazzeri, Cinzia Casiraghi, Kostya S. Novoselov, A. K. Geim, Andrea C. Ferrari, and Francesco Mauri. Breakdown of the adiabatic Born-Oppenheimer approximation in graphene. *Nature Materials*, 6(3):198–201, MAR 2007.

[142] Jun Yan, Yuanbo Zhang, Philip Kim, and Aron Pinczuk. Electric field effect tuning of electron-phonon coupling in graphene. *Phys. Rev. Lett.*, 98(16):166802, Apr 2007.

[143] Y.-W. Tan, Y. Zhang, H. L. Stormer, and P. Kim. Temperature dependent electron transport in graphene. *The European Physical Journal - Special Topics*, 148:15–18, 2007. 10.1140/epjst/e2007-00221-9.

[144] I. Calizo, F. Miao, W. Bao, C. N. Lau, and A. A. Balandin. Variable temperature raman microscopy as a nanometrology tool for graphene layers and graphene-based devices. *Applied Physics Letters*, 91(7):071913, 2007.

[145] B. Gao, Y. F. Chen, M. S. Fuhrer, D. C. Glattli, and A. Bachtold. Four-point resistance of individual single-wall carbon nanotubes. *Phys. Rev. Lett.*, 95(19):196802, Oct 2005.

[146] Joshua A. Robinson, Michael LaBella, Mike Zhu, Matt Hollander, Richard Kasarda, Zachary Hughes, Kathleen Trumbull, Randal Cavalero, and David Snyder. Contacting graphene. *Applied Physics Letters*, 98(5):053103, 2011.

[147] Isabella Gierz, Christian Riedl, Ulrich Starke, Christian R. Ast, and Klaus Kern. Atomic hole doping of graphene. *Nano Letters*, 8(12):4603–4607, 2008.

[148] M. M. Fogler, D. S. Novikov, L. I. Glazman, and B. I. Shklovskii. Effect of disorder on a graphene $p-n$ junction. *Phys. Rev. B*, 77(7):075420, Feb 2008.

[149] J Kong, HT Soh, AM Cassell, CF Quate, and HJ Dai. Synthesis of individual single-walled carbon nanotubes on patterned silicon wafers. *Nature*, 395(6705):878–881, OCT 29 1998.

[150] Vincent C. Tung, Matthew J. Allen, Yang Yang, and Richard B. Kaner. High-throughput solution processing of large-scale graphene. *Nat Nano*, advanced online publication, November 2008.

[151] Zhengtang Luo, Patrick M. Vora, Eugene J. Mele, A. T. Charlie Johnson, and James M. Kikkawa. Photoluminescence and band gap modulation in graphene oxide. *Applied Physics Letters*, 94(11):111909, 2009.

[152] T. Gokus, R. R. Nair, A. Bonetti, M. Bohmler, A. Lombardo, K. S. Novoselov, A. K. Geim, A. C. Ferrari, and A. Hartschuh. Making graphene luminescent by oxygen plasma treatment. *ACS Nano*, 3(12):3963–3968, 2009. PMID: 19925014.

[153] Marcel J. Fischer. Amine coupling through edc/nhs: A practical approach. 627, May 2010.

[154] J. Maultzsch, S. Reich, C. Thomsen, H. Requardt, and P. Ordejón. Phonon dispersion in graphite. *Phys. Rev. Lett.*, 92(7):075501, Feb 2004.

Publications

- Ravi S. Sundaram*, Mathias Steiner*, Hsin-Ying Chiu, Michael Engel, Ageeth A. Bol, Ralph Krupke, Marko Burghard, Klaus Kern, and Phaedon Avouris, *"The graphene-gold contact and its implications for nano-electronics"*. Manuscript under review.

- Gayathri Rao, Marcus Freitag, Hsin-Ying Chiu, Ravi S. Sundaram, and Phaedon Avouris, *"Raman and photocurrent imaging of electrical stress induced p-n junctions in graphene"*. Manuscript under review.

- D. Pacilé, J. C. Meyer, A. Fraile Rodríguez, M. Papagno, C. Gómez-Navarro, R. S. Sundaram, M. Burghard, K. Kern, C. Carbone, and U. Kaiser, *"Electronic properties and atomic structure of graphene oxide membranes"*. Carbon,49,966-972(2011).

- Cristina Gómez-Navarro, Jannik C. Meyer, Ravi S. Sundaram, Andrey Chuvilin, Simon Kurasch, Marko Burghard, Klaus Kern, and Ute Kaiser, *"Atomic Structure of Reduced Graphene Oxide"*. Nano Lett., 2010, 10 (4), pp 1144-1148.

- Ravi S. Sundaram, Cristina Gómez-Navarro, Eduardo J.H. Lee, Marko Burghard and Klaus Kern, *"Non-invasive metal contacts in chemically derived graphene devices"*Appl. Phys. Lett. 95, 223507 (2009).

- Vicente Lopez*, Ravi S. Sundaram*, Cristina Gómez-Navarro, David Olea, Marko Burghard, Julio Gomez-Herrero, Felix Zamora and Klaus Kern, *"Chemical Vapor Deposition Repair of Graphene Oxide: A Route to Highly-Conductive Graphene Monolayers"*Adv. Mater. 2009,21,1-4.

- Alan B. Kaiser, Cristina Gómez-Navarro, Ravi S. Sundaram, Marko Burghard, and Klaus Kern, *"Electrical conduction mechanism in chemically-derived graphene monolayers"* Nano Lett., 2009, 9 (5), pp 1787-1792.

- Ravi Shankar Sundaram , Cristina Gómez-Navarro, Kannan Balasubramanian , Marko Burghard , Klaus Kern. *"Electrochemical Modification of Graphene"* Advanced Materials 20, 3050 (2008).

* Equal first authorship.

Curriculum vitae

Name	Ravi Shankar Sundaram
Date of Birth	May 22, 1984
Nationality	Indian
June 2010-December 2010	Collaborative Research Opportunity at the IBM T J Watson Research Center Yorktown Heights, USA, Physical Sciences Department in the group of Dr. Phaedon Avouris. **Field of research:** Optoelectronics on graphene devices
2007-2011	Masters Thesis followed by Doctoral research at the Max Planck Institute for Solid State Research, Nanoscale Science Department in the group of Prof. Klaus Kern. **Field of research**: Electrical properties of chemically derived graphene.
November 2006- August 2007	Master studies in Materials Science and Engineering at the Ecole Polytechnique Federale de Lausanne (EPFL), Switzerland along with a Research Assistanceship at the Laboratory micro-nanosystems, Micro-nano technology department in the group of Prof. Juergen Brugger **Field of research**: Ink-Jetting of nanostructures

April 2005- June2005	Undergraduate Research Intern at the Institute for Nanotechnology, Forschungzentrum Karlsruhe, Germany in the group of Prof. Horst Hahn. **Field of research:** Sensor microarrays based on SnO2 nanoparticles
2002-2006	Undergraduate Studies in Metallurgical and Materials Engineering at the Indian Institute of Technology, Kharagpur, India along with a Research Assistanceship followed by Bachelors thesis research at the Dept. Metallurgical and Materials Engineering, in the group of Prof. Indranil Manna. **Field of research:** Ceramic nanocomposites for Solid Oxide Fuel Cells
1989-2001	Primary and Secondary education in India.

Acknowledgments

It is a pleasure to thank the many people who made this thesis possible.

Working in the group Prof. Klaus Kern has been one of the most challenging and knowledge building experiences in my career so far. I thank him for providing that impetus to succeed while enjoying my work. In addition I would particularly like to acknowledge the encouragement and freedom he gave for self motivated ideas. Through various stints as an undergraduate and as intern different research groups around the world, I have developed a liking towards collaborative research and I cannot thank Prof. Kern enough enabling this even during my PhD work.

I came to the Max Planck Institute as a masters thesis student. Although I had some research experience before, I was completely new to the field of carbon nanoelectronics and there aren't enough words to be said for the kind and selfless help of Dr. Marko Burghard, Dr. Cristina Gómez Navarro and Dr. Kannan Balasubramanian. Even though this work is not included in this particular thesis, the knowledge gained during this time built the foundation for the marathon PhD work that followed.

I would also like to deeply acknowledge all the guidance and advice offered by my supervisor Dr. Marko Burghard. I especially profited from all our scientific discussions through which he has instilled in me the art of meticulous self review and correction which is critical for all scientific output. I would especially like to thank him for persisting with his advise of focussing my research which was crucial for my successful collaborative work at IBM Research Center, New York. I also would like to thank him for his dedicated help in fine tuning this thesis manuscript.

Dr.Cristina Gómez Navarro was the mentor I needed to kick start my career as a researcher. Working closely with her has taught me the proper experimental methodology and analysis which I shall use for the rest of my

career as a scientist. Moreover she also has been a good friend and continues to support me both professionally and personally even after she moved to the University of Madrid. I will always be indebted to her for what she has taught me.

I found a friend, philosopher and guide in Dr. Kannan Balasubramanian. My times with him have always been filled with excitement and joy. The joy that he derives from his work has insipired me through out my time here. I am grateful to him for seamlessly accommodating me within his group when I needed to use some of the setups. This acknowledgement would be incomplete without mentioning the fun during lunch and of course TKIFs!

I am also indebted to Dr. Mathias Steiner, Dr. Marcus Freitag, Dr. Hsin-Ying Chiu and Dr. Phaedon Avouris of the IBM T.J Watson Research Center in in New York where it was an honor to spend the last half a year of my thesis work. I thank you very much for being such wonderful hosts and teaching me so much and reinforcing my love for collaborative research.
I think everyone would agree that a doctoral work is similar to a soap opera with its joyful and stressful sequences. I have been lucky to find the greatest set of friends who supported me through the tough times and shared my joy during better times. I would like to specially thank Vivek Pachauri and Tanya Kurkina for all the time we have spent together traveling, working or even simply drinking coffee! I would also thank my dear officemate and good friend Dr. Liza Herrera-Diez for being a delightful neighbour for all these years and listening to my endless loop of Pink Floyd music. Our discussions both scientific and otherwise have been extremely enjoyable. I would be remiss not to mention my friend Dr. Eduardo Lee who, with his Brazilian nature has shown me the best of times over the years both at work and away from it.

My colleagues of the molecular electronics and nanoscale diagnostics subgroup: Thomas Dufaux, Adarsh Sagar, Eva Peters, Uli Stuetzel, Nassim Rafiefard, Alexis Vlandas and all the past and present members of the group have been really helpful and friendly. I extend my sincerest expressions of gratitude to them and best wishes towards their respective theses.

I would like to thank the cleanroom group, Ulrike Waizmann, Thomas Reindl and Achim Güth and to the friendly staff of the Technology Group, Benjamin Stuhlhofer, Marion Hagel, Birgit Lemke and Stephan Schmid for their efficient and kind help at all times during my PhD work. My sincerest gratitude goes out to all the members of the Kern group. I have learnt and

profited from each of you in one way or the other.

I would also like to give a special thanks to Sabine Birtel and Frau King for making the incredibly complex administrative responsibilities so simple for me.

I would like to also thank my closest friends from IIT Kharagpur. Even though we have been spread all across the globe after graduation, I am extremely happy that we still are as close as ever and your support has always helped me. I have to thank my friend Aarathi Selvan for those wonderful sessions talking about philosophy, books and pretty much everything under the sun. I have learnt a great deal from you and many thanks to you!

An endeavour such as a Doctoral study involves sacrifices not only from the student but also his close family. I will never be able to repay the efforts put by my dear parents to prepare me for this study. I learnt the most important quality a scientist must have, patience, from them. I dedicate this thesis work to them. Lastly and importantly I thank my fiancee Swati Mishra, for the unconditional love and support during the tough last year of my PhD work.

Ravi Shankar Sundaram
Stuttgart
June 1, 2011